CO oxidation on metal supported ultrathin oxide films

vorgelegt von

Diplom-Chemieingenieurin

Yulia Martynova

aus Krasnokamensk

Von der Fakultät II - Mathematik und Naturwissenschaften

der Technischen Universität Berlin

zur Erlangung des akademischen Grades

Doktor der Naturwissenschaften

Dr. rer. nat.

genehmigte Dissertation

Promotionsausschuss:

Vorsitzender: Prof. Dr. rer. nat. Michael Gradzielski

Gutachter: Prof. Dr. rer. nat. Hans-Joachim Freund

Gutachter: Prof. Dr. rer. nat. Reinhard Schomäcker

Tag der wissenschaftlichen Aussprache: 30. Mai 2013

Berlin 2013

D 83

Acknowledgements

Abstract

Thin oxide films supported on metal substrates were studied in low temperature CO oxidation at near-atmospheric pressures. A representative selection of ultrathin films includes ruthenium oxide films grown on Ru(0001) and Pt(111) and manganese and zinc oxide films prepared on Pt(111). The performed experimental research has established relationships between the films structure and their reactivity under technologically relevant conditions (a particular dependence in each case). Based on our own findings, a unifying concept defining catalytic behavior of thin oxide films as catalytic materials was proposed. The results suggest to use oxygen binding energy on the film surface as a good descriptor for the reactivity. Weakly bound oxygen species can be formed on the oxide film surface at the high chemical potential of oxygen and serve as active species, which then replenished from the gas phase. Long-range film ordering and film/substrate nature influence the reactivity to the extent they provide weakly bound oxygen.

The fundamental study comprises surface science approach for the films preparation/characterization and conventional reactivity measurements. The films were grown either by deposition of a foreign transition metal oxide on a supporting metal single crystal or by oxidation of the substrate material under well-controlled conditions in ultrahigh vacuum. The film structure and composition were verified by low energy electron diffraction and Auger electron spectroscopy respectively. The film coverage as well as different oxygen states were distinguished by temperature programmed desorption. The catalytic performance of the films (and supports) was quantified via gas chromatography.

This systematic research reduces the lack of interpretation and comparison of the thin oxide films reactivity. The novelty of the present work relies on the idea that it lifts up thin film catalysis on the systematic level. The findings of this thesis can aid in rational design of oxidation catalysts.

Zusammenfassung

Ultradünne Oxidfilme auf Metallsubstraten wurden in der CO-Oxidation bei niedrigen Temperaturen und quasi-atmosphärischen Drücken untersucht. Eine repräsentative Auswahl ultradünner Filme enthält die Rutheniumoxidfilme gewachsen auf Ru(0001) und Pt(111) und Mangan- und Zinkoxidfilme aufbereitet auf Pt(111). Die durchgeführte experimentelle Forschung hat die Struktur-Reaktivitätsbeziehungen der Filme unter technologisch relevanten Bedienungen eingerichtet (individuell in jedem Fall). Ausgehend von unseren Ergebnissen wurde ein vereinheitlichtes Konzept vorgeschlagen, das die katalytischen Eigenschaften von dünnen Oxidfilmen beschreibt. Die Ergebnisse legen nahe, dass die Bindungsenergie von Sauerstoff auf der Filmoberfläche als Maß für die Reaktivität verwendet werden kann. Schwach gebundene Sauerstoffspezies können auf der Oxidfilmoberfläche unter dem hohen chemischen Sauerstoffpotenzial gebildet werden und als aktive Spezies dienen, die dann aus der Gasphase ersetzt werden. Die Fernordnung der Filme und die Art der Filme/Substrate beeinflussen die Reaktivität in dem Maß, in dem sie schwach gebundenen Sauerstoff bieten.

Die Grundlagenforschung verbindet so genannte 'surface science approach' zu Filmpräparation und Charakterisierung mit herkömmlichen kinetischen Messungen. Die Filme wurden entweder durch der Ablagerung der fremden Übergangsmetalloxide auf dem Einzelkristall des stützendes Metals oder durch Oxidation des Substratmaterials unter den gut kontrollierten Bedienungen im Ultrahoch-Vakuum hergestellt. Die Filmstruktur und Zusammensetzung wurden anhand der 'low energy electron diffraction' (LEED) und der Augerelektronenspektroskopie (AES) überprüft. Die Filmbedeckung sowie die verschiedenen Sauerstoffzustände wurden mittels temperatur-programmierter Desorption (TPD) unterschieden. Das katalytische Verhalten der Filme (auch der Substrate) wurde mithilfe Gaschromatographie quantifiziert.

Diese systematische Untersuchung vermindert die Lücken der Interpretation und des Vergleiches der Reaktivitäten dünner Oxidfilme. Die Neuigkeit dieser Arbeit vertraut auf die Idee, dass sie die Dünnfilme-Katalyse auf das systematische Niveau hebt. Die Ergebnisse dieser Arbeit können den rationalen Entwurf von Oxidationskatalysatoren fördern.

Contents

Chapter 1

Introduction

Production of valuable chemicals always stays an important area of mankind interests: industry producing materials cares about economic prosperity, while scientists look for elegant fundamental solutions and analytical methods. To govern a chemical reaction, i.e. to get a desired product with reasonable time and financial expenses and suppress byproducts formation or to decompose harmful substance, *catalysts* are used. This wide class of materials makes possible *catalysis*, a phenomenon of chemical reactions acceleration. Among a broad range of catalytic reactions a special place belongs to those which occur on the interface between different phases, i.e. heterogeneously. Commonly *heterogeneous catalysis* refers to gaseous components interaction on the solid surface. This is determined by advantageous properties of solid catalysts, since they satisfy to such critical requirements as high *activity* and *selectivity*, prolonged *lifetime* and easy *regeneration* [1].

Essential part of conventional catalysts often represents metals dispersed over oxide support. Fundamental studies needed for precise investigation of the reaction mechanism (a sequence of elementary steps) demand well-controlled conditions for catalysts preparation and powerful analytical tools for their characterization. Such a combination is fulfilled in *ultrahigh vacuum (UHV)*, when catalysts are least affected by foreign molecules, and electron based surface sensitive techniques can be applied [2]. Under UHV conditions model (two-dimensional, 2D-) catalysts are simplified to *single crystalline surfaces* with an ordered structure and well-known composition. The epoch of intensive studying of surface reactions of small molecules, e.g. *CO oxidation* (well-known probe reaction) [3], was facilitated by advances in *vacuum technique* and yielded in a special interdisciplinary area of human knowledge known as *surface science* [4].

A model reaction of CO oxidation was chosen as a 'working horse' of surface science to study catalytic properties of metal and oxide surfaces on fundamental level and avoid a wide range of intermediate reaction products. Such an approach minimizes the overall complexity of experiments and calculations both. This leads to better understanding of elementary steps of the reaction and is usually called as 'model studies in heterogeneous

catalysis'. On metals the reaction proceeds through the Langmuir-Hinshelwood mechanism when both reactants are adsorbed on the catalyst surface [5]. On oxygen-covered metallic surfaces and oxides the Eley-Rideal mechanism could be in operation: only one of the reactants (O) is chemisorbed, while the other species (CO) reacts by direct collision from the gas phase [6].

However, studies of oxide single crystals often suffer from *charging* problems due to their insulating properties. To overcome this drawback single crystalline *thin oxide films*, epitaxially grown on metal single crystals, were introduced into the practice of model heterogeneous catalysis and serve as supports for deposited metal nanoparticles [7]. But, this decrease in material dimensions and reactant pressures caused specific problems called *material* and *pressure gaps* respectively: particular material properties and catalytic behavior depend on catalyst size and pressure scale and cannot be directly extrapolated [8]. Under the term 'pressure gap' it is commonly understood that the structure of the active phase of a catalyst on atomic scale under industrial reaction conditions can be completely different from that in UHV due to several orders of magnitude ($\geq$ 12) pressure drop of the reactants [9]. To bridge the pressure gap between the fundamental surface science studies and large-scale chemical processes it was suggested to combine preparation of single crystalline surfaces and their analysis in UHV with high-pressure reactivity measurements - up to 1 bar (see [10] and references therein]).The material gap implies that the number of active sites in industrial catalysts is higher (2-4 orders of magnitude) than in planar (2D) single crystalline model catalysts, and their quality (coordination, defects, phases) can differ substantially [8].

Recent studies have shown that *ultrathin oxide films on metals* can demonstrate interesting catalytic properties on their own right [11-13]. Particularly, in the earlier works of our group well-ordered *monolayer FeO* films on Pt(111) were demonstrated to catalyze the CO oxidation reaction much more active than either bare Pt(111) substrate or nm-thick Fe_3O_4 films at low temperatures and near-atmospheric pressures [14]. Such enhanced reactivity was attributed to the charge transfer between metal and oxide which leads to oxygen activation on the surface and consequent oxide lattice reorganization. O-terminated O-Fe-O *trilayer* structure forming under reaction conditions was proven to direct CO oxidation through the Mars-van Krevelen like mechanism: weakly bound top layer oxygen

species are attacked by gas phase CO resulting in CO_2 production and are later replenished from the gas phase O_2 (rate limiting step) [15-17]. For the structural explanation see Fig.1.1a.
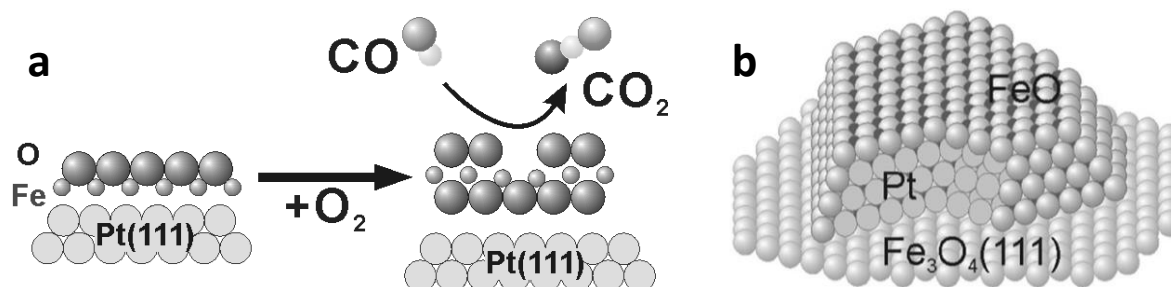
Figure 1.1 Ultrathin FeO film grown on Pt(111): a - Lattice transformation of FeO film to FeO_2 structure which supplies weakly bound oxygen for the reaction [11], b - supported Pt nanoparticles are encapsulated by a FeO layer upon annealing [15].

Therefore the film thickness may affect the reaction, particularly when charge transfer is the rate limiting step. If the film thickness does matter, then this allows one to tune the reactivity and selectivity of such an "inverted" catalyst, where an oxide phase is supported by a metal, in contrast to a traditional oxide-supported metal catalyst. In fact, such ideas have already been put forward, most notably by Vol'kenstein [18] and Schwab [19] (see also a critical review by Slinkin et al. [20]), who developed the so-called "electron theory of catalysis" based, in essence, on the concept of Schottky barriers. However, in that time the preparation and atomic scale characterization of thin oxide films was not feasible. In terms of this theory one can explain low reactivity of thick Fe_3O_4 films: the oxide film should be very thin to allow the charge transfer, since thin films possess lattice flexibility which may significantly contribute to stabilization of charged adsorbates (polaronic distortion). This property is not present in a thicker film, which behaves like the bulk counterpart. However, high reactivity of Pt nanoparticles deposited on top of thick Fe_3O_4 films was rationalized as strong metal support interaction (SMSI effect): upon annealing Pt surface gets covered with a FeO monolayer as shown on Fig.1.1b [21, 22]. Minimization of surface energy is considered as one of the main driving forces for encapsulation.

It is getting obvious, that this experience with accumulated knowledge is already a solid foundation in the field of supported oxide film catalysis. At the moment, this fast developing experimental trend (and theoretical as well) suffers from the lack of descriptive functions and 'methodological algorithms' which are needed to compare/predict the

reactivity of a new kind of model catalysts. Therefore, it is necessary to give a straightforward clue and build up an appropriate concept to be able correctly to interpret the catalytic activity of thin oxide films.

Being inspired with the enhanced reactivity of ultrathin oxide films, mentioned above, in the present work I have studied the catalytic performance of ruthenium oxide films grown on ruthenium and platinum and zinc and manganese oxide films grown on platinum. The aim of this thesis was to establish a direct relationship between the films structure and their reactivity in CO oxidation with a particular focus on thickness influence.

For this I have prepared a series of thin oxide films of each type under well-controlled conditions. The films were characterized (order, composition, coverage/thickness) under UHV conditions and tested in low temperature CO oxidation at elevated pressures. The work is organized as follows. At first, the whole experimental setup and utilized methods are overviewed (Chapter 2): low energy electron diffraction (LEED), Auger electron spectroscopy (AES), temperature programmed desorption (TPD) and gas chromatography (GC). Such a combined approach of traditional surface science tools (LEED, AES and TPD) and widely used analytical technique of GC let us to perform accurate film fabrication, their precise characterization and the reactivity measurements on the high level. Major experimental results (LEED patterns, AES and TPD spectra, the reaction kinetics) for each kind of films are presented: for $RuO_x/Ru(0001)$ and $RuO_x/Pt(111)$ in Chapter 3, for $ZnO/Pt(111)$ in Chapter 4 and for $MnO_x/Pt(111)$ in Chapter 5. Since the films nature is rather different, a literature overview for each film type is given in the beginning of a corresponding chapter prior to experimental results. In Chapter 6 I compare the catalytic performance of all films and finally summarize overall findings to conclude about the reactivity of ultrathin films in general and give an outlook in this respect.

Chapter 2

Background and Methods

2.1 Apparatus

A prior requirement for working with the well-defined surfaces is to maintain them in clean state within analysis time limits. Therefore to minimize the influence of undesirable adsorbate species (contamination, reconstruction) the samples should be kept under ultrahigh vacuum (UHV) conditions with pressures lower than 10^{-9} mbar. Another major reason concerns a prerequisite for surface science instrumentation. The use of characterization tools needs a UHV regime as well to avoid electron scattering by residual gas and to extend the lifetime of an electron source. Therefore a proper vacuum technique is a necessary precondition to prepare and study model catalysts.

The experiments were carried out in a stainless steel UHV chamber, as shown in Fig.2.1, with the base pressure 1×10^{-10} mbar. The vacuum of several ranges is maintained by four pumping stages which comprise an *Edwards* rotary pump ($\sim 10^{-2}$ mbar), a *Pfeiffer* turbomolecular pump (10^{-8} mbar) and a *Varian* Ti sublimation pump with a *Varian* ion pump (10^{-10} mbar). The chamber is heated up to 145$^{\mathrm{o}}$C ('baked') for at least 12 hours to remove water vapor as a major contaminant and thus to reach the UHV level. The pressure in the chamber is monitored by two gauges: in the range $10^{-6} \div 10^{-10}$ mbar by a *Varian* nude Bayard-Alpert type ionization gauge, in the range $10^{-5} \div 10^{-4}$ mbar by a *Varian* cold cathode ionization gauge. Gas line system allows supplying six different gases of high purity for backfilling, high pressure or desorption experiments and is pumped out by an *Edwards* rotary pump ($\sim 10^{-2}$ mbar) as well.

The rotatable x-y-z manipulator with an option of liquid nitrogen cooling is employed to place the sample attached to the sample holder in front of various analytical tools. The metal substrate used in this work is a double-side polished single crystal (99.99%, *MaTeck*, ~10 mm in diameter, 1.5 mm in thickness) of either Pt(111) or Ru(0001). As shown in Fig. 2.2 the sample was mounted to two parallel Ta (1mm) sticks by a pair of Ta wires (0.25-0.4 mm),

which were used for resistive heating and also for cooling by filling a manipulator rod with liquid nitrogen. The temperature was measured by type K thermocouples (chromel-alumel) spot-welded to the edge of the crystal, and controlled by a PID feedback system (*Schlichting Phys. Instrum.*). The temperature could be varied between ca. 85 K and 1300 K.
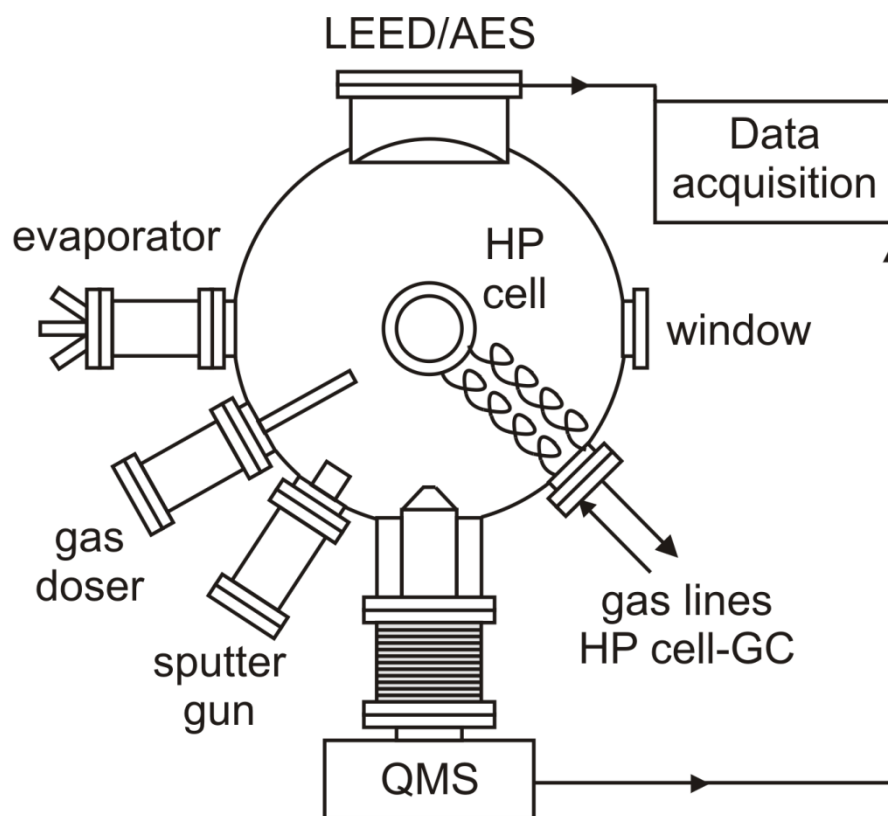
Figure 2.1 Horizontal cross-sectional view of the UHV chamber

For the thin films deposition by the physical vapor deposition (PVD) method the UHV chamber was equipped with electron beam assisted metal evaporator (*Focus EFM3T*) and a homebuilt effusion cell containing high purity deposition materials (*Goodfellow*). Clean metallic surfaces were prepared by Ar^+ ion bombardment with an *Omicron* sputter gun.

Low energy electron diffraction (LEED) optics coupled with an Auger electron spectrometer (AES) from *Omicron* was used to control the surface quality of prepared samples. A *Hidden* quadrupole mass spectrometer (QMS) was utilized for Residual Gas Analysis and Temperature Programmed Desorption (TPD) studies. For TPD studies the sample was exposed to gases through a directional gas doser. The pressure in that line was controlled by a MKS Baratron® gauge (*MKS Instruments*) and maintained by a *Pfeiffer*

turbomolecular pump. The LEED patterns were recorded with a *Canon* EOS 400D camera. The AES and TPD data collected by the corresponding software were evaluated using Origin program (*OriginLab*).
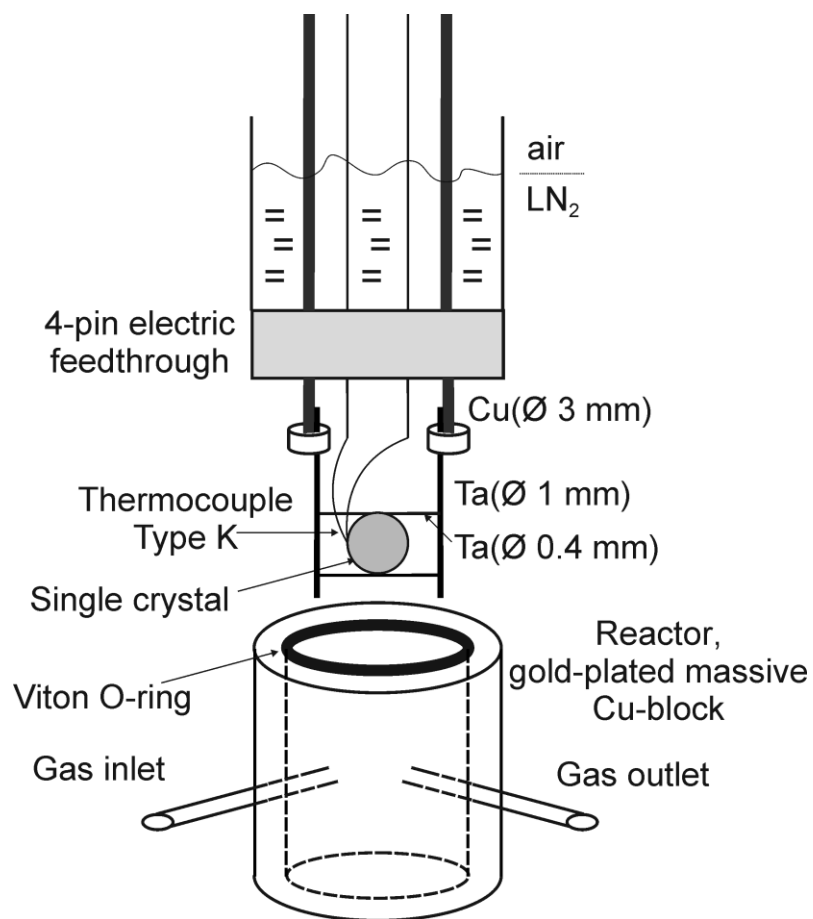
Figure 2.2 Sample holder and high-pressure cell sketch

The reactivity studies and treatments at elevated pressures were conducted in an especially designed "high-pressure" cell (HP cell, ~30 ml, Au-plated Cu massive block), built in inside the UHV chamber (see Fig. 2.2). An *Agilent Technologies* gas chromatograph (GC) connected by gas lines to the HP cell allows monitoring gas composition and the reaction kinetics. The manipulator rod inside the chamber ends with a KF-type flange with a 4-pins electrical feedthrough holding Cu and thermocouple wires.

To carry out the CO oxidation reaction, the following procedures were used. The well-characterized sample was moved vertically down to the high-pressure cell, which was then sealed from the UHV chamber by using a *Viton* O-ring placed on top of the reactor

matching the flange at the end of the manipulator. The reactor was then filled with reactants (CO (99.997%) and O_2 (99.9996%), *Linde*) up to the desired pressure in mbar range and balanced by He (99.9999%, *Linde*) up to 1 bar. Gas admission was controlled by two MKS Baratron® gauge (*MKS Instruments*). Meanwhile the main chamber remained in the pressure of ~10^{-8} mbar range. CO was additionally cleaned using a cold trap kept at 200 K. Reactants were circulated for 20 min at room temperature to equilibrate gas concentrations and to steady the gas flow using a membrane pump. The sample was then heated up to the reaction temperature with a constant heating rate. Sampled gas mixture probes were divided in GC using an HP-PLOT Q column in isothermal mode at 35 ºC and analyzed by a thermal conductivity detector (TCD) (see Fig. 2.3).

After the reaction, the spent catalyst was cooled down to room temperature within 2-3 min, and the reactor was pumped out down to ~10^{-5} mbar before exposing to UHV. Then the manipulator was retracted, and the post-reaction structural characterization of model catalysts was performed.
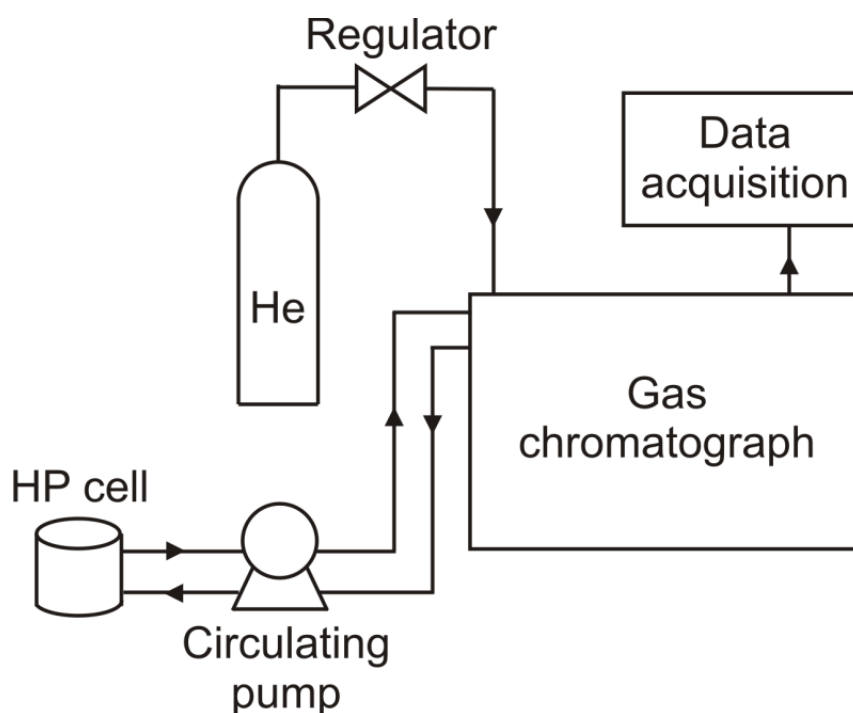
Figure 2.3 Gas chromatograph setup

2.2 Analytical methods

2.2.1 Low energy electron diffraction (LEED)

LEED stays the most frequently used experimental technique for structural characterization in surface science. Upon bombardment of crystalline solids by accumulated beam of electrons with a primary energy below 300 eV and observation of diffracted electrons as spots on a fluorescent screen the method can provide the information about long-range ordering and symmetry [23]. Due to different interatomic and interplanar distances in crystalline materials, the electron diffraction patterns are characteristic for a specific crystallographic structure and can be used to distinguish the structures.
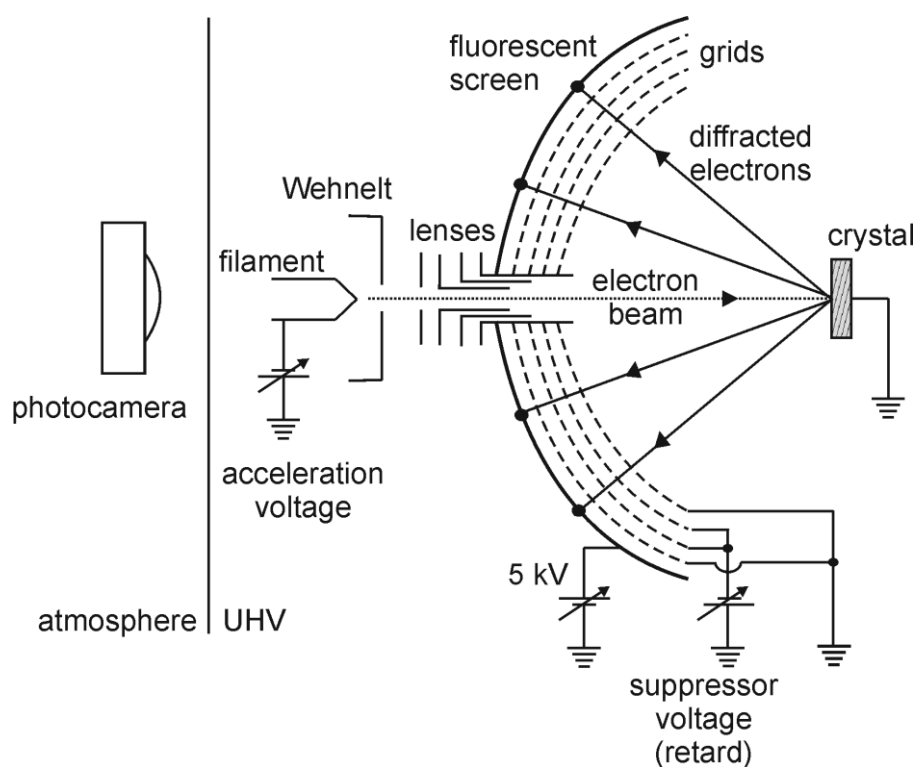
Figure 2.4 Diagram of a standard 4-grid LEED optics apparatus

A typical experimental set up is illustrated schematically in Fig. 2.4. The standard LEED apparatus comprises a hemispherical fluorescent screen and an electron gun aligned along the central axis of the screen. Accelerated electrons are emitted from the electron gun filament with low work functions (LaB_6, W or Ir), which then follow paths along the central axis with the aid of Wehnelt cap and electrostatic lenses, and finally hit the sample at ground potential in order to prevent charging. The backscattered electrons are then accelerated

towards the screen biased to 3-6 kV. The grid nearest the sample is grounded to allow the linear beam trajectories. The next two grids (called retard, suppressor or gate) are at a potential of several volts below the incident electron beam and provide accurate energy selection, therefore the inelastically scattered electrons which have lost more than a few volts cannot reach the screen – they are screened out. To make the retarding field homogeneous and mechanically stable these grids often go in pair. The fourth grid is again grounded to prevent the influence from the screen potential on the energy-selection grids. The elastically backscattered from crystal atoms electrons give a diffraction pattern [24].

In 1921 L. de Broglie predicted that every moving particle has a wave-like nature. This means that the particles, e.g. the electrons, undergo the effects associated with waves, such as diffraction or interference. In 1927 C. Davisson and L. H. Germer experimentally observed the angular distribution (a diffraction pattern) of electrons elastically scattered from Ni sample when applying a monochromatic beam of low energy electrons onto the crystal surface and explained their data in terms of diffraction of the electrons from crystallites [24].

The theoretical explanation for the formation of diffraction patterns from crystal structures is as follows: coming from de Broglie's equation for the electron's wavelength, the wavelength's dependence on the electron's kinetic energy (determined by the electron beam energy) can be derived:

$$\lambda = \frac{h}{p} = \frac{h}{m\vartheta} = \frac{h}{\sqrt{2mE_k}} = \frac{h}{\sqrt{2meV}} \ or \ \lambda = \left(\frac{150.4}{E_k}\right)^{1/2} \qquad (2.1)$$

where λ is the wavelength in m, $h=6.626\times10^{-34}$ Js is the Planck's constant, p is the electron's momentum, E_k is the electron's kinetic energy, $m=9.11\times10^{-31}$ kg is the electron mass, $e=1.6022\times10^{-19}$ C is the electron charge and V is the beam energy.

Electron scattering provides information about the surface (is surface sensitive) if the electrons are granted the correctly chosen energy. The inelastic mean free path (IMFP) of electrons in a solid depends on the energy of the electrons in a manner that does not depend too strongly on the chemical identity of the solid illustrated by the universal curve (see Fig.2.5) [25]. A beam of low energy electrons (V = 30-200 eV) results in a small wavelength λ of 1-2 Å which is of a size of interatomic distances in a crystal lattice (< 3 Å).

This is short enough to probe only first 3-4 atomic layers: electrons scattered from deeper gap virtually play no role in the detected signal.
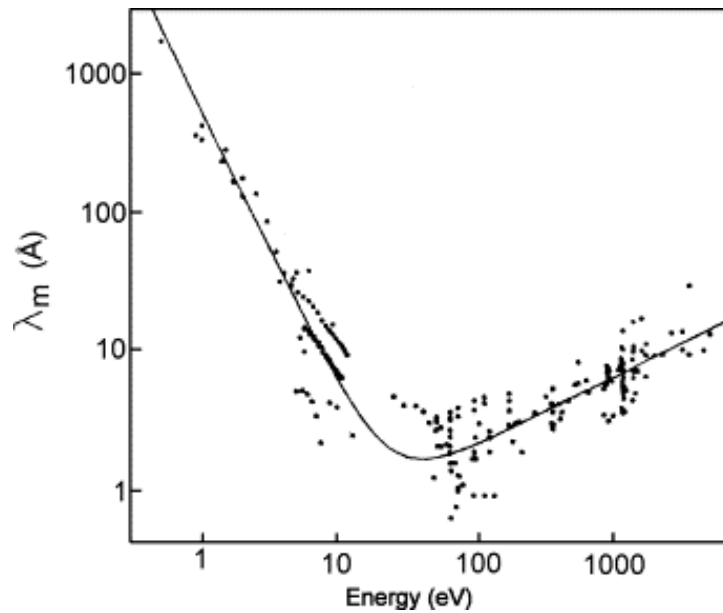
Figure 2.5 Universal curve of electron mean free path in solid matter [25]

Diffraction spots experimentally visible on a display system certify that the elastically scattered electrons undergo a constructive interference following the Bragg's law (for X-rays originally) if the path difference between the electrons coming from different atoms is equal to the multiplicity of the wavelength [24]:

$$2dsin\theta = n\lambda \tag{2.2}$$

where d is the interplanar distance in the crystal lattice, θ is the angle between the beam and the sample plane, n is an integer and λ is the wavelength. The process of electron scattering at the crystal surface is schematically shown in Fig. 2.6. The electron beam used at above 50 eV has typically a beam diameter of around 1 mm. The instruments transfer width (which is essentially the coherence length of the electrons) is of approximately 5-10 nm in modern instruments. Naturally only structures which extent over at least (100 x 100) Å can produce Bragg reflexes. Structure domains with a smaller diameter than the coherence width will not constructively add to the diffraction pattern but add diffuse background intensity. The observed diffraction pattern is therefore an ensemble average of structural domains (larger than the incident beam coherence width) within the electron beam.
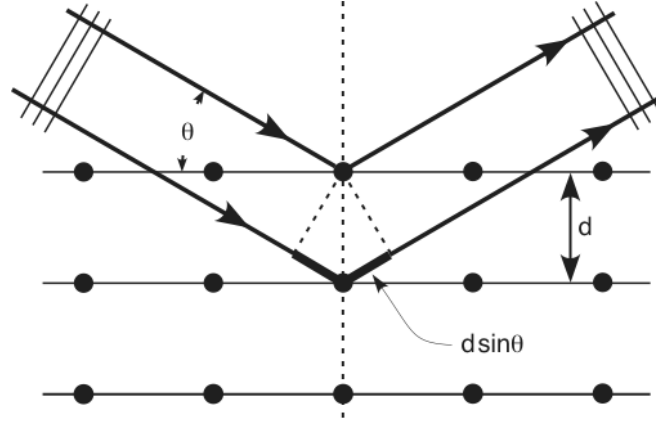
Figure 2.6 Diffraction process

LEED gives the information about the 2D-structure of the sample surface. A diffraction pattern is a geometrical visualization of a real crystal lattice in reciprocal space – the concept well-known for bulk X-ray diffraction. In 2D space, the lattice vectors are spanned by two base vectors $\vec{a}_1$ and $\vec{a}_2$, the reciprocal lattice follows from the definition of the reciprocal lattice vectors $\vec{a}_1^*$ and $\vec{a}_2^*$:

$$\vec{a}_1^* = 2\pi \frac{\vec{a}_2 \times \vec{n}}{\vec{a}_1(\vec{a}_2 \times \vec{n})}, \qquad \vec{a}_2^* = 2\pi \frac{\vec{a}_1 \times \vec{n}}{\vec{a}_2(\vec{a}_1 \times \vec{n})} \qquad (2.3)$$

$\vec{n}$ is the vector normal to the surface. This also means:

$$\vec{a}_i \cdot \vec{a}_j^* = 2\pi \delta_{ij} \qquad (2.4)$$

$$|\vec{a}_1^*| = \frac{2\pi}{|\vec{a}_1| \sin \alpha}, \qquad |\vec{a}_2^*| = \frac{2\pi}{|\vec{a}_2| \sin \alpha} \qquad (2.5)$$

where $\vec{a}_i$ are the base vectors of the real lattice (i=1,2); $\vec{a}_j$ are the base vectors of the reciprocal lattice (j=1,2); δ_{ij} is the Kronecker delta, $\delta_{11}=\delta_{22}=1$, , $\delta_{12}=\delta_{21}=0$; α is the enclosed angle between $\vec{a}_1$ and $\vec{a}_2$. The diffraction conditions for a two dimensional lattice are given by the two dimensional Laue conditions:

$$\left(\vec{k_i} - \vec{k_j}\right)\vec{a}_1 = 2\pi h, \qquad \left(\vec{k_i} - \vec{k_j}\right)\vec{a}_2 = 2\pi k \qquad (2.6)$$

where h and k are arbitrary integers. They principally represent the conservation of energy and momentum between the incident wave vector $\vec{k_i}$ and the emerging wave vector $\vec{k_j}$. This condition is fulfilled whenever $\Delta\vec{k}$ equals a reciprocal lattice vector $\vec{G} = h\vec{a}_1^* + k\vec{a}_2^*$. The

12

energy conservation requires that $\left|\vec{k_\iota}\right| = \left|\vec{k_j}\right|$. These two conditions can be made visible by changing the Ewald construction known from x-ray scattering to the surface case as shown in Fig. 2.7 [26].
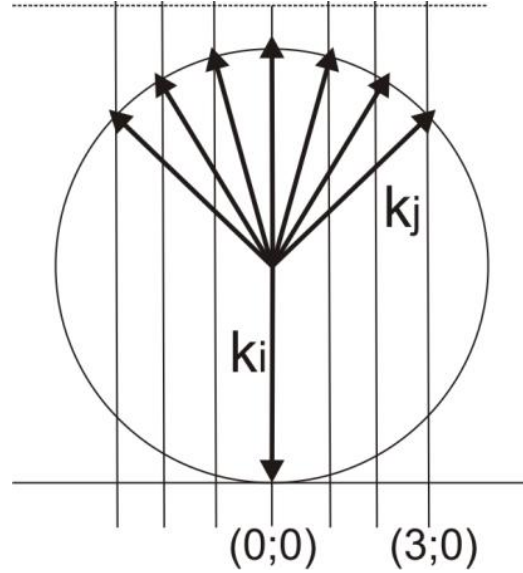
Figure 2.7 Ewald sphere synthesis for 2D case. Incident and diffraction beams are labeled

An overlayer structure with a rather large unit mesh and various domains may generate a complicated pattern. The lattice vectors of the surface including possible adsorbate overlayers are characterized as $\vec{b}_1$ and $\vec{b}_2$. A simple nomenclature of surface structures is that of Wood's. The surface structure is described by

$$N \left(\frac{b_1}{a_1} \times \frac{b_2}{a_2} \right) R\beta \qquad (2.7)$$

where N= "P" or "c" for primitive or centered cells, respectively, and β is the angle by which the surface vectors have to be rotated with respect to those of the bulk (see Fig. 2.8). The nomenclature of Wood has the advantage of simplicity. It is, however, not possible to describe all surface structures because the rotation angle might not be the same for both vectors.

Wood notation   Matrix notation
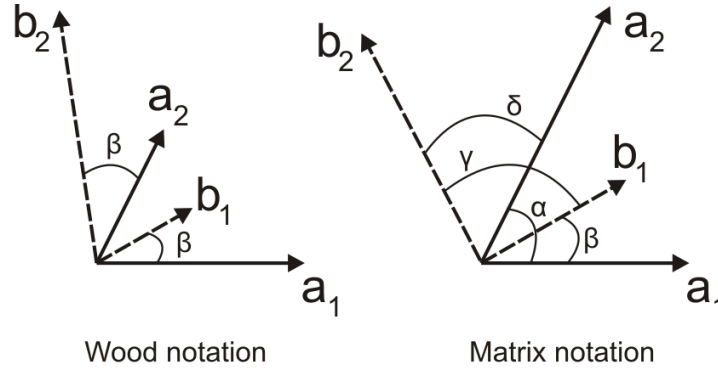
Figure 2.8 Terminology for surface lattices. a_1 and a_2 correspond to the substrate unit cell vectors. b_1 and b_2 indicate the superstructure unit cell vectors. α is the enclosed angle between the substrate, γ is the enclosed angle between the superstructure unit cell vectors. The angles β and δ accounts for a rotation of the superstructure with respect to the substrate.

The matrix representation (offered by Park and Madden) of superstructures shows that as $\vec{b}_1$ and $\vec{b}_2$ can be built up by the substrate unit cell vectors:

$$\vec{b}_1 = m_{11}\vec{a_1} + m_{12}\vec{a_2}, \quad \vec{b}_2 = m_{21}\vec{a_1} + m_{22}\vec{a_2} \qquad (2.8)$$

$$M = \begin{bmatrix} m_{11} & m_{12} \\ m_{21} & m_{22} \end{bmatrix} \qquad (2.9)$$

The indices m_{ij} can be derived by trigonometric considerations:

$$M = \begin{bmatrix} \frac{|b_1|}{|a_1|}[\cos\beta - \sin\beta \cot\alpha] & \frac{|b_1|}{|a_1|}\frac{\sin\beta}{\sin\alpha} \\ \frac{|b_2|}{|a_1|}[\cos(\beta+\gamma) - \sin(\beta+\delta)\cot\alpha] & \frac{|b_2|}{|a_2|}\frac{\sin(\beta+\gamma)}{\sin\alpha} \end{bmatrix} \qquad (2.10)$$

where the meaning of the variables is illustrated in Fig. 2.8.

In addition to mathematical formalism of the method theory it is necessary to label the real structures of the crystal surfaces and superstructures resulting from coincidence with adsorbate overlayers as well as corresponding LEED patterns using fundamental crystallographic two-dimensional (2D) Bravais lattices and Miller indices for low index planes as shown on Fig.2.9.
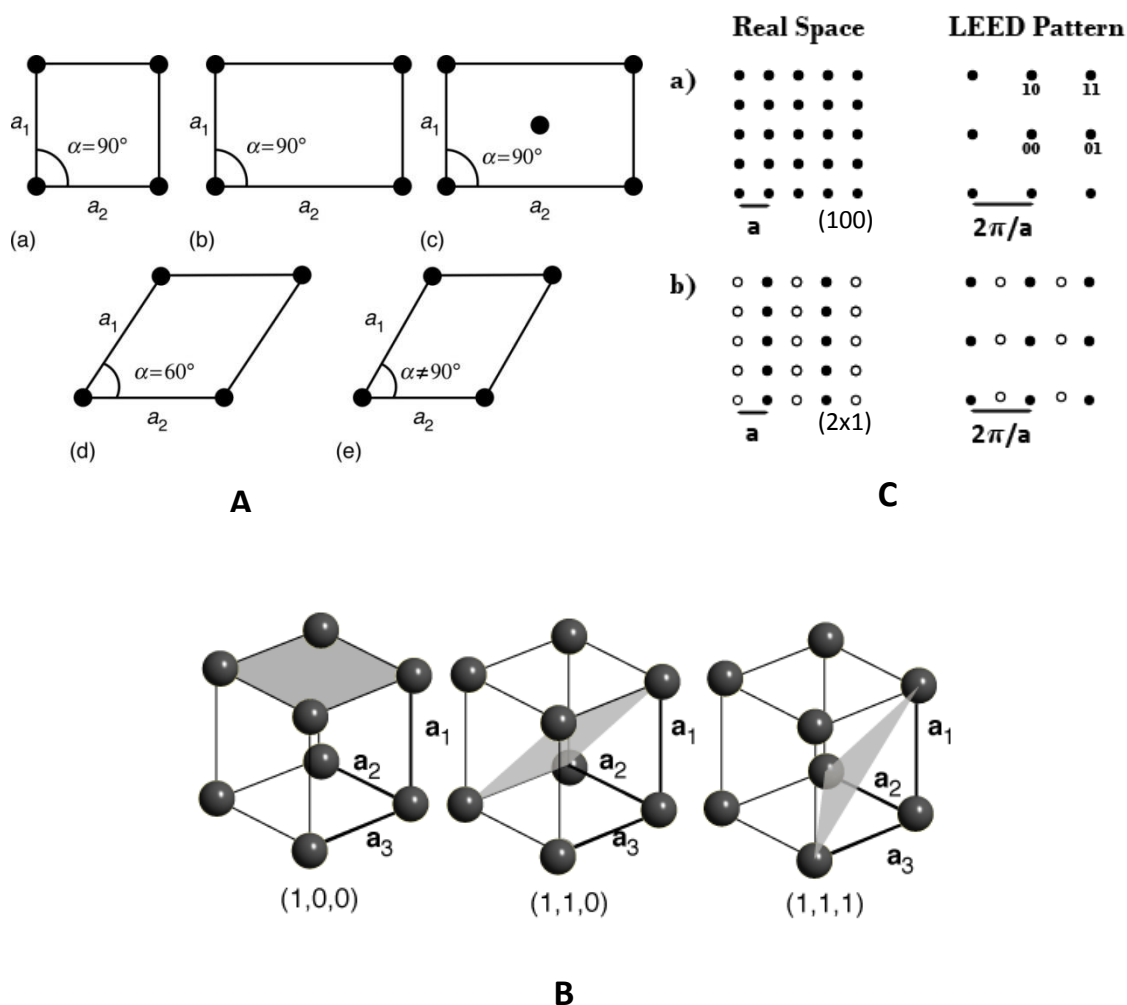
Figure 2.9 Crystallographic notation systems. A: 2D Bravais lattices: a – square, b – rectangular, c – centered rectangular (rhombic), d – hexagonal, e - oblique.). B: Miller indices. C: Real space- and reciprocal lattices (white spots are associated with the adsorbate structure.

2.2.2 Auger electron spectroscopy (AES)

AES is a widely used experimental technique utilizing the Auger effect. The technique allows determining surface chemical composition by investigating the kinetic energy of the Auger electrons emitted from the sample upon electron bombardment. One of practical advantages of the AES technique is experimental compatibility with LEED optics. The Auger effect was discovered by Lise Meitner and Pierre Auger independently in the 1920s [27]. It was first described by Meitner; however, Pierre Auger was a scientist who was mostly credited for it. They observed an internal conversion of energy from a radiationless transition.

15
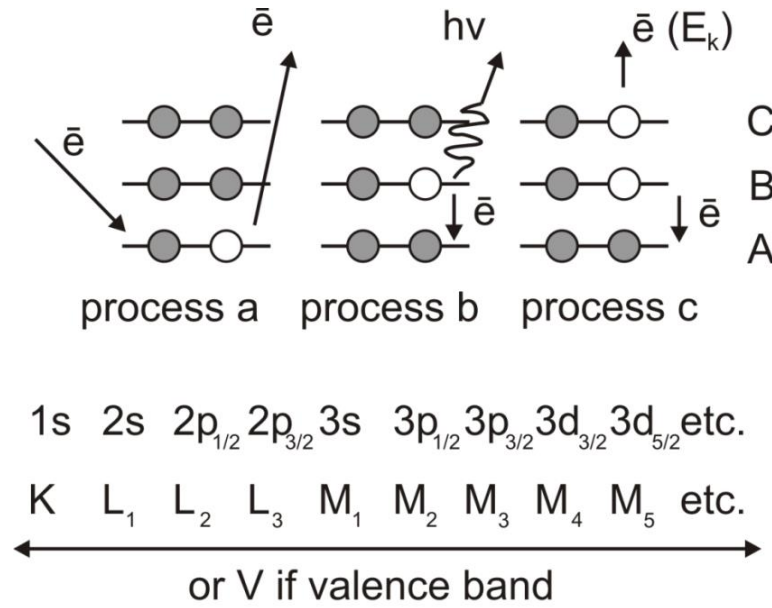
Figure 2.10 Auger electron emission mechanism and shells nomenclature

The physical mechanism of the Auger process and the shells nomenclature are given in Fig. 2.10. An electron beam of high energy typically of 2-5 KeV is used to ionize core levels of atoms, labeled as A. The ionized atom that remains after the removal of the core electron is in a highly excited state (a) and will rapidly relax back to a lower energy state by one of two routes: X-ray fluorescence (process b) and Auger emission (process c). A higher level electron fills the vacant core level. The energy liberated in this process is transferred to a second electron which is called the Auger electron. The Auger electron is then emitted with the kinetic energy:

$$E_k = E_{core} - E_{outer1} - E_{outer2} - \delta E - \phi \qquad (2.11)$$

where the δE term accounts for the relaxation effects involved in the decay process, which leads to a final state consisting of a heavily excited, doubly ionized atom; ϕ is the work function.

Therefore, the kinetic energy of the Auger electron is independent of the primary energy. An Auger transition (ABC) is therefore described by the initial hole location (A) and followed by the locations of the final two holes (B, C). The energies of the Auger electrons are in the range of 50 to 3000 eV and give a characteristic spectrum of peaks for atoms of a specific element due to unique orbital energies (besides H and He no Auger peaks because of two-

hole final state). Since AES peaks are rather low in intensity (see Fig.2.11), the spectra are typically recorded as the first derivative using lock-in techniques as shown in Fig. 2.12 [28].
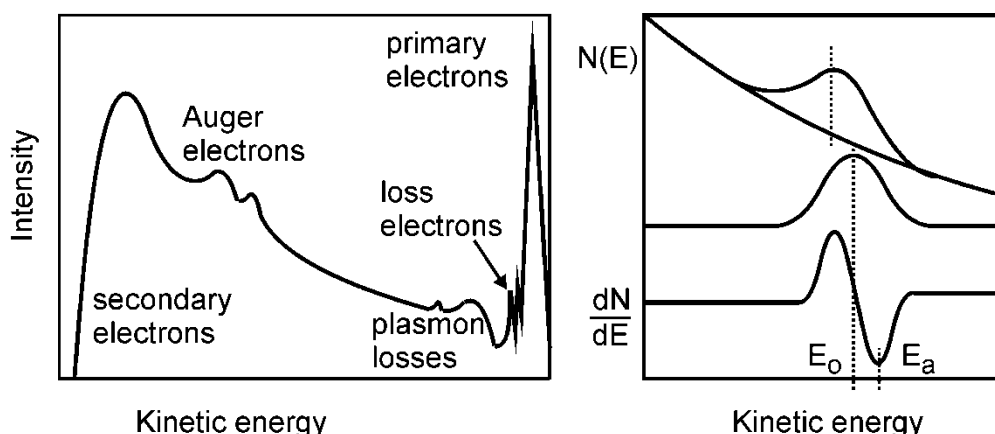
Figure 2.11 Energy spectrum of electrons coming from a surface irradiated with a beam of primary electrons. Electrons have lost energy to vibrations and electronic transitions (loss electrons), to collective excitations of the electron sea (plasmon losses), and to all kinds of inelastic processes (secondary electrons). The element-specific Auger electrons appear as small peaks on an intense background, and are better visible in a derivative spectrum.
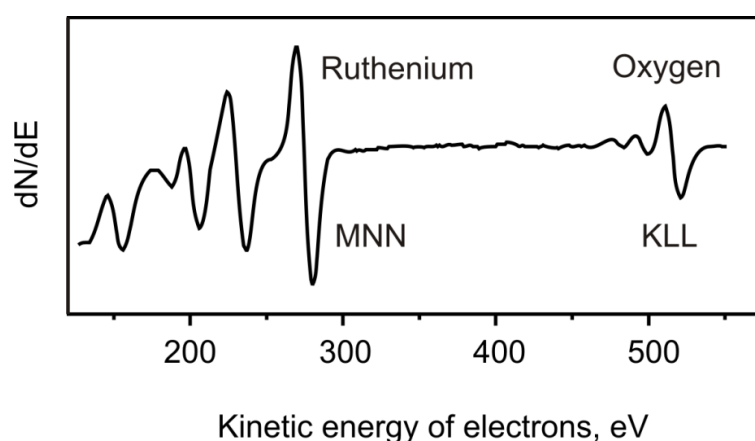
Figure 2.12 AES spectrum of ruthenium oxide as an example. Primary energy: 3 keV.

The AES often bases on the same setup as LEED utilizing a retarding field analyzer (see Fig.2.4 and Fig.2.13). Electron gun is placed in front of the sample and current is applied to the filament. Emitted and accelerated electrons hit the sample initiating the Auger process. Retarding grids allow only the Auger electrons with a given energy to pass through. The potential increases in steps, for example 1 eV/1 sec, which allows collecting all electrons with energies in a given range. The multiplier filters noise, strengthens and digitizes the signal which is then recorded by a computer in a form of the kinetic energy vs. Auger electron intensity plot. It is possible by adding a small sine (periodic oscillation) to the gate: a phase-sensitive detection yields an output signal proportional to the derivative.

17
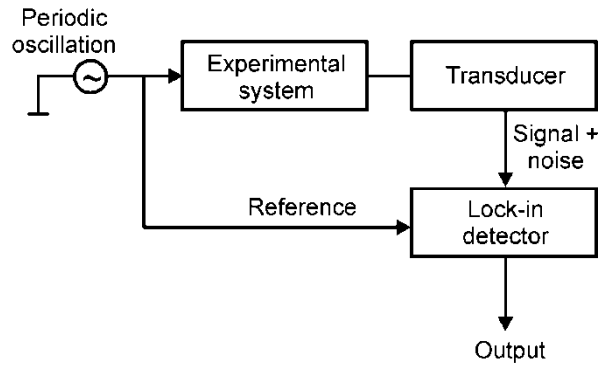
Figure 2.13 AES - electron energy analysis

Although E_k is independent of the primary beam energy (E_p), E_p is important for obtaining optimum Auger yield. The ionization probability Q_i to form a core hole in a level of energy E_i depends on the energy of the core level as $1/E_i^2$, as well as on the ratio E_p/E_i . In order to remove an electron with a binding energy E_i one needs a primary electron of higher energy. If the primary energy is too high, the electron simply goes too fast to have efficient interaction with a bound electron in a core level. As a result, it is shown theoretically by calculating cross section that a maximum cross section is obtained when E_p is three to five times of the core electron energy (see Fig.2.14) [28]. Therefore, the Auger electron of the kinetic energy ranging from 50 eV to 1000 eV need the primary energy in the range 2-5 keV. Auger transitions are more probable for lighter elements. According to the universal curve shown in Fig. 2.5, the Auger electron can escape from subsurface region of 1-2 nm in depth which corresponds to 3-5 atomic layers of the sample.
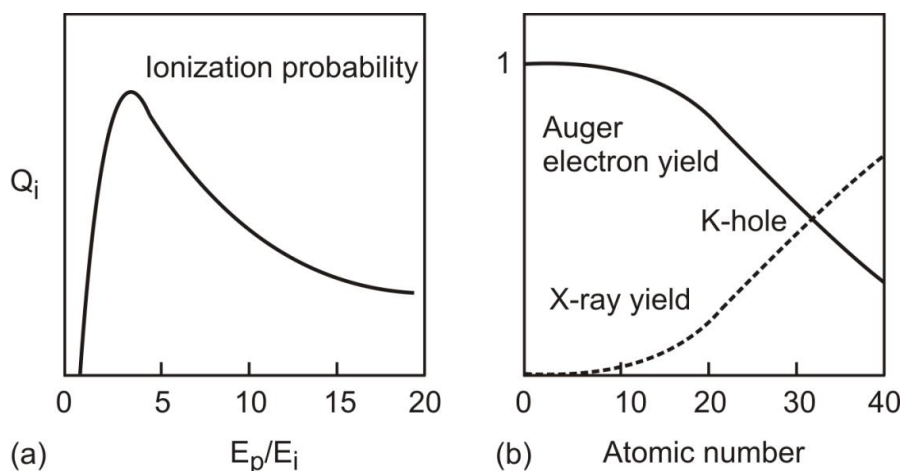
Figure 2.14 Optimal energy of a primary beam and yield of Auger electrons. a - The probability Q_i to create a core hole in a level with binding energy E_i with a primary electron of energy E_p maximizes for $E_p/E_i \approx 2$–3. b - Auger decay (solid curve) is the preferred mode of de-excitation in light elements, while X-ray fluorescence (dotted curve) becomes more important for heavier elements (shown for K shell vacancies, similar plots can be obtained for L and M shell transitions).

18

A quantitative analysis of Auger spectra is easily possible, but less straightforward than in X-ray photoemission spectroscopy (XPS) due to backscattering effects [28]. For example, the Auger yield measured from a few atomic layers thick molybdenum film on a tungsten substrate is about 20% higher than that of bulk molybdenum, because the heavier tungsten is an efficient backscatterer. This effect should be taken into account by multiplying the primary electron intensity i_p by a factor of (1+R), where R is the backscattering factor. In general, R is higher for heavier than for lighter elements, but it may also be matrix dependent. The general expression for the Auger electron current i_a becomes:

$$i_A = i_p(1 + R)QY \int_0^\infty n(z)d^{-z/\lambda cos\Theta}dz \qquad (2.12)$$

Where Y is the probability of Auger decay; n(z) is the concentration of the element at depth z; λ is the inelastic mean free path of the Auger electron; Θ is the take-off angle of the Auger electron measure from the surface normal. For a homogeneous sample with the detector perpendicular to the sample surface, Eq.2.12 reduces to

$$i_A = i_p(1 + R)QYn\lambda \qquad (2.13)$$

The mole fraction of component A in a binary mixture of A and B is given by

$$x_A = \frac{I_A/s_A}{I_A/s_A + I_B/s_B} \qquad (2.14)$$

where I_A and I_B are the intensities of the Auger peaks and s_A and s_B are the relative sensitivity factors. If there are more than two components then the denominator has to be replaced by a sum over all components. The mole fraction can be equated to the relative coverage [29].

2.2.3 Temperature-Programmed Desorption (TPD)

TPD is a surface science technique used for determination of kinetic and thermodynamic parameters of desorption processes or decomposition reactions from desorption behavior of adsorbed species. It can provide both qualitative and quantitative information. A sample exposed to a gas is heated with a temperature program (where the temperature is a linear function of the time) and the partial pressures of atoms and molecules evolving from the sample are measured, e.g. by mass spectrometry. When

experiments are performed using well-defined surfaces of single-crystalline samples in a continuously pumped UHV chamber then this experimental technique is also referred to as thermal desorption spectroscopy (TDS). TPD offers interesting opportunities to interpret desorption in terms of reaction kinetic theories, such as the transition state formalism.

The sketch of a typical experimental setup for TPD studies is presented on Fig.2.15. The sample is linearly heated with a rate $\beta=0.5-5$ Ks^{-1} resulting with the temperature ramp $T=T_0+\beta t$ with time t. The concentration of desorbing species is usually measured with a quadrupole mass spectrometer (QMS) also known as a residual gas analyzer (RGA). The pumping speed should be sufficiently high to prevent readsorption of the desorbed species back onto the surface. The mass spectrometer has a shield with a nozzle pointing towards the sample which therefore eliminates signals coming from the sample holder. The sample is positioned < 1 mm far from the nozzle. A QMS consists of three sections. In the first ionization region, gas atoms and molecules are ionized by electrons (typically of ~70 eV) produced by W cathode. Ions are then accelerated and focused into the second section, the mass filter, which consists of four parallel bars forming an electrical quadrupole field. The applied voltages affect the trajectory of ions traveling down the flight path centered between the four rods. For given voltages, only ions of a certain mass-to-charge ratio pass through the quadrupole filter and all other ions are thrown out of their original path. A mass spectrum is obtained by monitoring the ions passing through the quadrupole filter as the voltages on the rods are varied. The last section of the spectrometer is the ion detector which contains a secondary electron multiplier [28].
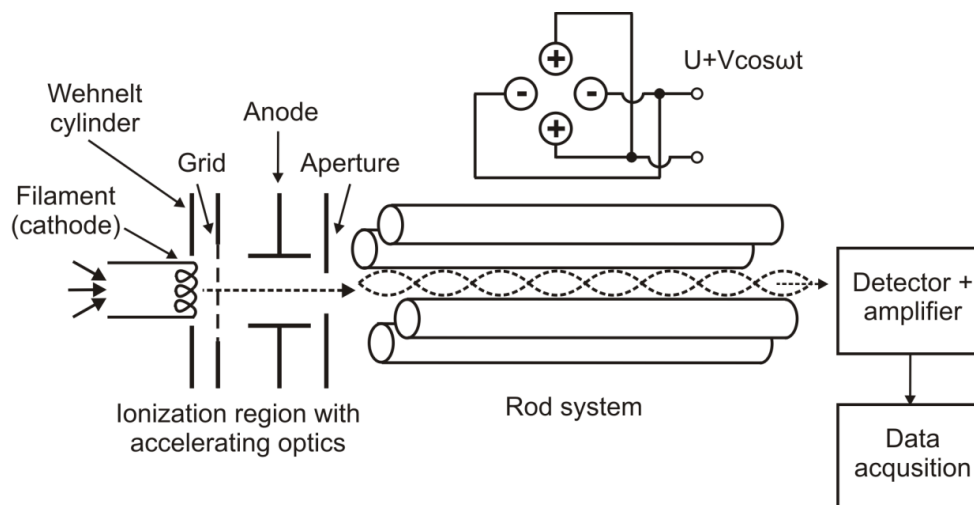

Figure 2.15 Schematic representation of QMS setup for TPD experiment

20

Among the range of surface processes which can occur on gas-solid interface such phenomena as adsorption and desorption are important for understanding of interatomic matter interaction. In surface science adsorption is implied as a process of concentration of species from a gas phase on the surface of a solid. The rate of adsorption is governed by the rate of impingement of molecules at the surface and the sticking coefficient. This flux per unit surface area (F, $molecules·m^{-2}·s^{-1}$) is given by the Hertz-Knudsen equation:

$$F = \frac{P}{\sqrt{2\pi mkT}} \qquad (2.15)$$

where P is gas pressure, $N·m^{-2}$, k is Boltzmann's constant ($1.38×10^{-23}$ $K·J^{-1}$), m is molecular mass of the impinging species, kg and T is the absolute temperature. The rate of adsorption (R_{ads}) is

$$R_{ads} = FS \qquad (2.16)$$

Depending on the nature of the interaction-potential there is a certain probability that the atom/molecule is not immediately scattered back into the gas-phase but comes to reside at the surface. The probability of this event is referred to as the sticking coefficient (S) and takes a value from 0 to 1 where the value of 1 means that all atoms/molecules impinging the surface spend significantly longer time at the surface compared to in the direct scattering process. It is essential here to mention that S depends on the substrate temperature as well as on the temperature of the incoming molecule, but also it strongly depends on the number of available adsorption sites at the surface, decreasing with decreasing number of available adsorption sites. In the case of high availability of surface adsorption sites, and low temperatures at which adsorbate can form condensed multilayers, one can assume S to be essentially constant.

Adsorption of atoms or molecules from the gas phase onto a solid surface occurs when attractive forces exist at short distance between them. There are two principle modes of adsorption on surfaces: physisorption and chemisorption. Physisorption is a weak bonding, with typically low enthalpy values 20-40 $kJ·mol^{-1}$, characterized by the lack of a true chemical bond between adsorbate and surface, i.e. no electrons are shared, not saying that there cannot be significant electron rearrangement in the molecule upon adsorption. So, the

basis of distinction is the nature of the bonding between atoms or molecules and surfaces. The weakest interaction which can lead to bonding between a surface and an adsorbate is the attractive van der Waals interaction, which originates from the interaction of a fluctuating dipole in the adsorbate with a polarizable surface. A van der Waals bonding between two molecules can be described as the interaction between two point dipoles. In the case of bonding to a surface, the attractive potential has a r^{-3} dependence. However, as the atom is brought very close to the surface, the overlapping of the electron cloud of the adsorbate and the substrate leads to a steep increase of kinetic energy of the electrons and hence a high repulsive potential as a result of the Pauli exclusion principle. Thus a physisorption potential is the sum of the repulsive and attractive Van der Waals contributions [30] (see Fig. 2.16, potential energy diagrams).

Chemisorption includes also all other types of interactions resulting in a stronger net chemical bonding to the surface compared to physisorption. Chemisorption occurs when there is an overlap between the electronic orbitals of the adsorbate and the surface, leading to the formation of chemical bonds of energies typically exceeding 50 kJ·mol^{-1}. The bond can be predominantly ionic or covalent. There are three types of chemisorption: molecular chemisorption (a), non-activated dissociative chemisorption (b) and activated dissociative chemisorption (c) (see Fig. 2.16) [27]. The potential energy curve is described by a combination of the physisorption and chemisorption. The left region from the crossing point in the figure is dominated by the chemisorption. The depth of the adsorption well is a measure of the strength of the binding to the surface and is represented as adsorption energy (E_{ads}). The desorption of an adsorbed species from a surface is considered to be the reverse process of adsorption. For cases (a) and (b), the desorption energy (E_{des}) is equal to E_{ads}. The dissociative chemisorption is often an activated process, which means that an activation barrier (E_{act}) needs to be overcome. E_{des} then can be equated:

$$E_{des} = |E_{ads}| + |E_{act}| \qquad (2.16)$$

The potential energy diagram for an activated dissociative chemisorption process is shown on Fig. 2.16(c). A diatomic molecule approaching the surface from a large distance first physisorbs on the surface. If a molecule possesses kinetic energy enough to overcome the activation barrier, the molecule may dissociate. The dissociated species can be bonded to

the surface in a chemisorption state. The corresponding potential curve of two atoms differs from that of the molecule at the large distance by the dissociation energy of E_{diss}.
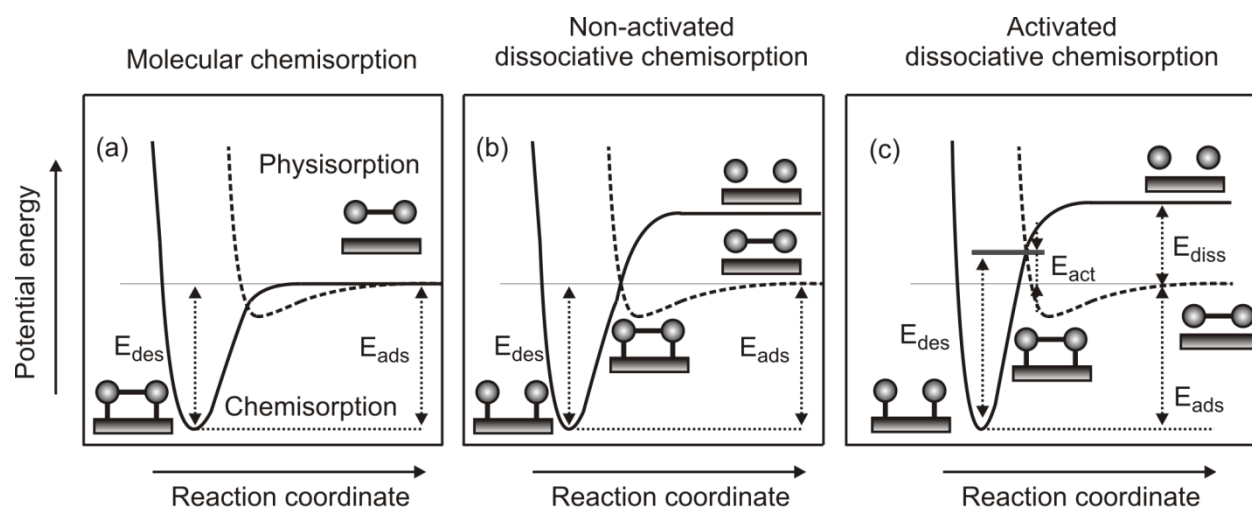
Figure 2.16 Potential energy diagrams for a diatomic molecule approaching and interacting with a solid surface

The energetics and kinetics of adsorption can be understood by evaluation of the TPD data [31-33]. Fig. 2.17 schematically shows a typical TPD spectrum (pressure-temperature curve). The profile of desorption is characterized by a desorption peak - maximal concentration of desorbing species at certain temperature in agreement with the Boltzmann distribution. Each peak corresponds to various desorbing species. The area under a peak is proportional to the amount of adsorbed species. The position of the peak (the peak temperature) is related to the enthalpy of adsorption. TPD provides information on the strength of the bond between adsorbate and substrate.

Figure 2.17 Schematic TPD spectrum

The experimental aspects of thermal desorption spectroscopy are based on the concepts of adsorption and desorption. If a solid with a surface free of adsorbed particles is placed in a gas medium, the process of adsorption will commence. Under static conditions, this process will continue in static until an equilibrium concentration of adsorbed particles is reached. If the solid surface under consideration is placed inside in a chamber of volume (V), which is under a constant evacuation at speed S, and the gas is leaked at a constant rate (L), 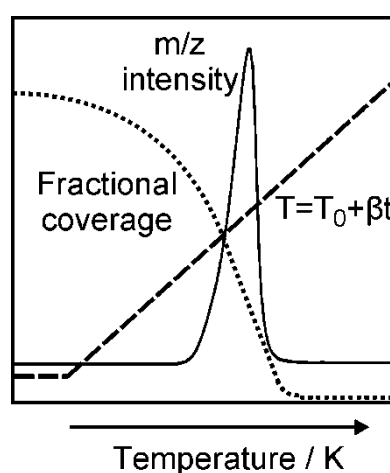the above equilibrium concentration can be described in terms of the steady-state pressure (p_{eq}) inside the chamber:

$$L = KSp_{eq} \qquad (2.17)$$

Here K represents the proportionality constant ($K = 3.27 \times 10^{19}$ molecules·l^{-1}, at $p = 1$ torr and $T = 295$ K). If the sample surface is heated at a constant rate, the gas pressure inside the chamber increases due to the flux of desorbing particles. Assuming no re-adsorption of the desorbing particles, the mass balance of particles leaving and entering the chamber is given by adsorption and desorption processes:

$$A\frac{dN}{dt} + L = KSp + KV\frac{dp}{dt} \qquad (2.18)$$

where A is the surface area of the adsorbent, dN/dt is the rate of desorption and p is the instantaneous pressure inside the chamber. Adsorption on the walls of the system has also been neglected. Using Eq. 2.17, and substituting $\Delta p = p - p_{eq}$, the equation of mass balance [Eq. 2.18] can be simplified as

$$\frac{d\Delta p}{dt} + \frac{\Delta p}{\tau} = a\frac{dN}{dt} \qquad (2.19)$$

Here $a = A/KV$ and $\tau = V/S$. τ is the characteristic pumping time. Depending on the magnitude of the pumping speed, two experimental scenarios can be identified. At a small pumping speed ($\tau \to \infty$), the desorption rate is proportional to the first derivative of pressure with time ($dN/dt \sim d\Delta p/dt$). Alternatively (for the most part of TPD studies), at high pumping speed ($\tau \to 0$), desorption rate is proportional to the pressure ($dN/dt \sim \Delta p$).

Analysis of desorption signals is based on treating the desorption process as a kinetic phenomenon. The kinetics of the desorption process follows the rate law with Arrhenius type behavior described as:

$$R_{des} = k_{des}\theta^n = v \, exp\left(-\frac{E_a^{des}}{RT}\right)\theta^n \tag{2.20}$$

where R=8.314 J·K^{-1}·mol^{-1} is the universal gas constant, T is the absolute temperature in K, Θ is the coverage ($0 \leq \Theta \leq 1$), v is the pre-exponential frequency factor (in many cases $v = 10^{13}$ s^{-1} is a good approximation), n is the desorption order, and E_a^{des} is the desorption activation energy, kJ·mol^{-1}. A frequently used basis for the evaluation of kinetic parameters from TPD spectra is known as the Polanyi-Wigner equation defining the rate of desorption R_{des}:

$$R_{des} = -\frac{d\theta}{dt} = -\frac{d\theta}{dT}\frac{dT}{dt} = -\frac{d\theta}{dT} = \frac{v(\theta)}{\beta} exp\left(-\frac{E_a^{des}(\theta)}{RT}\right)\theta^{n(\theta)} \tag{2.21}$$

here β is heating rate in K·s^{-1}. Initially the increasing of the temperature results in an exponential rise of the desorption rate. At the same time coverage of the surface decreases. The parameters E_a^{des}, n, and v should generally be considered as functions of coverage and may in cases of complex kinetics (e.g., a phase equilibrium on the surface) also depend on desorption temperature, which is a function of the heating rate. That means that desorption parameters can depend on the conditions of the TPD experiment.

The surface coverage Θ is a function of the gas pressure over the sample. It is characterized be the Langmuir adsorption isotherm which is widely used for the discussion of adsorption/desorption phenomena [34]. The concept is based on the following assumptions: a - adsorption is localized, i.e., the adsorbed particles are immobile; b - the substrate surface is saturated at Θ = 1 ML (monolayer), *i.e.*, when all adsorption sites are occupied, c - there are no interactions between the adsorbed particles.

The desorption order, if interpreted as the molecularity of an elementary reaction, allows insight into the nature of the rate-limiting step of the desorption process, which is, from the kinetic point of view, in general a consecutive reaction. From the molecularity of the desorption process one can often draw conclusions about the state of the adsorbate itself. Zero-order desorption (n=0) takes place (see Fig.2.18 a), if the desorption rate does

not depend on the coverage. The spectra are typically asymmetric and show all the same leading edge, while the temperature of maximum desorption shifts to higher values with increasing initial coverage. First-order desorption (n=1) spectra have symmetric line shapes (Fig.2.18 b), the peak temperature of which is independent of the initial coverage. Second-order desorption (n = 2) is typical for dissociative adsorption (see Fig.2.18 c). In this case, the peaks are symmetric, and the temperature at maximum desorption shifts to lower values with increasing initial coverage.
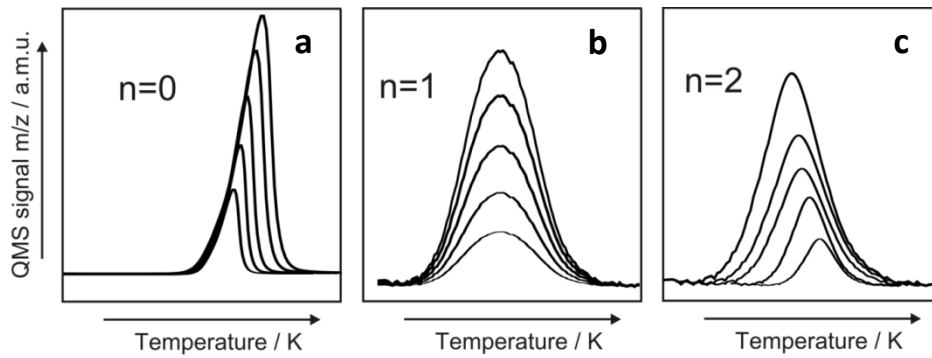

Figure 2.18 Orders of desorption process. Sets of TPD profiles illustrate various desorption kinetics: (a) - zero order, (b) - first order, (c) - second order.

In the literature, several methods for evaluating the desorption activation energies, prefactors and orders of desorption have been described, including mostly Redhead's analysis, leading edge analysis and complete analysis.

In 1962 Redhead [33] derived a simple relation between the desorption activation energy E_a^{des}, the peak maximum temperature T_{max} and the desorption order ν assuming that activation parameters are independent of surface coverage and that desorption followed first order kinetics. The maximum in the desorption rate occurs when dR_{des}/dT=0. Redhead has shown that the desorption rate equation for n=1 can be solved to obtain:

$$\frac{E_a^{des}}{RT_{max}^2} = \frac{\nu}{\beta} exp\left(-\frac{E_a^{des}}{RT_{max}}\right)$$
(2.22)

Solving Eq.2.22 for E_a^{des} provides:

$$E_a^{des} = RT_{max}\left(ln\frac{\nu T_{max}}{\beta} - ln\frac{E_a^{des}}{RT_{max}}\right)$$
(2.23)

The second term in brackets is small relative to the first and is estimated as 3.64. The error introduced through this estimate is less than 1.5% for $10^8 < v/\beta < 10^{13}$ K^{-1}. The Redhead method is often employed to extract activation energies from a single peak desorption spectrum.

Leading edge analysis was introduced by Habenschaden and Küppers in 1984 [31]. According to this method it is expected that in this small temperature range ($\sim$ 4% of spectra), the variation of v can be neglected, and θ is close to the initial coverage. The leading edge of the TPD curve fits the Polanyi-Wigner equation (Eq. 2.21). The desorption rate is proportional to the intensity of the TPD trace. Here the equation becomes:

$$R_{des} = A \, v \, \theta^n exp\left(-\frac{E_a^{des}}{RT}\right) \qquad (2.24)$$

where A is proportionality constant. Taking logarithms of both sides of this equation leads to:

$$lnR_{des} = nln\theta + lnA + lnv - \frac{E_a^{des}}{RT} \qquad (2.25)$$

If lnR_{des} is then plotted against 1/T, from the slop of such Arrhenius plot the value of E_a^{des} can be determined. From the intercept with the ordinate the frequency factor v can be determined provided that reaction order and coverage are known. If lnR_{des} is plotted against $ln\theta$ at a fixed temperature, the slop will be *n*, order of desorption. The great advantage of this method is that it requires a minimum of assumptions. A drawback is the use of the leading edge for the analysis because the signal/noise ratio in this region of low desorption rates is inherently low.

The first complete analysis of TPD was given in 1975 by King [32]. Fig. 2.19 illustrates the procedure: a coverage θ is chosen (e.g. 0.15 ML); the points corresponding to θ=0.15 ML on all TPD curves are found. This gives a pair of (R_{des} and T) values from every curve with initial coverage larger than 0.15 ML. An Arrhenius plot of all lnR_{des} versus 1/T values for this particular coverage yields E_a^{des}. The prefactor follows from the intercept $nln\theta + lnv$, when the order of desorption is known. For coverage above 0.1 ML the term $nln\theta$ is much smaller than lnv, and could be ignored. The pre-exponential factor can be regarded as representing

27

the frequency of attempts of the adsorbed particle to escape the chemisorptive potential. The values determined vary by at least four orders of magnitude, from 10^{12} to 10^{16} s^{-1}.
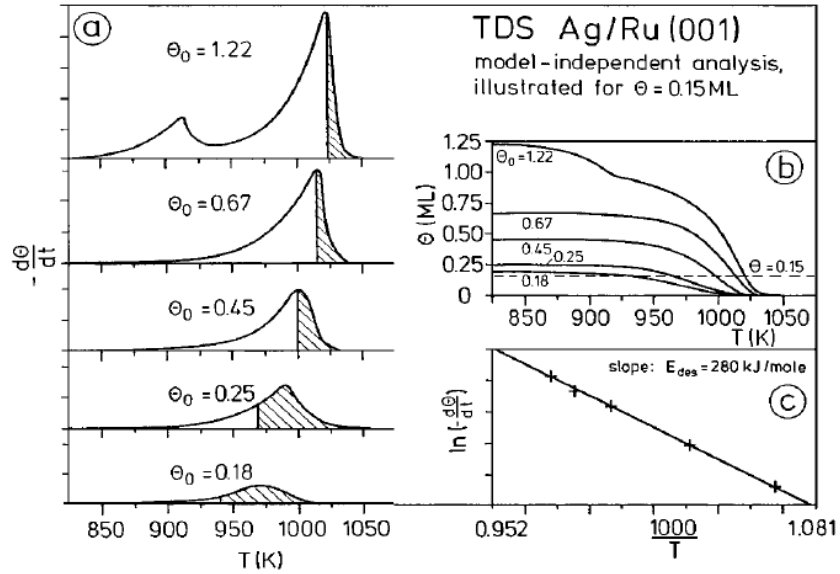

Figure 2.19 Complete analysis of TPD data. (a) The spectra are integrated to determine points on the spectra corresponding to a fixed coverage. (b) A pair of (R_{des}, T) values for every desorption trace are given, from which an Arrhenius plot is made. (c) The slope yields the activation energy [28]

The transition state theory of reaction rates gives the link between macroscopic reaction rates and molecular properties of the reactants, such as translational, vibrational and rotational degrees of freedom [28]. The desorption of a molecule M proceeds (see Fig.2.20):

$$M_{ads} \xrightarrow{K^{\#}} M_{ads}^{\#} \xrightarrow{kT/h} M_{gas} \qquad (2.26)$$

where M_{ads} is the adsorbed molecule; $M_{ads}^{\#}$ is the molecule in the transition state for desorption; $K^{\#}$ is the equilibrium constant for the excitation of M_{ads} into the transition state; k is the Boltzmann's constant; h is the Planck's constant; T is the temperature; M_{gas} is the molecule desorbed in the gas phase.
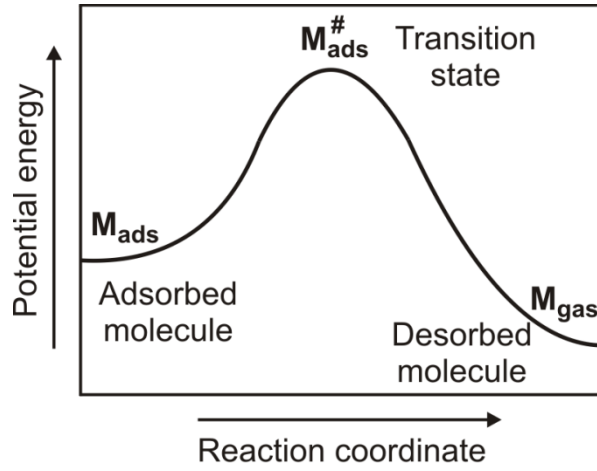
28

Figure 2.20 Desorption process in terms of the transition state theory

For desorption, the reaction coordinate is the vibration of the molecule with respect to the substrate. The chance that the adsorption bond breaks is given by the factor kT/h. Therefore the rate constant of desorption in the transition state theory is:

$$K_{des} = K_1 K_2 = K^\# \frac{kT}{h} = \frac{Q^\#}{Q} exp\left(-\frac{E_{ads}}{RT}\right)\frac{kT}{h} \tag{2.27}$$

where $Q^\#$ is the partition function of $M_{ads}^\#$, Q is the partition function of M_{ads}, E_{ads} is the adsorption energy. The partition function Q contains translational, vibrational and rotational terms:

$$Q = Q_{trans}Q_{vib}Q_{rot} \tag{2.28}$$

$$Q_{trans} = l\frac{\sqrt{2\pi mkT}}{h}; \quad Q_{vib} = \frac{1}{1-exp(-h\nu/kT)}; \quad Q_{rot} = \frac{8\pi^2 IkT}{h^2} \tag{2.29}$$

where l is the characteristic linear dimension of an adsorption site; m is the mass of the molecule M. ν is the vibrational frequency; I is the moment of inertia of the molecule M. The total partition functions are the products of each term for each individual translation, vibration and rotation. The simpliest case arises if the partition functions Q and $Q^\#$ are almost equal. This corresponds to a transition state that resembles the ground state of the adsorbed molecule. The activation energy E_{act} equals to E_{ads} +kT for desorption through a tight transition state. According to the definition of the activation energy:

$$E_{act} = -RT^2\frac{\partial}{\partial T}lnK_{des} \tag{2.30}$$

29

Comparison with Eq. 2.27 results in the prefactors equal to $\frac{ekT}{h}$, $1.6 \times 10^{13} s^{-1}$ at 300 K. Higher pre-exponential factors are obtained when the molecule rotates or moves in the transition state, indicating rather loose transition state, for example the prefactor for desorption of CO from Ru(0001) is in the range of 10^{15} to 10^{16} s^{-1}.

2.2.4 Gas chromatography (GC)

GC represents a widely applied analytical tool for chemical compounds identification in a mixture based on their separation between the mobile gaseous phase and the stationary phase. The method is practically realized in a gas chromatograph (GC).

The operational principle and major parts of the GC involved in the experimental procedure are schematically presented on Fig.2.21 (also see general overview on Fig. 2.3). Upon manual or automated sampling by the injector the analyte mixture is introduced in the GC, vaporized in a heater if necessary and diluted by a carrier gas (mobile phase). Then the gas flow by means of a rotary valve enters the column, a tube filled (packed) or coated (capillary) with an immobile material, where the chromatographic separation takes place through a distribution of components due to molecular interaction with the column material. The column is thermostated in the oven, a section used for the temperature variation. Further divided substances in the order of separation follow to the detector where they are finally analyzed utilizing specific physical properties. An electronic signal produced by the detector is plotted against time by the computer assisted software as a chromatogram. The latter consists of a number of peaks corresponding to components in the sample. The peak integrated area shows the concentration of a certain substance while the peak position (time) refers to its chemical nature [35].

Distribution of a component is determined by its relative affinity for the two phases. Those solutes interacting more strongly with the stationary phase will be retained longer in the column. Molecular interaction results from intermolecular forces that are electrical in nature. In GC such types termed as *dispersion forces* and *polar forces* are important. All interactions between molecules are composites of these forces. Dispersion forces arise from charge fluctuations throughout a molecule resulting from electron/nuclei vibrations. Polar

interactions arise from electrical forces between localized charges resulting from permanent or induced dipoles.
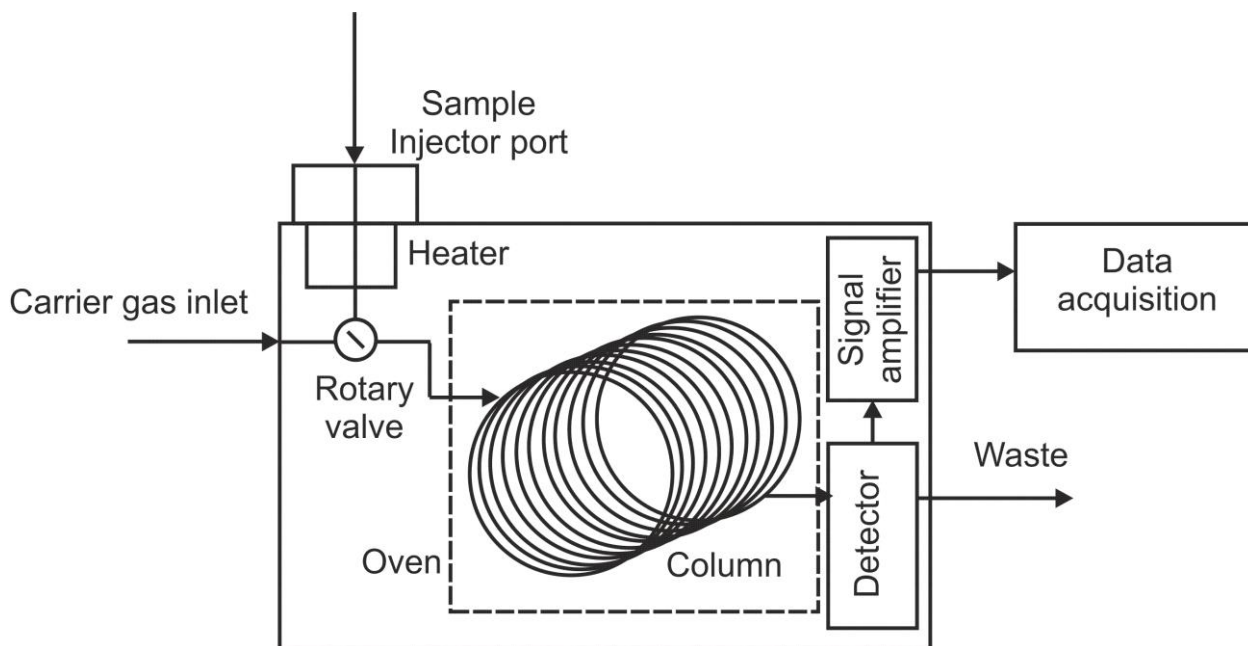

Figure 2.21 Operational principle of a general purpose gas chromatograph. Pneumatic control is not shown.

The mathematical background for quantitative analysis in GC relies on the basics of plate and rate theories. The concept of the plate theory was originally proposed for the performance of distillation columns. However, Martin and Synge (1941) first applied the plate theory to partition chromatography. The theory assumes that the column is divided into a number of zones called *theoretical plates.* One determines the zone thickness or height equivalent to a theoretical plate (HETP) by assuming that there is perfect equilibrium between the gas and liquid phases within each plate. The resulting behavior of the plate column is calculated on the assumption that the distribution coefficient remains unaffected by the presence of other solutes and that the distribution isotherm is linear. The diffusion of solute in the mobile phase from one plate to another is also neglected [36].

Eluting from the column the component is characterized by the (absolute) retention time t_R- the amount of time that elapsed from injection of the sample to the recording of the peak maximum of the component band (peak) by the detector. This term is commonly used as the adjusted retention time t_R'- the solute total elution time minus the retention time for an unretained peak of the mobile phase (or holdup time -the time necessary for the

carrier gas to travel from the point of injection to the detector; this is characteristic of the instrument, the mobile phase flowrate, and the column in use):

$$t_R' = t_R - t_M \tag{2.31}$$

The column efficiency or sharpness of the peak is defined by the theoretical plate number N. Assuming the peak to have normal (Gaussian) distribution (see Fig. 2.22) N could be found:

$$N = \left(\frac{t_R}{\sigma}\right)^2 = 16 \left(\frac{t_R}{\omega_b}\right)^2 = 5.54 \left(\frac{t_R}{\omega_h}\right)^2 \tag{2.32}$$

where σ is the peak band broadening, $\omega_b = 4\sigma$ is the peak width at base and $\omega_h = 2.35\sigma$ is the peak width at the half of the height.
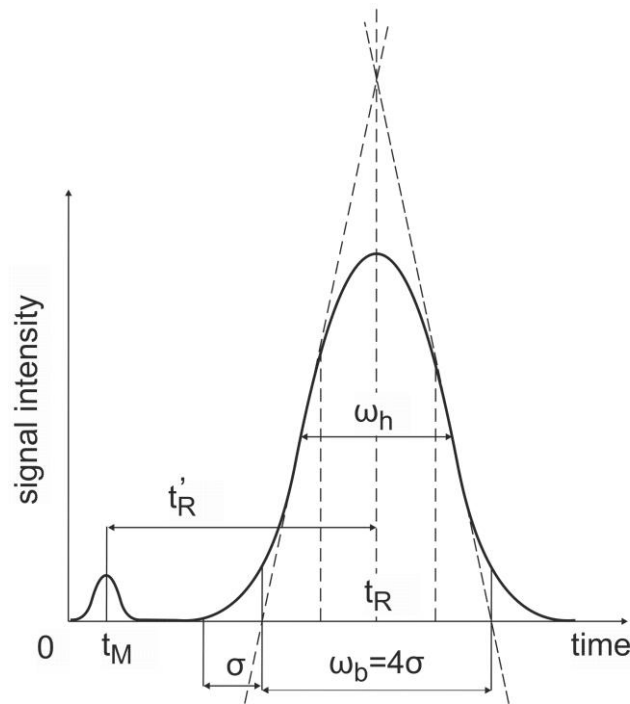

Figure 2.22 Schematic drawing of a component peak on a chromatogram.

Having calculated the number of theoretical plates and knowing the length L of the column, one may determine the HETP (or simply H):

$$H = HETP = \frac{L}{N} = \frac{L}{16} \left(\frac{\omega_b}{t_R}\right)^2 \tag{2.33}$$

Thus Eq.2.33 shows that the HETP represents the peak broadening as a function of retention time. In a gas chromatographic column, each component will yield different N and HETP

values. Those solutes with high retention will result in greater numbers of theoretical plates and thus lower HETP values.

Peaks resolution defined as a degree of separation between neighbour peaks of two components 1 and 2 in terms of their average peak widths can be written as follow:

$$R_s = \frac{2\Delta t_R}{\omega_1 + \omega_2} = \frac{2(t_2 - t_1)}{\omega_1 + \omega_2} \qquad (2.34)$$

Capacity (retention) factors k is a measure of the ability of the column to retain a sample component. When an analyte retention factor is less than one, elution is so fast that accurate determination of the retention time is very difficult. High retention factors (greater than 20) mean that elution takes a very long time. Ideally, the retention factor for an analyte is between one and five. Selective components distribution is characterized by the selectivity factor k'. It is in turn expressed through the ratio of k for two components 1 and 2:

$$k = \frac{t'_R}{t_M} = \frac{t_R - t_M}{t_M} \qquad k' = \frac{k_2}{k_1} = \frac{t'_{R2}}{t'_{R1}} \qquad (2.35)$$

The separation factor α is the ratio of the distribution constants K for substances 1 and 2 measured under identical conditions. By convention the separation factor is usually greater than unity:

$$K = \frac{C_s}{C_g} \qquad\qquad \alpha = \frac{K_2}{K_1} \qquad (2.36)$$

where C_s is a component concentration in the stationary phase and C_g its concentration in the mobile phase. Finally, taking into account capacity and separation factors the resolution could be given by a commonly used expression as follows:

$$R_s = \frac{1}{4}(N)^{1/2}\left(\frac{\alpha - 1}{\alpha}\right)\left(\frac{k}{1+k}\right) \qquad (2.37)$$

where N and k refer to the later-eluting compound of the pair. If two peaks are separated by a distance 4σ, then $R_s = 1$. If the peaks are separated by a 6σ, then $R_s = 1.5$ which practically means the beginning of an effective separation. If further to consider the non-negligible time for substances in the mobile phase, this gives the *effective* theoretical plates related to the number of theoretical plates:

33

$$N_{eff} = N \left(\frac{k}{1+k}\right)^2 \tag{2.38}$$

Although HETP is a useful concept, it is empirical. One must use the rate theory to explain chromatographic behavior. The rate theory is based on such parameters as rate of mass transfer between stationary and mobile phases, diffusion rate of solute along the column, carrier-gas flowrate, and the hydrodynamics of the mobile phase. The *van Deemter equation* (1956) is used for describing the gas chromatographic process. The equation was derived from consideration of the resistance to mass transfer between the two phases as arising from diffusion:

$$H = A + \frac{B}{u} + Cu \tag{2.39}$$

where *A* - eddy diffusion term, *B* - longitudinal or ordinary diffusion term, *C* - or resistance to mass transfer term and u is a linear gas velocity. A representation of this equation is given in Fig. 2.23, which shows the effect of *H* with changes in linear gas velocity. This equation predicts that for maximum column performance, the contribution of each term must be minimized while maintaining a constant linear flowrate.

In the case of a capillary column, the *A* term is equal to zero because there is no packing material. Thus, Eq. 2.39 simplifies to abbreviated expression often referred to as the *Golay equation* (1957):
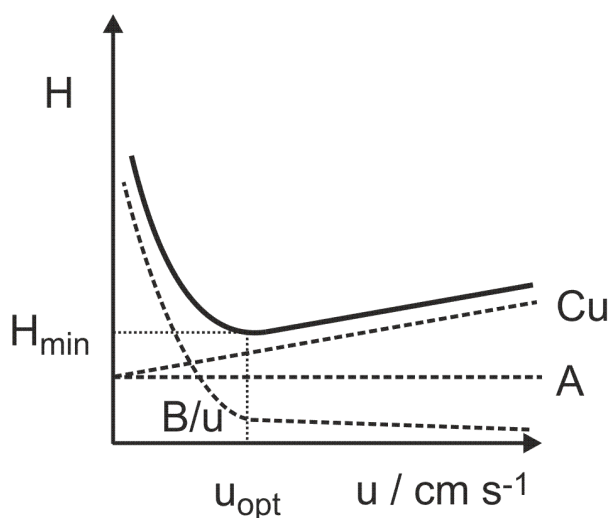
$$H = \frac{B}{u} + Cu \tag{2.40}$$

Figure 2.23 Van Deemter plot. Change in *H* versus linear gas velocity *u*

In the practice of chromatographic instrumentation the central role is played by columns. They are categorized into two classes by their operational principle (see Fig. 2.24). The first type originally introduced is packed one when the separation of the gas mixture takes place in a column filled with particles of a solid occupying the major volume. In chemical analysis packed columns were replaced by capillary columns in the early 1980s with mass production of fused silica tubes. Inner walls of a capillary column with the narrow diameter are coated with a thin layer (μm) of non-volatile immobilized liquid or solid substance as a stationary phase. This offered a tremendous improvement in resolving power compared to a conventional packed column. Such a column is also often referred to as an open tubular column. The high permeability or low resistance to carrier-gas flow of capillary column enables a very lengthy column to generate a large number of theoretical plates.
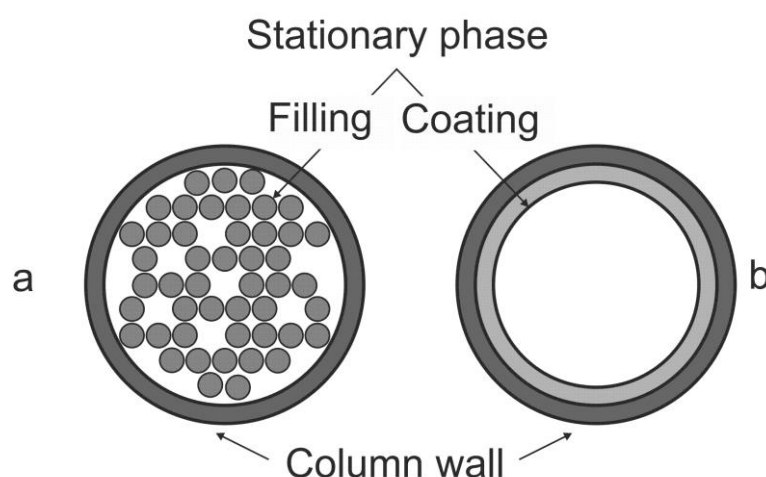

Figure 2.24 Representative flow through chromatographic columns: a- a packed column, b - a capillary column

The proper selection of a stationary phase/column depends on the nature of mixed substances to be separated. Generally, one can be guided by the rule of matching polarity: polar components require a polar stationary phase material and vice versa. Among the general purpose polar materials polysiloxanes, polyethylene glycol are widely used for various organics analysis. Graphitized carbon and porous polymers belong to non-polar adsorbents and are applied in hydrocarbons separation. Molecular sieves divide well noble and permanent gases.

The optimal chromatographic performance of the column is defined by combination of its inner diameter, length, the carrier gas flow (linear velocity), the stationary phase

thickness and the temperature mode. The larger diameter/flow/higher temperature facilitates shorter analysis times but results in lower peaks resolution and backwards. The length change influences in a reverse way: a longer column will have higher resolution compensated by the increased time of detection. Temperature-programmed operation is preferred rather than isothermal when separating components with close physico-chemical properties (molar mass, boiling point). A thicker layer of the stationary phase film causes the magnification of the column capacity (mass of retained analyte) and the retention time as well. Finding the balance of all parameters depends on the particular experimental problem (and the column price) [36].

To register the chemical substances a wide variety of detectors is nowadays applied in GC technique, often coupled with other methods. The detector performance is characterized by a number of important parameters. The limit of detection (LOD) is the concentration at which the output is equivalent to twice the noise level. The dynamic range of a detector is usually given as a concentration ratio to LOD within which a concentration dependent output is produced. The most significant region of the dynamic range is the linear range. An ideal gas chromatographic detector should have low LOD and a large linear dynamic range (five to six orders of magnitude). The response factor is the ratio of the signal (integrated area)-to-sample size and must be stable within the linear dynamic range. A selective detector responds to compounds containing a specific heteroatom while a universal detector responds to any component. Detectors can be divided into two groups: mass flow detectors, which respond to the mass of sample component reaching the detector per unit time, and concentration-sensitive detectors, which provide an output that is directly proportional to the concentration of a sample component in the mobile phase [37].

The most popular detector in GC practice stays a thermal conductivity detector (TCD or katharometer) due to its cost and accuracy. The TCD detector responds to any substance different from the carrier gas. The detector (see Fig.2.25) contains two filaments: one exposed only to carrier gas, while the other is exposed to the carrier gas for sample analysis. Instead of a direct measurement of filament temperature, the filament resistant, which is a function of temperature, is measured. When the gas for the sample analysis is only carrier gas, the two filaments can be balanced. Such a scheme is called the Wheatstone bridge. The

ability of a colliding molecule to carry off heat depends on its thermal conductivity. Hydrogen and helium have high thermal conductivity and therefore will be more efficient at "cooling" a heated filament than other gases. When the sample cell filament is subjected not only to the carrier gas the primary signal is produced [36]:

$$\Delta R_f = -\alpha \frac{R_f^0 \Delta \lambda (T_1 - T_2)}{\lambda}$$ (2.41)

where ΔR_f is a resistance difference between two filaments, α is the temperature coefficient of resistance for the filament wire, R_f^0 the resistance at the reference temperature of 0°C, λ is proportional to the temperature difference across the cell, T_1 is the temperature of the filament wire, T_2 is the temperature of the detector.
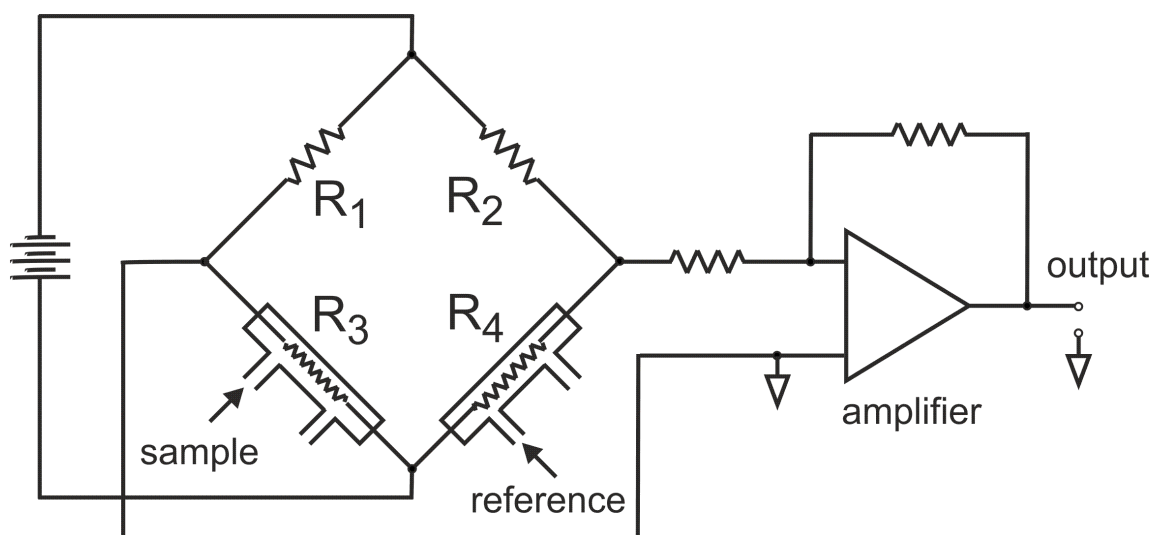

Figure 2.25 The working principle of a thermal conductivity detector. R_3 and R_4 are the resistance of the sample and reference cells respectively, R_1 and R_2 are the auxiliary resistances.

Qualitative data analysis i.e. identification of substance by the peak position (the retention time) is carried out by comparison with that of pure standards or test mixtures for the same experimental conditions and column parameters. Quantitatively the amount of each component in a mixture is found as:

$$C_i = \frac{A_i r_i}{\sum_{i=0}^{n} A_i r_i}$$ (2.42)

where A_i is integrated area of the component peak, r_i is the response factor of the detector for this substance (it could be found from a calibration curve).

Chapter 3

CO oxidation over ruthenium oxide films on Ru(0001)

3.1 Catalytic activity of Ru-based materials.

Ru(0001) is famous to interact with a broad range of versatile small molecules (often coadsorbed) like CO, O_2, H_2, NO, N_2, NH_3, H_2O, hydrocarbons, methanol [38-49] and to be active in such chemical processes as CO oxidation [50], ammonia synthesis and oxidation [51, 52] under UHV conditions. Its surface can also serve as a substrate for preparation of a wide variety of thin films. This includes oxides of transition metals (MO_X, where M=Ce, Ti, Fe, Al), silica, graphene and bimetallic alloys as ordered layers [53-59].

However, its native oxide coating the ruthenium bulk continues to attract attention in fundamental research in its own right, especially in the CO oxidation reaction at elevated pressures. The stoichiometric oxide RuO_2 growing in (110) direction on Ru(0001) surface was found to interact with CO, O_2, H_2, NO, H_2O, hydrocarbons [60-66] and catalyze CO, NH_3 and HCl oxidation [67-69] in UHV. A review of ruthenium dioxide properties and applications in comparison with metallic ruthenium was recently given by Over [70]. It turned out that CO oxidation became a very challenging topic in surface science of Ru-based catalytic materials due to discrepancies and ambiguity raised by the pressure gap and different reaction conditions what resulted in a number of phases ascribed to be reactive. The milestones of this intriguing story are provided below.

The beginning of the intensive Ru-related studies takes place at the moment when the reaction conditions were changed *from UHV to mbar pressure range of reactants* in the work of Peden and Goodman where they reported Ru(0001) to be more active than Rh and Pd in CO oxidation with stoichiometric gas ratio [71]. There they proposed the idea to explain Ru anomalous behavior and developed it further that a dense (1x1) phase of chemisorbed oxygen on Ru(0001) is the active phase in the reaction [6, 72].

Later Over and co-workers suggested that under technologically relevant conditions the Ru catalyst is represented by the $RuO_2(110)$ surface [73, 74]. Enhanced reactivity was proposed to be governed by interaction of weakly bound oxygen atoms with CO [75]. Upon the following-up studies with polycrystalline RuO_2 powder and supported Ru nanoparticles Muhler with colleagues formulated the shell-core model [76, 77]. The group of Schlögl in the studies with Ru(0001) and polycrystalline RuO_2 powder suggested that the active phase is a thin film of poorly defined oxide structure labeled as "surface oxide" [78, 79].

These investigations induced search of similar oxygen rich surface structures on other noble metal catalysts at mbar pressures. The formation of ultrathin oxide layers on Pt, Pd, and Rh and their high reactivity in CO oxidation have recently been reported [80-85]. Experiments were supported by DFT calculations with the full step-by-step analysis of the oxide formation and CO oxidation energetics over both Ru(0001) and $RuO_2(110)$ surfaces by Reuter and Scheffler [86-89].

Recently, Somorjai with coworkers presented the size-reactivity dependence of CO oxidation over core-shell Ru nanoparticles covered by a thin layer of oxide species [90]. Therefore, through a controversial interplay between experiment and theory it is now believed that the active phase is neither a chemisorbed oxygen phase nor the stoichiometric $RuO_2(110)$ but rather a very thin ruthenium oxide film of not yet well determined structure.

Systematic studies of the reactivity of "native" oxide films as a function of the film thickness have not been performed so far, although in their recent paper Goodman and co-workers mentioned similarities in the catalytic behavior of the ruthenium oxide films prepared at different oxidation temperatures [91]. Thus, the efforts to transfer the ideas introduced in Chapter 1 also to "native" oxide films have a rational background.

Such films could in principle be even formed on noble metal surfaces, provided the high chemical potential of oxygen. In this work, I have examined thin ruthenium oxide films on Ru(0001) (as well as bare Ru and chemisorbed O-phases) in the CO oxidation reaction at near-atmospheric pressures and low temperatures (400 – 470 K). In particular, my study was focused on finding the relation between the reactivity of oxide films and the film thickness.

3.2 Structure of materials and thin film preparation

Ru(0001) has hexagonal close packed *(hcp)* crystal structure with lattice constant a=2.704 Å what results in a hexagonal (1x1) LEED pattern. The major surface contaminants are Si, S and C [92]. Clean surfaces of the Ru(0001) single crystal can be obtained by several cycles of argon ion sputtering and annealing in UHV and oxygen [93]. However, it is difficult to confirm the cleanliness of Ru surface since its MNN Auger peak at 273 eV interferes with the carbon KLL peak at 272 eV. After the surface quality was proved by LEED and AES, it can be finally verified by CO TPD. CO desorption from clean Ru(0001) is characterized by a well-known profile with two peaks α_1 at ~ 460 K and α_2 at ~ 400 K corresponding to undisturbed $\sqrt{3} \times \sqrt{3}\,R30°$ and compressed CO respectively, that was revealed by Menzel with coworkers [41].

Ru(0001)-   O-(2x1)   3O-(2x2)   O-(1x1)
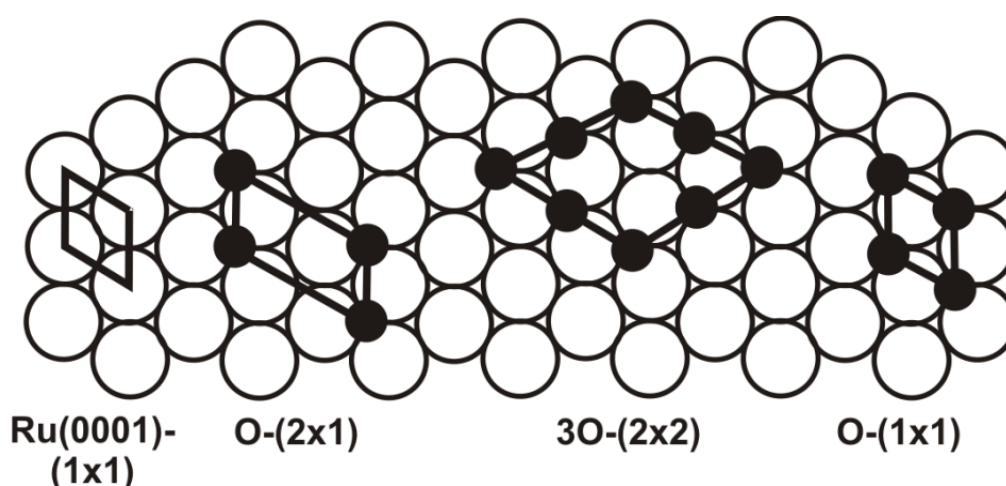(1x1)

Figure 3.1 Real space geometry of Ru(0001) and O-adlayers unit cells [70]

Several chemisorbed oxygen adlayer structures can be formed on Ru(0001). Their real space schematic representation is shown of Fig.3.1. The O(2x1)-Ru(0001) surface with the coverage Θ=0.5 ML was prepared by exposure to $2x10^{-7}$ mbar O_2 at 420-450 K for 10 min [39] giving a (2x2) hexagonal LEED pattern which originates from a coincidence of three rotational domains. Here one ML (monolayer) corresponds to a number of surface atoms that equals that of Ru atoms in the topmost layer of Ru(0001).

Upon population the surface with O-atoms its sticking coefficient decreases, and higher oxygen chemical potential is needed to attach more oxygen to the metal. The 3O(2x2)

structure with Θ=0.7 ML [94] was prepared by oxidation in $1x10^{-6}$ mbar O_2 at 1220 K for 5 min and cooling in the same oxygen pressure down to 300 K. The dense O(1x1)-Ru(0001) surface with O in hcp sites and Θ=1 ML was formed upon the crystal exposure in the HP cell to 20 mbar of pure O_2 at 450 K for 10 min in contrast to 'NO$_2$ method' [95]. The formation of the oxidic phase under UHV conditions is kinetically hindered [86].

Bulk ruthenium (IV) oxide has a rutile crystal structure where each Ru atom is completely coordinated by six surrounding oxygen atoms with a unit cell 4.51 Å × 3.11 Å [96]. But the bulk-truncated surface of new crystallographic plane e.g. (110) is terminated with rows of bridging oxygens and shows 5-fold Ru atoms called 'coordinatively unsaturated sites (cus) with missing O neighbours as shown on Fig.3.2. Single crystalline RuO_2(110) films can be grown on the hot Ru metal substrate by dosing high amounts of O_2 [73].
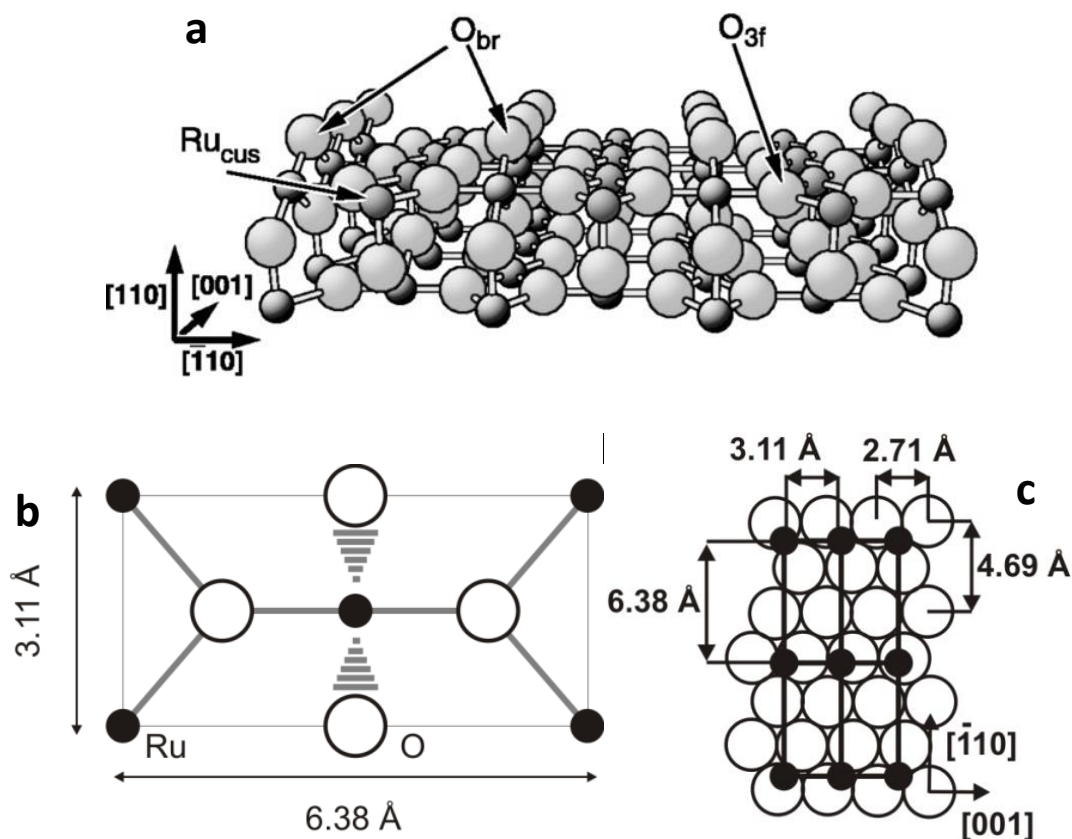

Figure 3.2 Surface geometry of RuO_2(110) [97, 98]: a - ball-stick model, b - top view on a unit cell, c - oxide domain on Ru(0001) substrate

In this work native thin oxide films on a double-side polished Ru(0001) crystal were prepared by oxidation of the crystal surface in 10^{-4} mbar of O_2 at 600 - 700 K by backfilling

entire UHV chamber. The film thickness was varied by the oxidation time and temperature. The freshly prepared oxide films all showed LEED patterns characteristic for the $RuO_2(110)$ overlayer on Ru(0001) as depicted on Fig.3.3d: it evolves from the superposition of a (1x1) hexagonal arrangement of Ru(0001) support and additional array of $RuO_2(110)$-(1x1) spots with rectangular symmetry seen as domains rotated 120° with respect to each other; in the real space the oxide has a unit cell 6.38 Å × 3.11 Å [97, 98].
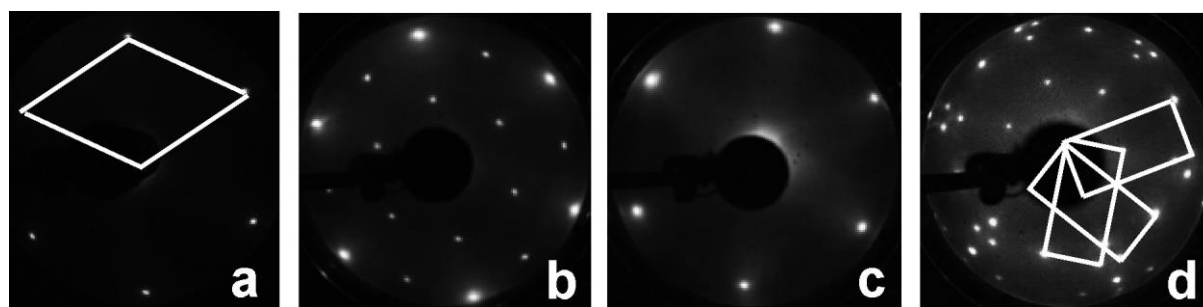
Figure 3.3 LEED patterns (70 eV) of different O-phases on Ru(0001) used in this work: a - clean Ru(0001), b - O(2x1) or 3O(2x2), c - O(1x1) and d - $RuO_2(110)$. (1×1) and (110) unit cells are indicated.

The surface composition was determined by AES using normalization to O(2×1)- and 3O(2×2)-Ru(0001) structures as the references. The nominal film thickness is presented in this work in oxygen monolayer equivalents (MLE) such that 1 MLE corresponds to the amount of the surface oxygen atoms in the (1×1)O-Ru(0001) structure. A typical Auger spectrum of an oxide film was given as an example on Fig.2.12 in Ch.2. In this work oxide films were grown up to maximal thickness ~ 7 MLE.

A characteristic CO TPD spectrum from oxide films served as an additional fingerprint [60, 99]. Based on this data it was assumed that oxide films possess the stoichiometry and ordering of $RuO_2(110)$ phase. However, to prevent any speculations about the film structure within the whole thickness interval it was decided to use symbolic nomenclature of RuO_x.

Additional structural characterization of the similarly prepared oxide surfaces was performed in another UHV chamber equipped with LEED, *scanning tunneling microscopy (STM)* and x-ray photoelectron spectroscopy (XPS) by *B. Yang, X. Yu and J.A. Boscoboinik*, members of the 'Structure and reactivity' group, Department of Chemical Physics, Fritz-Haber-Institute of Max Planck Society.

3.3 Results and discussion

3.3.1 Thickness dependence

The CO oxidation reaction was performed in a circulating mixture of CO and O_2 in the mbar-pressure range balanced by He to 1 bar. Typical kinetic curves of CO_2 production under oxidizing conditions (10 mbar CO + 50 mbar O_2) are shown in Fig.3.4a. The CO_2 production grows linearly in time during the first 10-15 min, then slows down and stops as CO is totally consumed. Characterization of the post-reacted surfaces by LEED and AES revealed practically the same surface composition and ordering, suggesting no substantial structural transformations under the reaction conditions. For all oxygen adlayer structures, the post-reacted surfaces showed solely the (1×1) LEED pattern, i.e., in contrast to the high temperature conditions (>550 K) where the oxide formation is observed during the reaction [74, 76, 78].

On Fig.3.4b reactivity data are given in terms of turnover frequencies (TOF), the number of produced CO_2 molecules per active sites and second, as calculated from:

$$TOF = \frac{V}{R} \cdot \frac{L}{T} \cdot \frac{1}{N_{Cat}} \cdot \frac{dP(CO_2)}{dt} \qquad (3.1)$$

where V=165.6 cm^3 is the volume of the HP cell (reactor) and gas lines to the GC, L=6.022·10^{23} mol^{-1} is Avogadro's number, R=8.413 $J \cdot K^{-1} \cdot mol^{-1}$ is the universal gas constant, T=300 K is the gas temperature, $N_{Cat} = 10^{15}$ is the number of active sites of the catalyst (the area of the *double*-side crystal is about 1.08 cm^2), $P(CO_2)$ is the partial pressure of CO_2, t is time. Since during the reaction the direct measurement of the partial pressure of CO_2 was not provided, it was assumed that its maximal value is equal 10 mbar as well as the initial pressure of CO, what is based on the full conversion of CO: $dP(CO_2) \sim dP(CO) \sim$ 10 mbar.

Figs.3.4 (a, b) clearly shows that thin oxide films are much more active than the clean Ru(0001) surface. The O-adlayer surfaces showed negligible reactivity, regardless of whether the surface exhibited O(2x1) or 3O(2x2) structures before the reaction, since the surface immediately transforms into the (1x1) structure upon exposure to high pressures of oxygen in the reactor. Each sample was prepared separately and used only once.
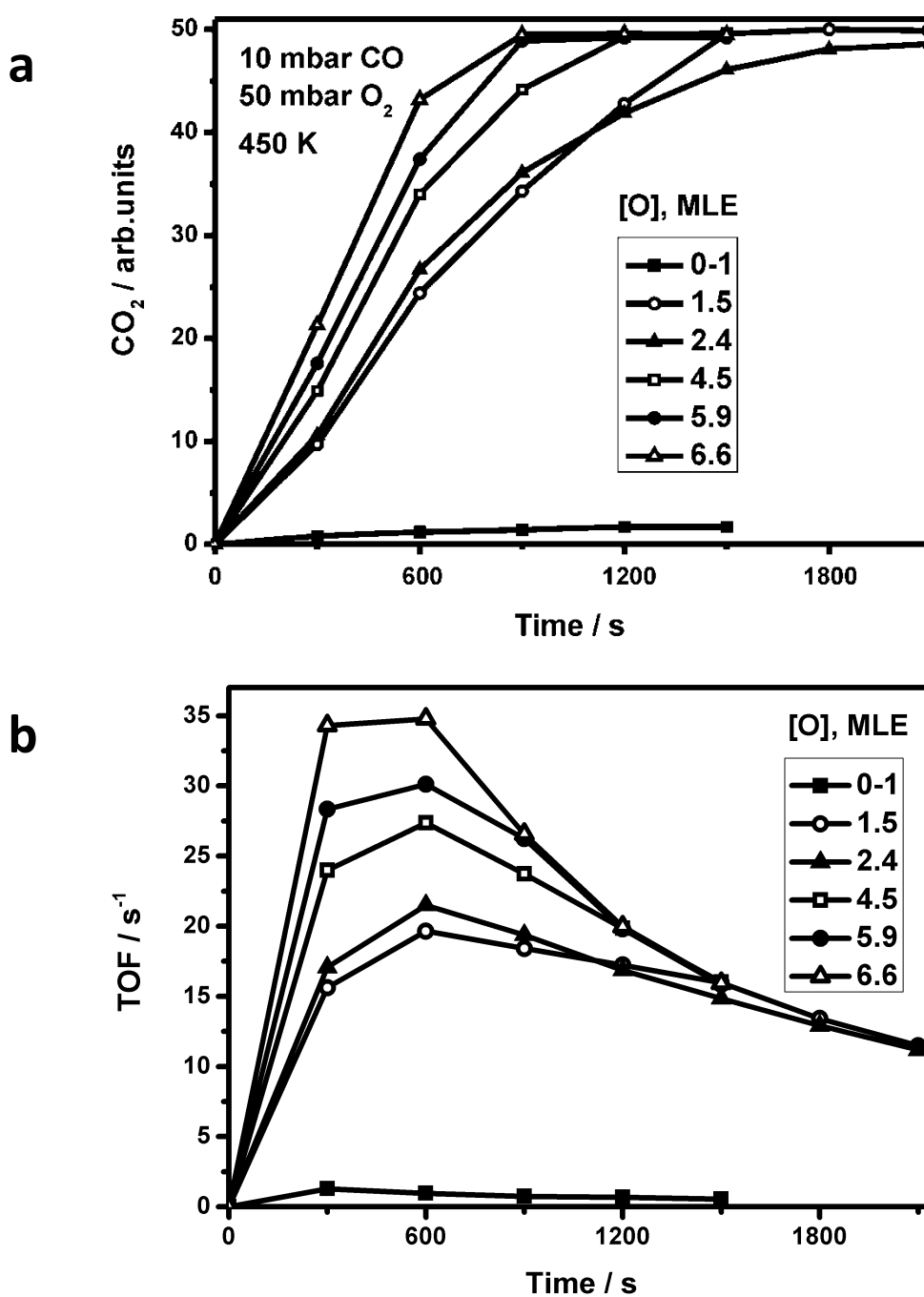
43

Figure 3.4 Reaction kinetics for CO oxidation on clean Ru(0001) crystal, O-adlayers and thin oxide films grown on Ru(0001), possessing the indicated amounts of oxygen (in MLE) prior to the reaction: a - kinetic curves of CO_2 production, b - turnover frequencies of CO_2 production.

In order to quantify the effect, the CO_2 production rate was measured within the first 10 min, although the oxide films showed substantial conversion, above 50 %. The nearly constant reaction rate even at high CO conversions implies no poisoning by CO_2 that is

accumulated in the circulating mixture. To further prove this conclusion, the following experiment has been performed as shown in Fig.3.5.

After 10 min of the reaction over a 5 MLE oxide film at 430 K the reactor was pumped out while cooling the sample to the room temperature. Then, the reactor was re-filled with the fresh CO + O_2 mixture, heated up to the reaction temperature, and the reactivity was measured again. In the beginning, the CO_2 production rate slightly diminished, most likely because of carbonaceous deposits, but it recovered to the original value as the carbon burned out in the excess of oxygen.

Indeed, when the same procedure was repeated except the sample has been flashed to 600 K in UHV prior to refilling the reactor, the reaction proceeds with the same rate from the onset. Therefore, it was concluded that the reaction does not suffer from CO_2 self-poisoning, at least under net oxidizing conditions. This finding allowed comparing the activity of oxide films even at high CO conversions.
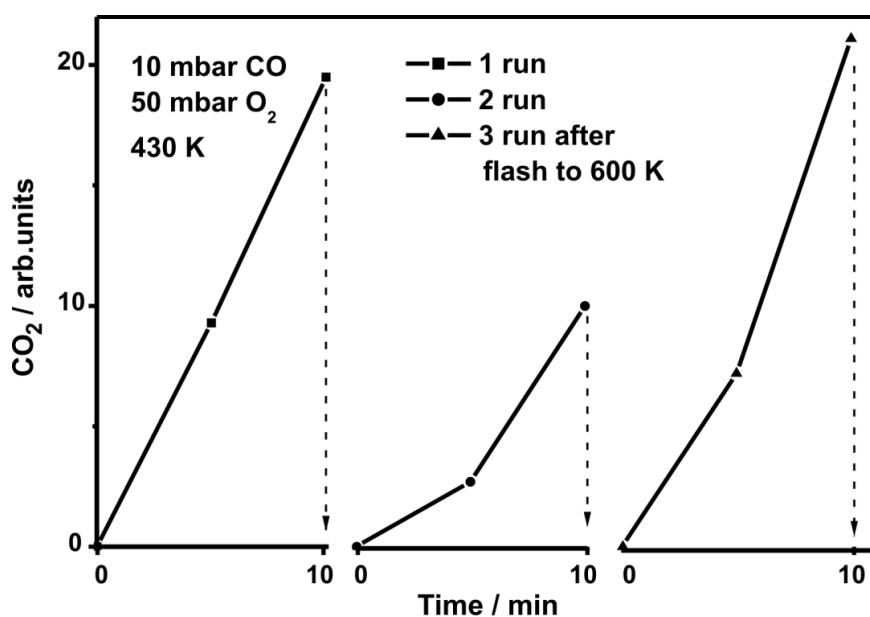

Figure 3.5 Sequential CO oxidation runs over the same 5 MLE thick RuO_x film on Ru(0001) (10 mbar CO+50 mbar O_2, balanced by He to 1 bar, 430 K).

When the reaction rates are re-plotted against the sample oxygen content prior to the reaction, Fig.3.6 clearly shows a steep increase in the reactivity upon oxygen incorporation into the Ru surface (i.e. oxygen coverage exceeds 1 MLE). Basically, the CO oxidation reaction sets in only in the presence of oxide films. Increasing of the nominal film

thickness further enhances the reactivity, but to the lower extent. These results suggest that the presence of a very thin oxide layer is, in principle, sufficient to show superior catalytic activity, i.e. in contrast to the O-chemisorbed layers which are inactive under the conditions studied. For clarity a vertical dashed line indicates a point where oxygen content of the film represents already the stoichiometry of RuO_2.
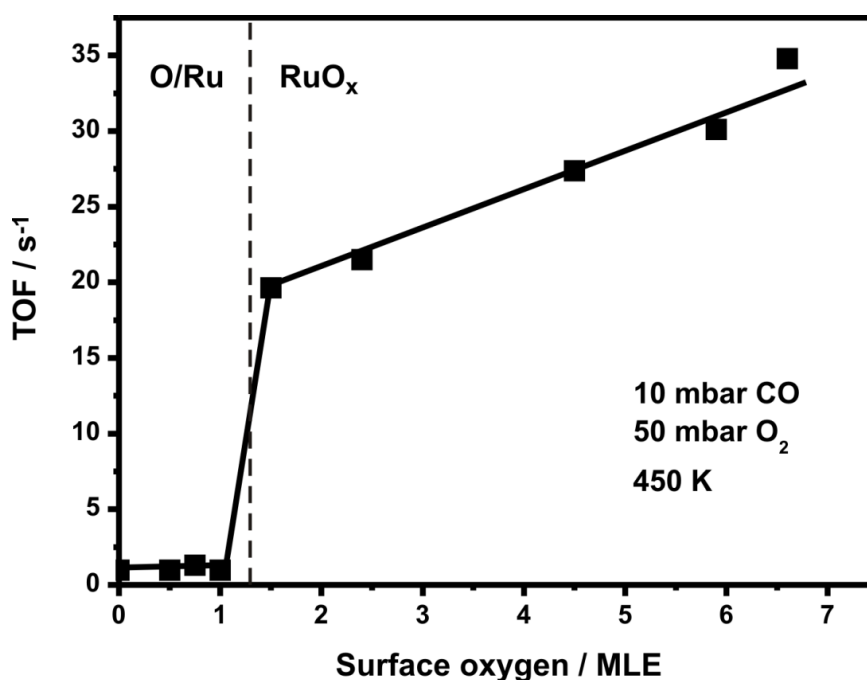

Figure 3.6 Structure-reactivity dependence of CO_2 production over RuO_x films on Ru(0001), O/Ru(0001) layers and initially clean Ru(0001) as a function of oxygen coverage measured before the reaction (10 mbar CO+50 mbar O_2, balanced by He to 1 bar, 450 K). The onset of oxide formation is marked by a vertical dashed line.

3.3.2 Active phase formation

To gain further information about the atomic structure of the films, similarly prepared films have been examined by STM in another UHV chamber (B. Yang, X. Yu, J.A. Boscoboinik), where the oxygen coverage was determined by XPS [100].

Relatively thick films (approximately 4 MLE and above) exhibited sharp LEED patterns of RuO_2(110)/Ru(0001) and showed STM images very similar to the previously reported by Over et al. [73] and Rössler et al. [101], with rectangular-shaped terraces dominating the large scale morphology (Fig.3.7a). High resolution STM images (inset in Fig.3.7a) revealed the atomic structure characteristic for the RuO_2(110) surface, where the protruding lines with a

~ 6.5 Å spacing were assigned to the bridging oxygen atoms in the bulk rutile structure of RuO_2 [97]. At these high oxygen coverages, an oxide film uniformly covered the entire crystal surface.
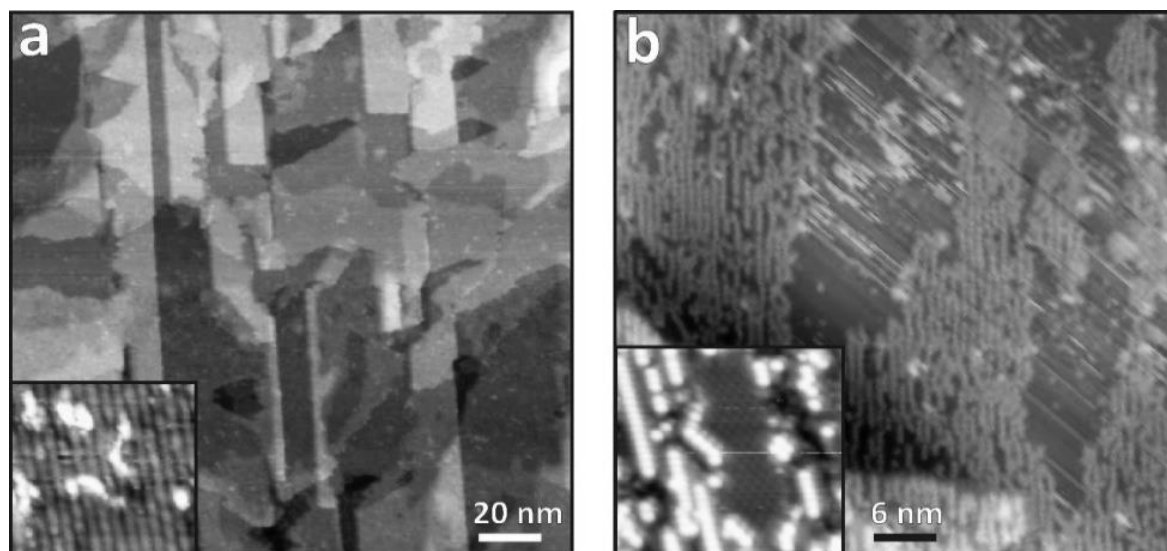

Figure 3.7 STM images of RuO_x films grown on Ru(0001): (a) Typical large-scale STM image of "thick" (> 4 MLE) films. The inset shows a high-resolution image characteristic for the RuO_2(110) surface, with a ~ 6.5 Å spacing between the protruding rows. (b) STM image of raw-like structures additionally observed on the ultra-thin films (1-2 MLE). The streaks are caused by the tip instability along the scanning direction. The inset shows atomically resolved STM image of the rows as well as 3O(2x2)-Ru(0001) structure in between [100]. The images are provided by *B. Yang, X. Yu and J.A. Boscoboinik.*

In contrast, the ultra-thin films (i.e., 1-2 MLE), showing faint diffraction spots of RuO_2(110), exhibited very heterogeneous surface, with patches of RuO_2(110) coexisting with the (1x1)O-Ru(0001) surface. In addition, new row-like structures were observed by STM as shown on Fig.3.7b. The protruding rows were primarily running along the [10-10] direction, i.e. the same as for RuO_2(110) overlayer. However, the rows exhibited a ~4.6 Å periodicity along the rows (see inset in Fig.3.7b), which is considerably larger than observed for the bridging oxygen rows on RuO_2(110), i.e. 3.1 Å. Also the spacing between the rows (e.g. ~ 9 Å, on average) is definitely larger than the distance between adjacent rows on RuO_2(110) (= 6.4 Å). For the isolated rows it was possible to see by STM that the "open" surface between the rows exhibits the honeycomb-like 3O(2x2)-Ru(0001) structure (inset in Fig.3.7b).

Tentatively, these rows have been assigned to the one-dimensional oxide structures as an intermediate state and/or precursor to the formation of RuO_2(110) overlayer.

Certainly, determination of its atomic structure needs further studies. In this respect the recent work of Over's group is interesting where it is proposed that the growth of 3D RuO_2 clusters requires high O_2 pressures only on the initial step of their formation [102]. The authors claimed no evidence of O-Ru-O trilayer formation predicted by Reuter et al. [87].

Nonetheless, thermal desorption spectra of oxygen on the oxide films of various thicknesses did not reveal any new features beyond those observed on the "thick" RuO_2(110) films. A set of preformed oxide films was subjected to mbar pressures of pure oxygen at the reaction temperature. Post-characterization with LEED and AES indicated no change in surface ordering and composition.

Upon exposure to 10 mbar O_2 at 450 K all the films studied showed O_2 desorption signal at ~ 420 K in TPD spectrum as presented on Fig.3.8 (amplified by a factor of 5), previously assigned to terminal oxygen [61], and the main peak centered at ~ 1010 K resulted from the film decomposition and thus attributed to lattice oxygen. The intensity of both peaks basically scaled with increasing the nominal film thickness. Therefore, combined together the LEED, STM, and TDS results suggest the increase of the reaction rate above 1 MLE, shown in Fig.3.6, due to the increasing the surface fraction covered by an oxidic (not necessarily the RuO_2) phase.
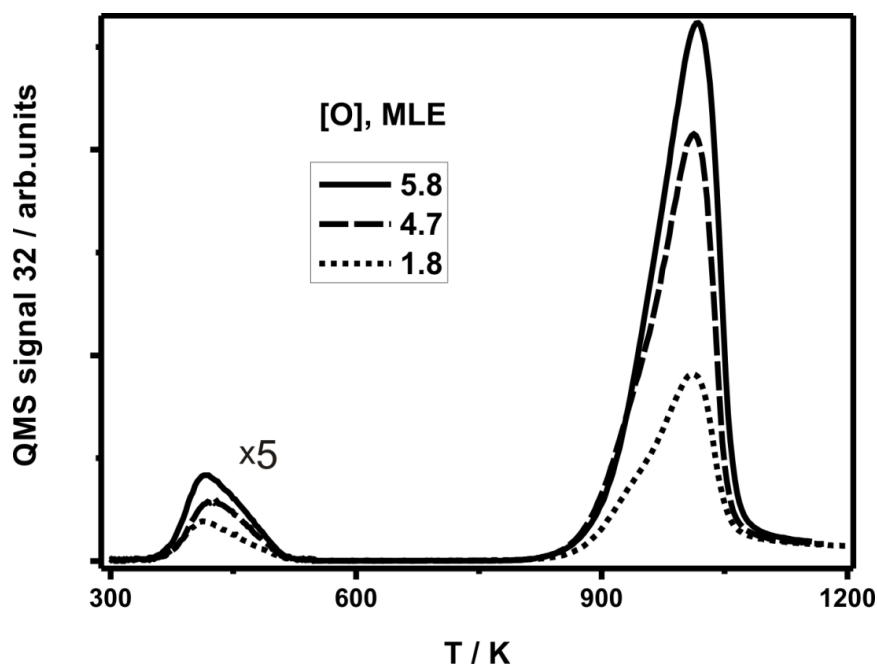

Figure 3.8 TPD spectra of oxygen from decomposition in UHV of oxygen pretreated oxide films RuO_x/Ru(0001) (10 mbar O_2 at 450 K, 20 min). Heating rate β=3 Ks^{-1}

48

3.3.3 Activation energy and reaction orders

The apparent activation energy of CO oxidation was measured under oxidizing conditions only for the 5 MLE samples, where the $RuO_2(110)$ film covered the whole surface. A freshly prepared film of the same composition was prepared for each experiment. Kinetic curves of CO_2 production at different temperatures are shown on Fig.3.9a. In the mixture of 10 mbar CO and 50 mbar O_2 the Arrhenius plot in the temperature range of 400 - 470 K yields the activation energy ca. 58±4 kJ/mol as shown on Fig. 3.9b.
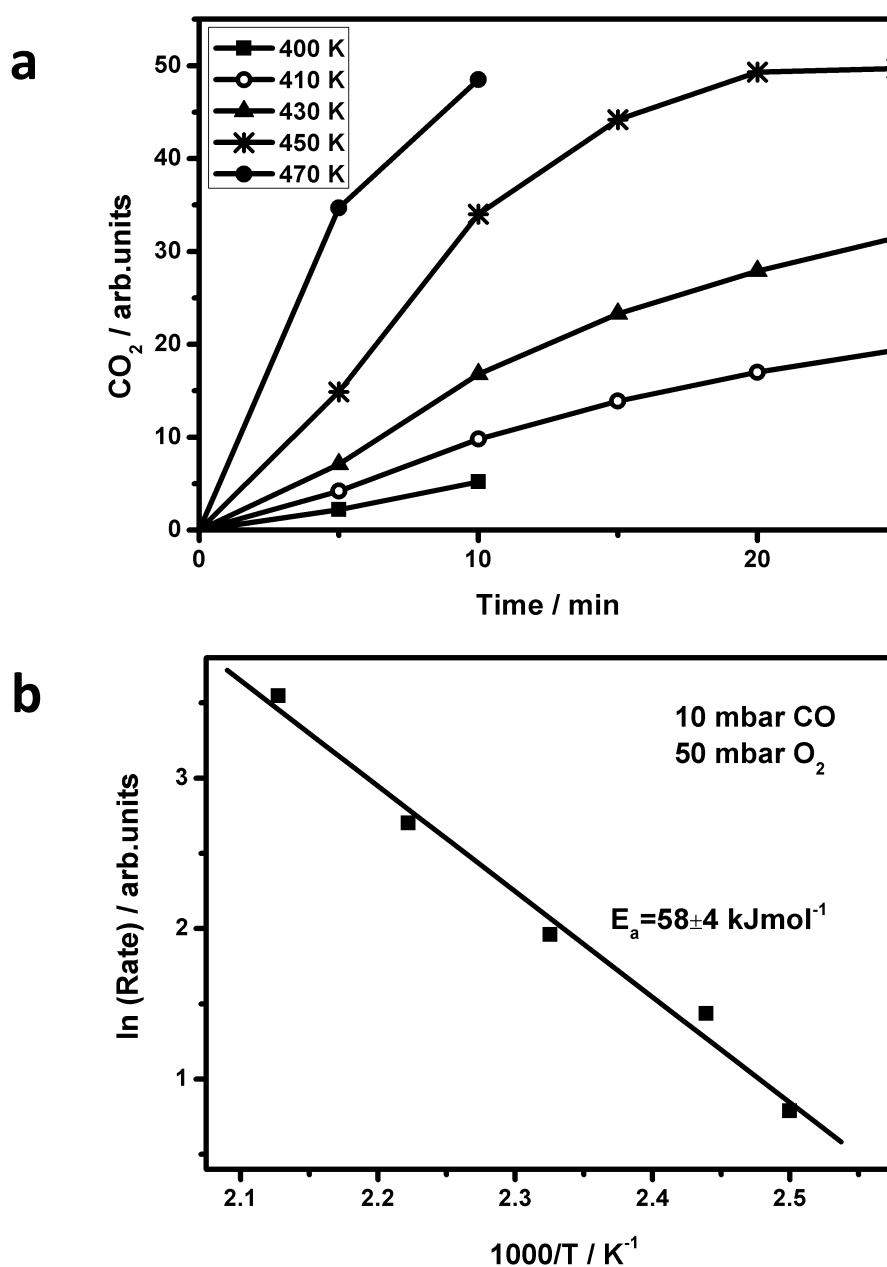
Figure 3.9 CO oxidation at different temperatures over 5 MLE oxide films on Ru(0001) in a mixture of 10 mbar CO and 50 mbar O_2 balanced to 1 bar with He: a - kinetic curves, b - the Arrhenius plot.

This value is considerably lower than 78±10 kJ/mol reported for the 1.6 nm RuO$_2$(110)/Ru(0001) film and measured at the nearly stoichiometric CO/O$_2$ ratios (14 mbar CO + 5.5 mbar O$_2$) at 470 - 670 K [103]. Since in the current work the reaction was carried out at low temperatures and excess of oxygen, no deviation from isothermal mode was observed in contrast to [104], where authors performed the direct comparison between the reactivity of non-oxidic phase and that of a RuO$_2$(110) layer 1.6 nm thick (250 mbar CO + 130 mbar O$_2$, > 550 K) and reported the ignition of the reaction over the oxidic phase causing temperature increase up to 130 K and a self-acceleration of the reaction.

The reaction orders n for CO and m for O$_2$ in the reaction rate equation (where r is reaction rate, k is reaction constant, θ_{CO} and θ_{O_2} surface coverages of CO and O$_2$ respectively)

$$r = k \cdot \theta_{CO}^{n} \cdot \theta_{O_2}^{m} \qquad (3.2)$$

were determined by measuring reactivity at different CO/O$_2$ ratios at 430 K. In one set of the experiments, the partial pressure of CO was set to 10 mbar, and the oxygen pressure was varied. In another set, the oxygen pressure was set to 20 mbar, and the CO pressure was varied. (Again, for each experiment, a new film with the same surface composition was prepared, 5 MLE thick). The results, shown in Fig.3.10, revealed the first order reaction for CO and practically zero order for O$_2$. Zero orders for both CO and O$_2$ were reported by Over et al. [103], which were, however, determined only qualitatively by varying partial pressures of both gases simultaneously.

The reaction kinetics, presented in Figs.3.10 (a,b), clearly shows the catalysts deactivation with time. Several mechanisms for the deactivation have been discussed in the literature: a surface reconstruction into a less active phase [105] and a carbonaceous (e.g., a carbonate) contamination [91, 101]. Which of these two is operative in experiments of current work is difficult to ascertain on the basis of solely AES and LEED characterizations of the post-reacted surfaces. The results of Fig.3.5 demonstrated no CO$_2$ self-poisoning effect otherwise expected for the carbonate mechanism. It therefore appears that the deactivation is a relatively slow process, at least under net oxidizing conditions (see Fig.3.4).

In the recent work of Gao et al. [91] authors demonstrated that under oxidizing conditions and relatively low temperatures (<450 K) preformed RuO$_2$ films display higher

activity than the (1×1)O-Ru(0001) phase, i.e. in full agreement with this work. However, the activity was determined from the pressure changes monitored with a baratron gauge using the entire UHV chamber (61.6 l) as the reactor. The reactant mixture was renewed each time when the conversion exceeded 10 %. But this high reactivity regime for RuO_2 is restricted: (1) to very oxidizing reaction conditions (2) to very low reaction temperatures, and (3) to short reaction times. Although these are the conditions used in the present work, its results indicate that the decisive parameter is the low reaction temperature, at which the (preformed) $RuO_2(110)$ films are more active than metallic Ru(0001) regardless of the $CO:O_2$ ratio and reaction time.
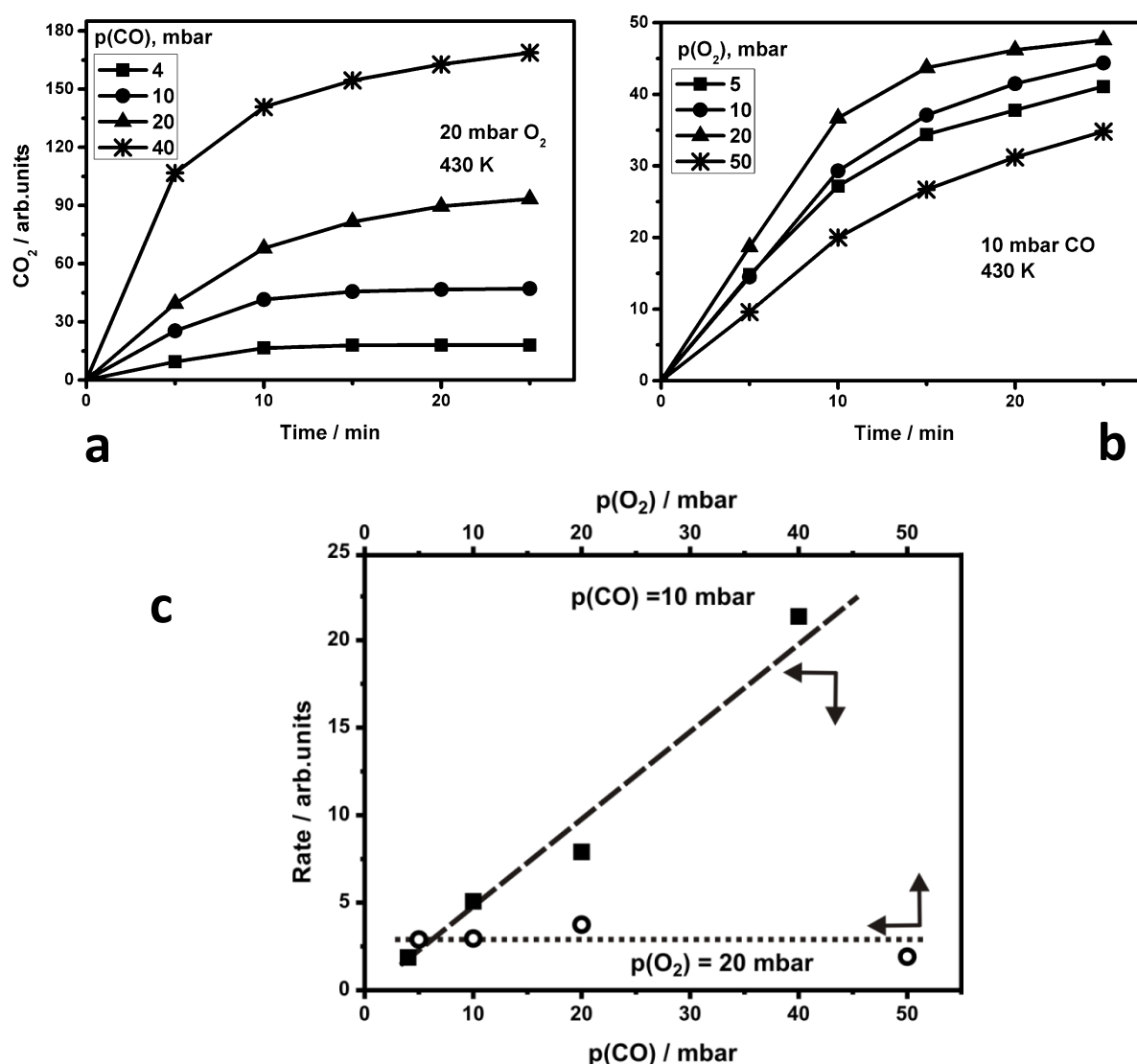
Figure 3.10 Pressure dependence of the CO oxidation reaction on 5 MLE RuO_x films on Ru(0001) at 430 K: a - the CO pressure was varied at fixed $p(O_2)$ = 20 mbar (He balance), b - the O_2 pressure was varied at fixed $p(CO)$= 10 mbar (He balance), c - reaction rates vs pressures. Each data point corresponds to a new film.

51

It seems the only discrepancy that remains between current work and Gao et al's study is their finding of a ''negative'' activation energy at T<475 K in the mixture of 8 Torr CO and 40 Torr O_2 (see Figs. 7a and 8 in [91]), that has never been reported for any technical or model Ru catalysts. Meanwhile, regular behavior is shown in the current work, with activation energy of 58±4 kJmol^{-1} (see Fig.3.9b). In order to explain the rate decreasing with the temperature in the range 400–475 K, Gao et al. invoked the formation of a carbonate which deactivates the active sites at low temperatures, but dissociates upon approaching 500 K. However, this explanation implies that the carbonate overlayer was formed before the reactivity was measured. In contrast, the experiments shown in Fig.3.5 suggest that the presence of CO_2 (as a precursor for a carbonate) does not change the reaction rate, at least on the most active films.

3.3.4 Surface order influence

Finally, in order to see the effect of surface ordering on the reaction, the reactivity of the disordered films was compared with that of ordered films. For this, freshly prepared oxide films were subjected to mild Ar$^+$-sputtering (500 eV) followed by re-oxidation in 10^{-4} mbar O_2 at 450 K, i.e., much below the temperature used for the preparation of ordered films (~ 700 K).

These treatments resulted in the disappearance of the characteristic diffraction spots of the RuO_2(110) phase, i.e. loss of its long-range order, and increased background intensity with Ru spots left on the LEED pattern as shown on Fig.3.11, although no considerable changes in the surface stoichiometry were observed by AES. Nonetheless, for the two thicknesses studied (4.5 and 6.5 MLE), the disordered films exhibited higher reaction rate than the ordered films (see Fig.3.12). Each kinetic curve refers to a new sample. Thermal decomposition confirmed the presence of O_2 peak at ~ 420 K in TPD spectrum similar to that observed for O-pretreated ordered RuO_x films on Fig.3.8.

Thus, the reactivity of oxide surface is not related to the surface ordering, thus suggesting that CO oxidation over the ruthenium oxide surfaces is, in fact, structure insensitive. Therefore, the rate enhancement, observed for the disordered films, could, in principle, be explained by the increased surface area of the roughened surfaces. These

results agree well with the previous high pressure (0.1 mbar, CO:O_2=1) XPS studies showing no direct correlation between the high CO_2 production rate and the formation of the stoichiometric RuO_2 phase [78].
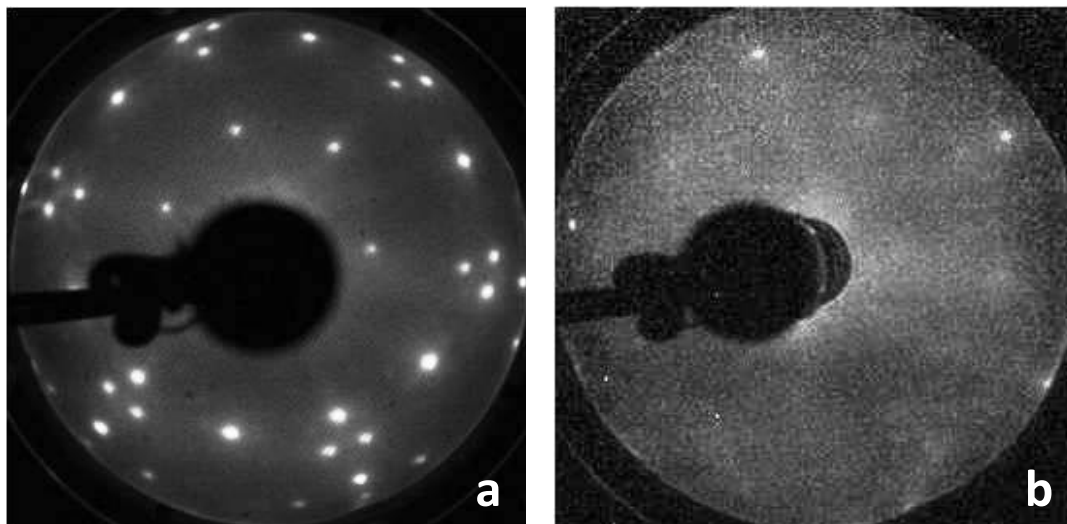

Figure 3.11 LEED patterns (70 eV) of (a) an ordered 5 MLE RuO_2(110)/Ru(0001) and (b) a disordered RuO_x film on Ru(0001) prepared from (a) by 500 eV Ar^+ sputtering at 300 K and re-oxidation in 10^{-4} mbar O_2 at 450 K.
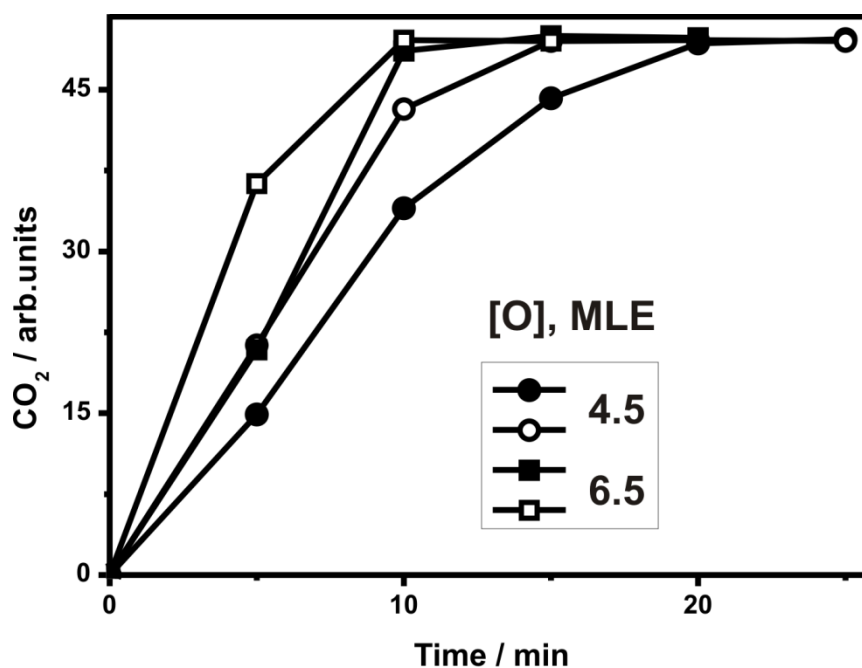

Figure 3.12 Effects of surface ordering on the reactivity of thin oxide films on Ru(0001). Solid and opened symbols show the results for ordered and disordered films, respectively, at two thicknesses as indicated. The disordered surfaces were prepared by 500 eV Ar^+ sputtering at 300 K and re-oxidation in 10^{-4} mbar O_2 at 450 K.

3.3.5 Comparative study of RuO$_x$ films on Pt(111) vs RuO$_x$/Ru(0001)

In order to see the effect of a metal substrate thin ruthenium oxide films were grown on Pt(111). Pt(111) and Ru(0001) planes have the similar geometry, and thus the correct epitaxial relationships for rutile-like RuO$_2$(110) plane are possible as shown on Fig.3.13 (similar to the sketch on Fig.3.2) as well as for (100) plane [106].
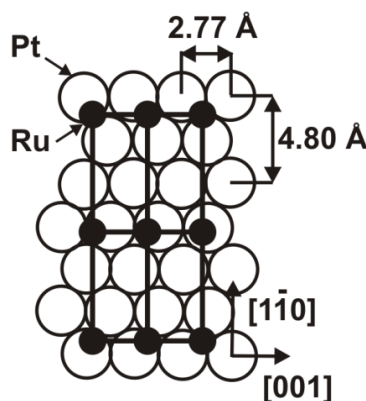
Figure 3.13 Epitaxial relationships of rutile RuO$_2$(110) phase on a hexagonal surface Pt(111) [106]

So far fabrication of *thin* ruthenium oxide films on Pt(111) under UHV conditions has never been reported. Mostly the available literature refers to electrochemical growth. In [107] the authors reviewed the preparation of Ru decorated Pt(111) electrodes by electrochemical and PVD deposition and its activity in CO electrooxidation attributed to a surface *metallic* alloy (with the initial submonolayer Ru coverage). There was briefly mentioned that the presence of oxide fraction inhibits the ruthenium deposition. Highly (110)-textured polycrystalline RuO$_2$ films 150-300 nm thick were grown on Pt(111)/Ti/SiO$_2$/Si(001) by metal-organic chemical vapor deposition (MOCVD) method [108]. 300 nm thick RuO$_2$(100)/ Pt(111) electrodes were prepared by reactive sputtering in oxygen for further use as a substrate [106].

In this work the preparation of thin RuO$_x$ films on Pt(111) was made in two steps. At first ruthenium was evaporated on Pt(111) at room temperature from a metallic rod by e-beam assisted reactive deposition in 10^{-7} mbar O$_2$. Subsequent postoxidation in 10^{-4} mbar O$_2$ was performed at 700 K, identically to the requirements for the growth of the native oxide film on Ru(0001). As prepared oxide films exhibited the (1×1) hexagonal LEED pattern with the slightly diffused spots and enhanced background intensity as shown on Fig.3.14b, i.e. completely different from expected RuO$_2$(110) phase grown on Ru(0001). Upon the film

preparation Pt spots should attenuate, however, lattice constants of Pt(111) and Ru(0001) are similar (2.71 and 2.77 Å respectively) that it is difficult to distinguish in this superimposed hexagonal array of spots with enhanced intensity between Ru and Pt. Thus, the theoretical calculation [106] of the epitaxial growth of a rectangular lattice over a hexagonal one did not come true in the actual experimental work.
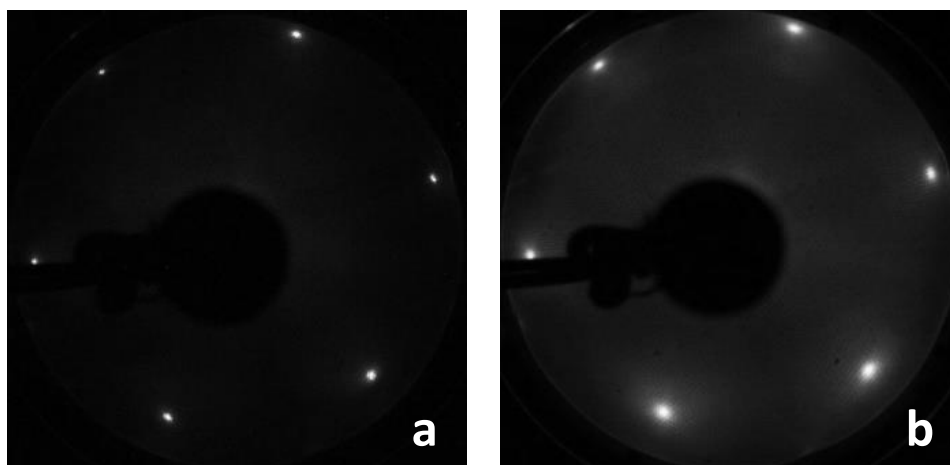

Figure 3.14 LEED patterns (70 eV) of RuO_x film on Pt(111): a- clean Pt(111), b - RuO_x film on Pt(111).

On deposited RuO_x films open patches of Pt(111) surface could be excluded, since *no* CO uptake typical for Pt(111) qualitatively (by the peak shape) and quantitatively (the peak position and height) was observed as depicted on Fig.3.15. Desorption of CO from ideal Pt(111) surface is characterized by well-known broad peak between 300-500 K with a pronounced shoulder at 360 K [109].
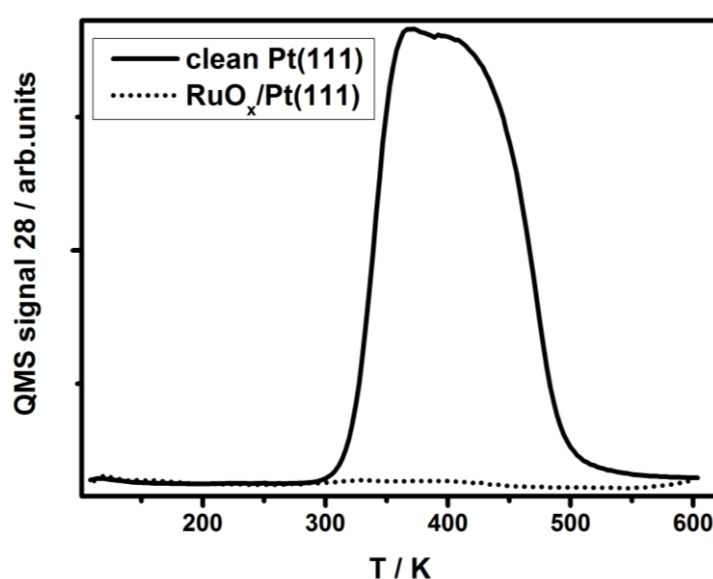
Figure 3.15 CO TPD profiles from clean Pt(111) and RuO_x film on Pt(111). Heating rate $\beta=3$ Ks^{-1}

The amount of oxygen on the surface clearly indicates the presence of some oxidic phase (measured both by AES and TPD). The Auger spectra of $RuO_x/Pt(111)$ and $RuO_x/Ru(0001)$ look very similar as shown on Fig.3.16.
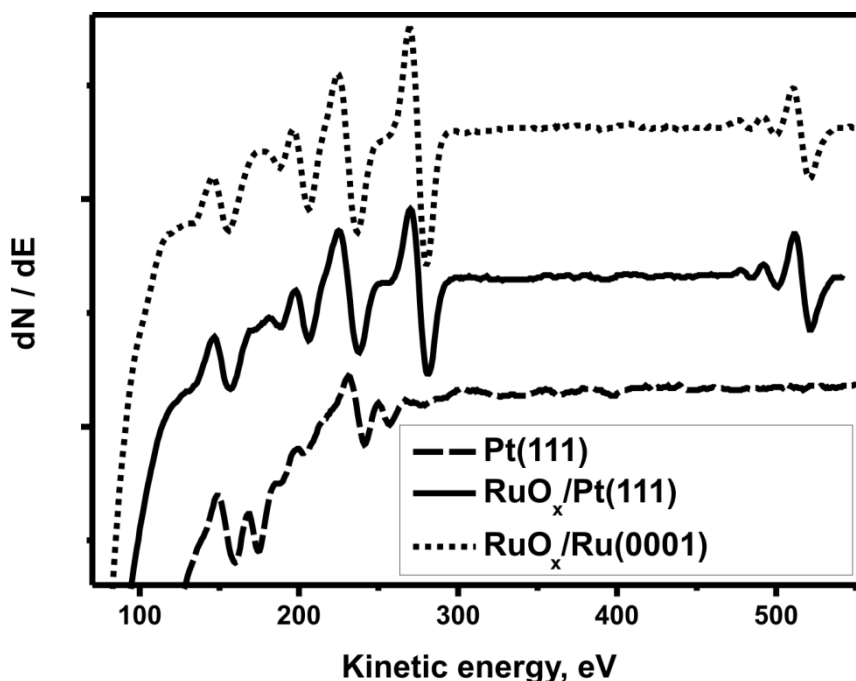

Figure 3.16 Auger spectra of RuO_x films of comparable thickness on Ru(0001) and Pt(111) (clean Pt(111) is given as well for the reference), 3 keV.

The reactivity measurements indeed demonstrated CO_2 formation over $RuO_x/Pt(111)$. The observed production rate was approximately twice less than that of $RuO_x/Ru(0001)$ under the same oxidizing conditions. This could be seen on Fig.3.17; it should be taken into account that the reactivity of the clean Pt substrate must be subtracted since the deposited film was grown on the one-side crystal. In analogy with a native oxide film a spent deposited film maintained its ordering and a compositional stoichiometry according to post characterization by LEED and AES.

The reason for such a low reactivity of $RuO_x/Pt(111)$ was studied in additional experiments with pure oxygen treatment. Similarly to the native oxide films on Ru(0001) freshly prepared and characterized RuO_x films on Pt(111) were subjected to 20 mbar O_2 at 450 K for 10 minutes in the HP cell. After this treatment they were thermally decomposed and *did not* exhibit any O-species in low temperature interval (below 750 K) as depicted on Fig.3.18 (compare with Fig.3.8 for native oxide films $RuO_x/Ru(0001)$). Note that O-species

56

desorbing at ~ 1150 K after the main lattice O-peak at 1000 K belong to 'as prepared' oxide film, i.e. not exposed to O_2 in the HP cell. However, some new feature appeared: before the lattice O-peak a broad moderate shoulder has developed at about 840-850 K. Its origin might be interesting from structural point of view as an evidence of the surface reorganization.
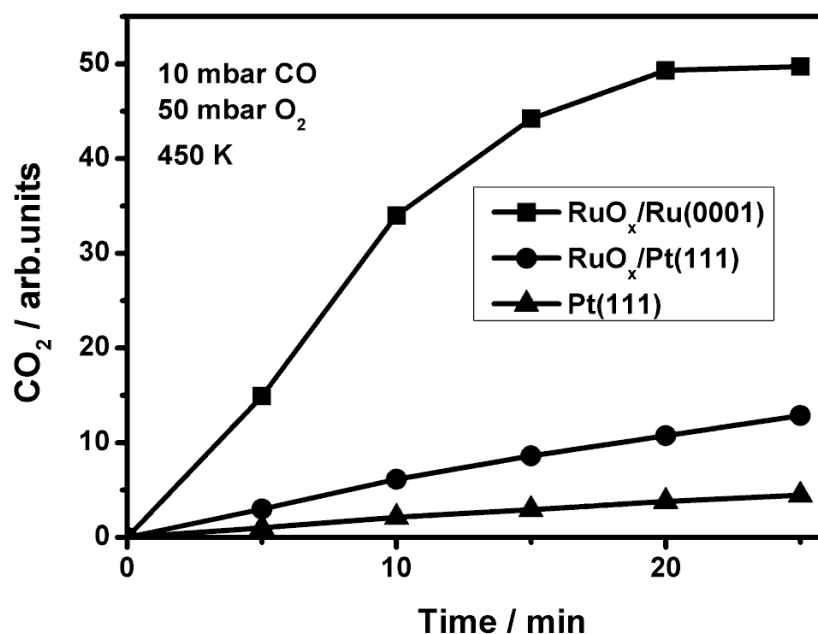

Figure 3.17 Kinetics of CO oxidation over RuO_x films grown on a one-side Pt(111) crystal and a double-side Ru(0001) crystal. The reactivity of a clean one-side Pt(111) crystal is given for the reference. Thickness of both oxide films is comparable.
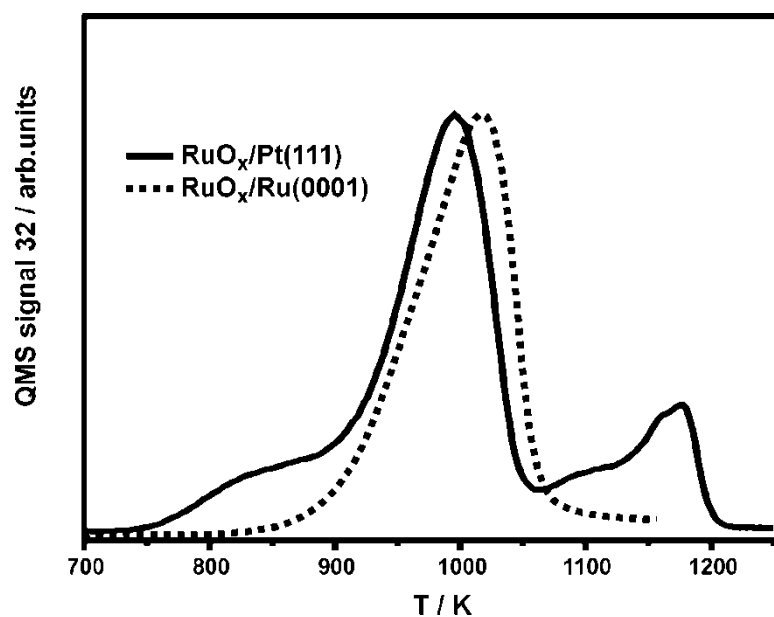
Figure 3.18 TPD spectra of oxygen from decomposition in UHV of oxygen pretreated RuO_x/Pt(111) compared with RuO_x/Ru(0001) (10 mbar O_2 at 450 K, 20 min). Heating rate β=3 Ks^{-1}

57

Observed results require additional morphological studies for the further clarification. This finding apparently contradicts to previous, when presputtered native films of ill-defined structure on Ru(0001) showed a pronounced enhancement of CO_2 formation with a following conclusion about the reaction to be structure insensitive.

Formation of an oxidic phase is not a prerequisite of high reactivity itself. However, comparison of O_2 TPD spectra shows that important is the desorption temperature of oxygen species: similar to structure-reactivity dependence observed over FeO/Pt(111) [14-15]. Indeed, good correlation between the increase of the film reactivity and the absolute amount of weakly bound oxygen (WBO) as a function of film thickness allows to conclude about higher availability of O atoms in RuO_2(110) phase (growing preferentially on Ru(0001)) either upon film thickening and/or better ordering. Fig.3.19 represents data taken from Figs.3.6 and 3.8 to make the statement more obvious: here a WBO-axis shows an integral area under the low temperature O-peak (at 420 K) formed at elevated O_2 pressures (Fig.3.8). And since this peak develops only on oxide phase of (110) orientation due to its geometry, oxide film thickness (and coverage) is not critical for the superior catalytic activity of ruthenium oxide in the CO oxidation reaction.
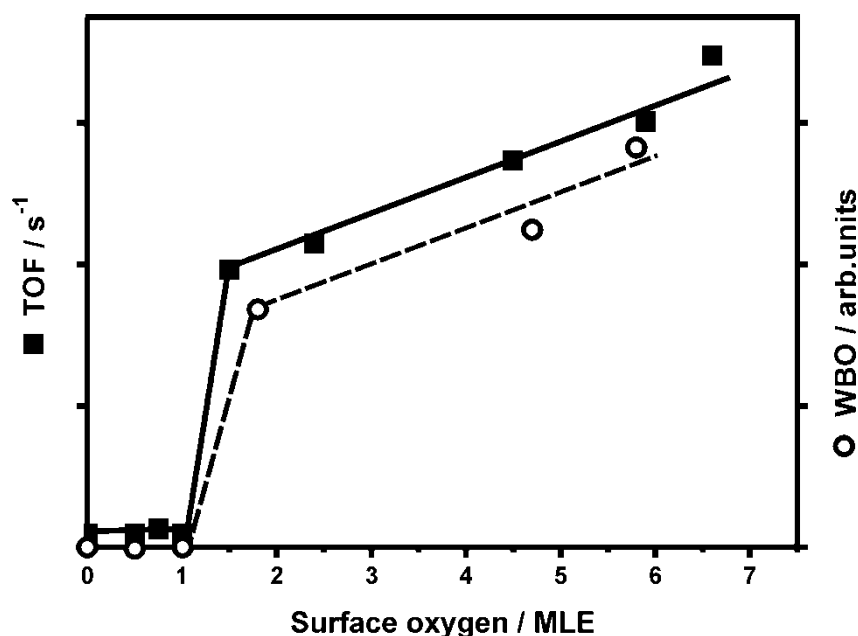

Figure 3.19 Consistency between increase of the film reactivity and the absolute amount of weakly bound oxygen (WBO) as a function of film thickness. The plots are offset from each other for clarity.

3.4 Summary

- Thin ruthenium oxide films grown on Ru(0001) and O/Ru(0001) overlayers were studied in the CO oxidation reaction at near-atmospheric pressures at low temperatures (400 – 470 K).

- It was shown that the reaction sets in only in the presence of the oxidic layer.

- For the ultra-thin films (1-2 MLE), the surface exposed both the oxide and O/Ru adsorbates structures. In addition, one-dimensional oxide structures were observed, which were tentatively assigned to the intermediate state for a crystalline oxide thin film that covers the whole surface at higher oxygen coverage.

- The films apparently maintained the structure and composition under highly oxidizing reaction conditions.

- The reaction rate slightly increases with increasing the nominal film thickness and correlates with the total amount of weakly bound oxygen species formed on the surface.

- The disordered native oxide films on Ru(0001) showed even higher reactivity than ordered counterparts. Therefore, it was proposed that surface ordering of oxide phase does not play a key role in CO_2 formation.

- However, deposited RuO_x films on Pt(111) possessing no (110) ordering and weakly bound O-species have demonstrated much less reactivity towards CO oxidation than RuO_x films on Ru(0001) of comparable thickness under the same oxidizing conditions.

- Thus, obtained results suggest that the epitaxial growth of RuO_2(110) phase is a prerequisite for the Ru-based catalyst to be active and defines the reaction mechanism. Possibly, the disordered RuO_x films on Ru(0001) still maintained some islands or domains of the active RuO_2(110) phase, but they were too small to be detected by LEED.

Chapter 4

CO oxidation over zinc oxide films on Pt(111)

4.1 Catalytic activity of ZnO-based materials and growth of ZnO films

Besides large-scale use of ZnO as a semiconductor, colorant and technological filler, zinc oxide is widely represented in heterogeneous catalysis due to industrial application in methanol synthesis and water gas shift reaction (WGSR) [110, 111].

Preparation and characterization of polycrystalline powdered $Cu/ZnO/Al_2O_3$ mixtures and their reactivity measurements under technologically relevant conditions are in very detail described in works of R. Schlögl's and M. Muhler's groups [112, 113]. There the authors came to the conclusion about the active involvement of metal-oxide interface in the reaction mechanism when Cu particles distributed over an oxide support under reaction conditions are partially covered with ZnO_x species as a result of the SMSI effect.

The growth, electronic properties, interaction with a number of adsorbates and the reactivity of Cu nanoparticles deposited on O-terminated ZnO(0001) (Zn- as well) single crystals are reviewed in papers of C.T. Campbell with coworkers, e.g. [114] with references herein. In parallel they studied the kinetics of forward and reverse WGSR on clean Cu(111) and (110) to model high-area Cu/ZnO catalysts [115]. An attempt to grow an 'inverted' $ZnO_x/Cu(111)$ model catalyst and employ it in methanol synthesis did not yield any product formation, most likely because of the reaction conditions far from realistic [116].

Upon Zn-coverage dependent studies of CO_2 hydrogenation over Zn-deposited low-index Cu surfaces Nakamura et al. [117] concluded about structure sensitive Zn promotional effect: in contrast to Zn/Cu(110) and Zn/Cu(100) systems Zn/Cu(111) showed high turnover frequencies of methanol formation (18 atm, 523 K) at low Zn coverage (<0.2) due to Cu-Zn surface alloy. At higher coverages (>0.2) Zn is selectively oxidized to ZnO leading to a drastic

decrease of the catalytic activity. In comparison with Cu(111) and other Cu planes the activity of Zn/(111) was close to that of Cu/ZnO powder catalyst [118].

Involvement of metal-oxide interface in the reaction mechanism mentioned above allows studying a model reaction, e.g. CO oxidation over a thin ZnO film grown on any suitable (111) metal substrate as a good starting point.

Growth of the well-ordered ZnO films was previously reported using Ag(111) and Pd(111) single crystal substrates. With the help of surface x-ray diffraction and scanning tunneling microscopy (STM), Tusche et al. [119] observed that 2 ML-thick ZnO(0001) films grown on Ag(111) are depolarized, i.e. Zn and O atoms are arranged in co-planar sheets like in the hexagonal boron nitride (or graphite) structure. The transition to the bulk wurtzite structure occurs in the 3–4 ML coverage range and is accompanied by considerable surface roughening.

On Pd(111), Weirum et al. [120] observed the layer-by-layer growth mode for ZnO films up to 5 ML, at least. Low energy electron diffraction (LEED) and STM results together with density functional theory calculations suggested that the graphite-like structure is thermodynamically the most stable phase over a large range of oxygen chemical potentials, before it converges to the bulk-type wurtzite structure at a film thickness above 4 ML.

Small molecules can adsorb on individual clean ZnO phases depending on the surface termination and polarity. This was intensively investigated by Wöll with coworkers and is explicitly reviewed in [121]. Here they conclude referring to their own work [122] that electrostatically unstable polar O-terminated ZnO phase is the most interesting from the chemical point of view since it was theoretically predicted to be active in methanol synthesis from syn-gas.

Although ZnO-based catalysts are primarily used in the methanol synthesis and the water gas shift reaction, CO oxidation was previously studied as well on ZnO powders, single crystals and films. In the work of Kobayashi with coworkers [123] with commercial ZnO powder in addition to the Langmuir-Hinshelwood mechanism, i.e. between chemisorbed CO and oxygen, and Eley-Rideal mechanism, with reaction between gaseous CO and adsorbed

oxygen, the simultaneous two reaction pathways mechanism was considered, in which two different active species (neutral O and O⁻) were involved.

Esser with colleagues [124] reviewed earlier reports on the reactivity of polycrystalline ZnO surfaces in CO oxidation and compared with that of ZnO(10-10) in own experiments: they concluded that the results on polycrystalline samples are determined by contributions from nonpolar ZnO(10-10) patches and that elementary steps of the reaction can be explained on the basis of charge transfer.

Weiss and Folman [125] studied CO oxidation over ZnO films, fabricated by r.f. sputtering on Ag foil, as a function of the film thickness. However, the thinnest films studied were about 20 nm in thickness. Nonetheless, the authors found that the elementary constants in the rate equations for CO oxidation at 600-650 K depend on the film thickness. Good agreement between the experimental and the theoretical results, based on the Schottky model together with the rigid band model, has been found.

Therefore, keeping in mind all the information above, here I have studied the reactivity of ZnO films on Pt(111) in the CO oxidation reaction at low temperatures and near atmospheric pressures in the continuation of previous works of our group on CO oxidation over ultrathin oxide films.

To the best of my knowledge, the only available information about purposeful growth of crystalline ZnO layers on Pt substrate refers to works about ZnO/Pt electrodes, e.g. of Chugh with coworkers [126], where they reported the fabrication of ZnO/Pt(111)/sapphire(0001) by PLD (pulsed layer deposition) and provided a HRTEM (high resolution transmission electron microscopy) image of such a layered structure as well as XRD (x-ray diffraction) proof of preferential formation of ZnO(0001).

Guided by 'the electronic theory of catalysis' and the concept of weakly-bond oxygen both for FeO/Pt(111) and RuO$_x$/Ru(0001) in this project I was driven by the idea of establishing the relationship between the reactivity of ZnO films and their thickness.

4.2 Structure of materials and thin film preparation

Bulk ZnO can exist in the form of three polymorphs: zinc blend (sphalerite), wurtzite and rock salt. Zn^{2+} and O^{2-} ions are tetrahedrally coordinated to their counter ions in the first two forms, while in the latter, which is stabilized at higher pressure, the local environment is octahedral. The most thoroughly studied and thermodynamically stable under ambient conditions phase is the wurtzite one. Polar (0001) or (000-1) as well as non polar (10-10) and (11-20) planar surfaces can be prepared. Polarity of certain ZnO planes originates from the ionic nature of Zn-O bond and, thus, an existing dipole moment and generated electric field.

Along the c-axis of the polar (0001) or (000-1) directions, ZnO exhibits repeating Zn/O/... stacks of the hexagonal type. When the ZnO bulk is truncated normal to these planes, the surface is Zn- or O-terminated, respectively, with three-fold coordinated atoms (see Fig.4.1a). Such surface is electronically unstable, and surface charge is usually compensated through surface reconstruction, facetting, electron redistribution or most likely adsorption of foreign species from the residual atmosphere in the experimental set-up, e.g. hydroxyls, yielding a lower surface energy. Stabilized ZnO(0001) and (000-1) basal faces have a unit cell with a=3.25 Å in the real space giving a hexagonal (1×1) LEED pattern [96, 121, 127]. In contrast to ZnO single crystals with wurtzite structure ultrathin ZnO films grown on Ag(111) [11] demonstrated planar graphene-like structure (Fig.4.1b).
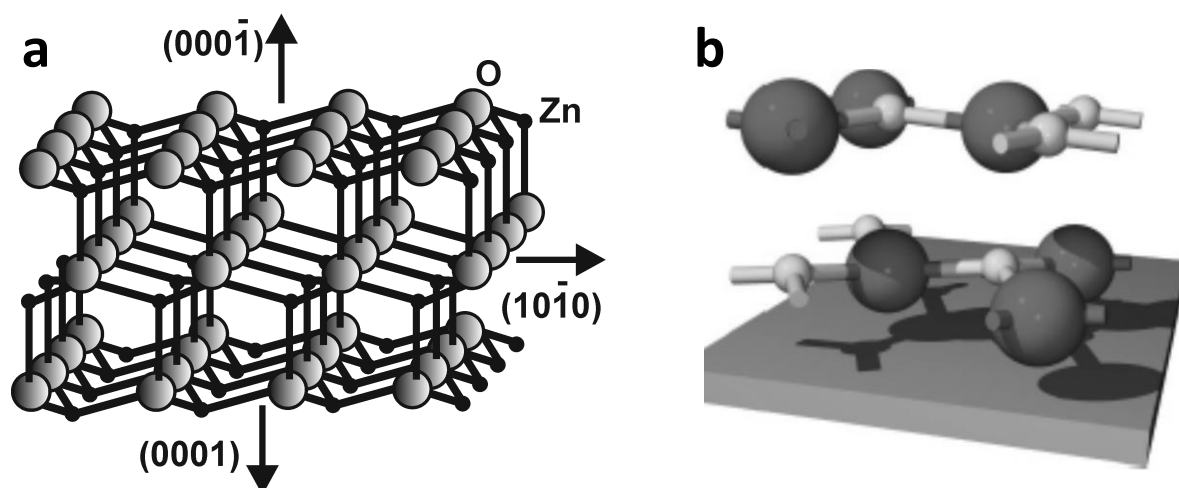
Figure 4.1 Structures of ZnO bulk material and thin film: a - Stick-and-ball model of bulk ZnO of wurtzite structure [96], b - graphene-like planar structure of 2 ML ZnO(0001) film on Ag(111): small and large balls refer to Zn and O respectively [119].

Extended STM studies of geometric and electronic properties of low-index ZnO surfaces of single crystals done by Diebold's group [128, 129] revealed an essential difference between the surface morphology of (0001)-Zn and (000-1)-O phases. The Zn-terminated surfaces are characterized by a high roughness on the nanoscopic scale exhibiting triangular islands and pits while oxygen-terminated surface presents flat hexagonal terraces, wide and smooth with no added islands and holes.

Zinc was deposited on a double-side Pt(111) crystal by heating a Zn rod (1 mm in diameter, 99.99%, Goodfellow) to ~ 500-520 K using W wire wrapped around. The Zn source is shielded by a stainless steel cylinder having a small orifice (~ 5 mm in diameter) and placed ca. 2 cm away from a crystal. The deposition flux was controlled via a Type K thermocouple spot-welded to the edge of the Zn rod. The construction and the deposition recipe were adapted from that of ZnO/Ag(111) of our group.

The zinc oxide films were prepared by Zn reactive deposition onto clean Pt(111) at 85 K or room temperature in 10^{-7} mbar O_2 followed by oxidation at 600 K in 10^{-6} - 10^{-5} mbar O_2 for 20 min. Low temperature Zn deposition favored more homogeneous Zn distribution over Pt surface (to get a closed film in one step) and almost full Zn oxidation close to ZnO stoichiometry prior to postoxidation.

Zn deposition in O_2 ambient was carried out to prevent Zn dissolution in the Pt substrate and any Zn-Pt alloy formation [130]. For most reactivity studies, oxide films were grown on either side of the crystal. Such a method of Zn deposition from a metallic source in an effusion cell further gives the oxide films of better quality in contrast to e-beam assisted deposition from self-made stoichiometric ZnO target.

Postoxidation was necessary only for the film ordering, since required amount of oxygen was already incorporated during the deposition step. Postoxidation temperature was found experimentally to have an oxide film well-ordered and intact (see Figs.4.2 and 4.3). The surface coverage was measured by CO titration of Pt sites (using TPD of CO that desorbs from Pt(111) at 300 – 500 K) and AES and expressed in monolayers (ML) or monolayers equivalent (MLE) (see below).
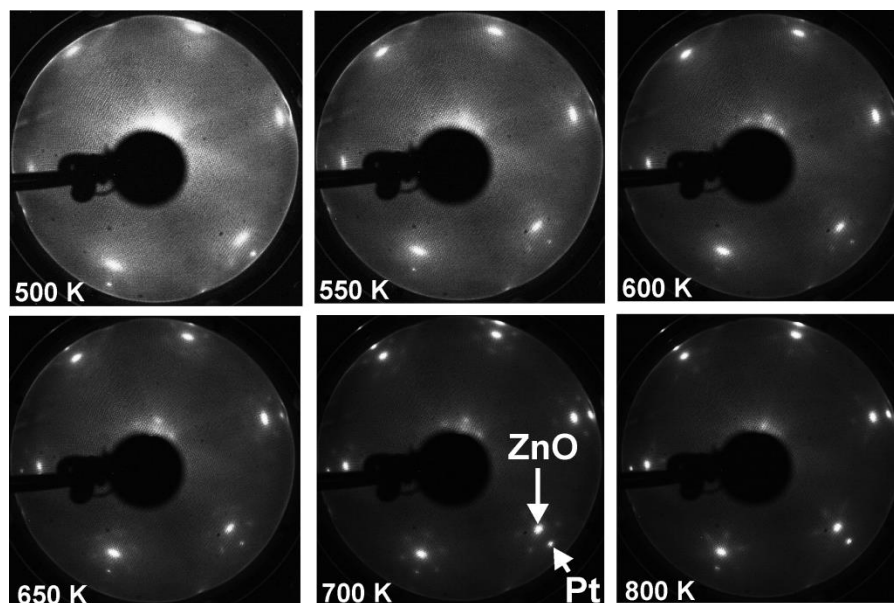
Figure 4.2 LEED patterns (at 60 eV) of ~1 MLE ZnO film on Pt(111), annealed in O_2 at different temperatures as indicated.
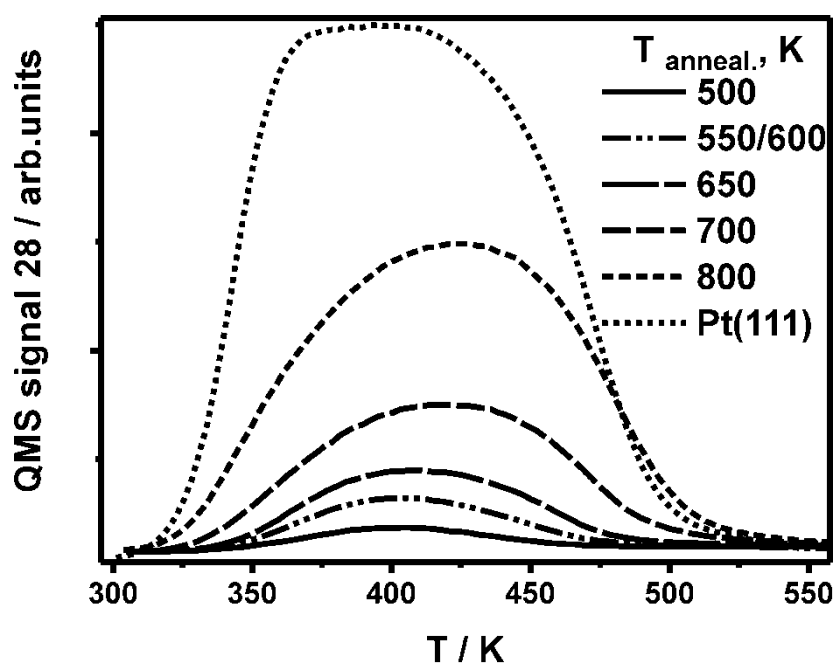

Figure 4.3 CO TPD profiles from clean Pt(111) and ZnO films on Pt(111) annealed at different temperatures in O_2 . Heating rate $\beta=3$ Ks^{-1}

Figs.4.4 and 4.5 show LEED patterns and Auger spectra of the "as-prepared" films at increasing thickness used for catalytic studies in CO oxidation. The diffraction spots of ZnO(0001)-(1×1) are aligned with those of Pt(111) and show up together with the surrounding hexagonal spots. The latter can be straightforwardly assigned to a coincidence

Pt(111)-(6×6) superstructure, similar to that observed on ZnO/Pd(111) [11], that arises due to the mismatch between the lattice constants of ZnO(0001) and Pt(111) (3.25 and 2.78 Å, respectively). Basically, 6 times the Pt(111) lattice coincide with 5 times the ZnO(0001) lattice. Such geometrical superposition was already given in [131]. Above 2-3 ML, the films only show a relatively diffuse pattern of ZnO(0001) with a high background intensity. The ZnO-related spots were sometimes streaky in the "tangential" direction, thus indicating the presence of domains slightly misaligned with respect to the metal support underneath.
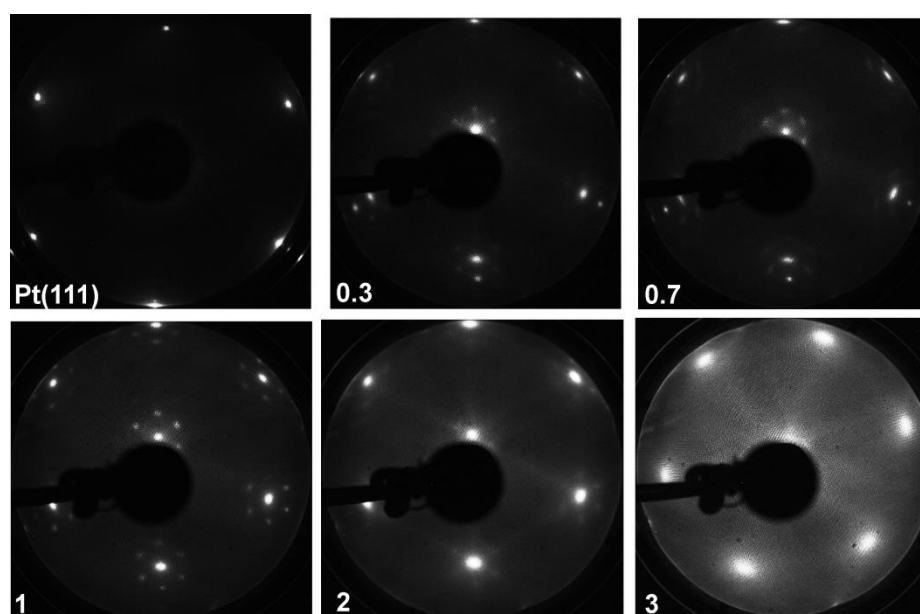
Figure 4.4 LEED patterns (at 60 eV) of ZnO films grown on Pt(111) at the different film thickness in MLE as indicated.
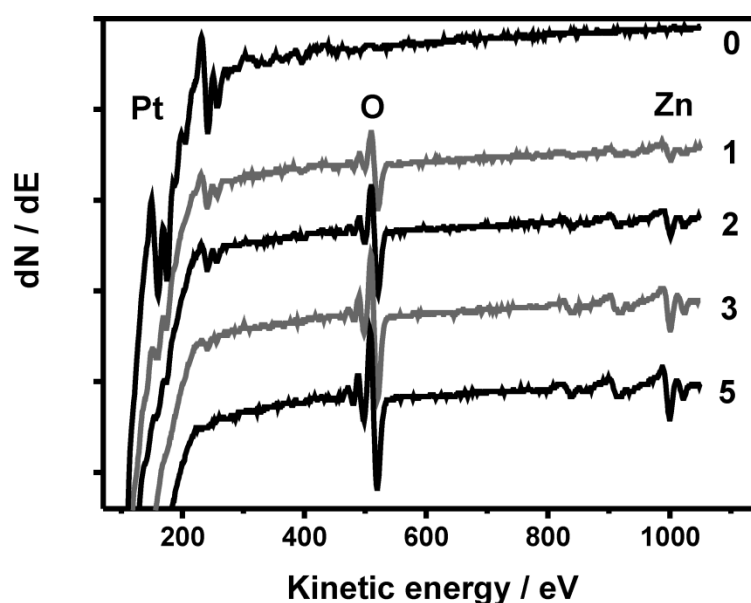
Figure 4.5 Auger spectra of ZnO films grown on Pt(111) at the different film thickness as indicated in MLE.

In submonolayer regime the surface coverage was measured by CO titration (see Fig.4.6a). For more than a monolayer coverage, the nominal thickness was measured by integrating the 32 amu (O_2) desorption signal during film decomposition at T > 950 K (see Fig.4.6b). Also the thickness was roughly monitored by AES via attenuation of the Pt related signals with two restrictions: at submonolayer coverage sensitivity to Zn is too low for precise estimation, at high coverage Zn and O signals stay constant with Pt signals almost gone (see Fig.4.7).
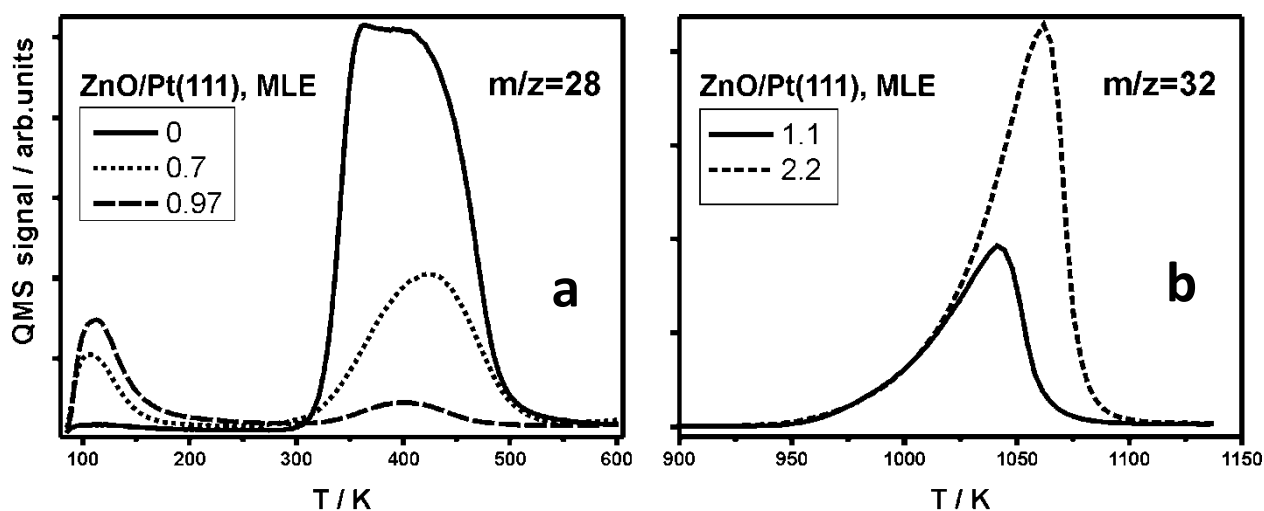
Figure 4.6 ZnO/Pt(111) coverage calibration: a - CO TPD profiles from clean Pt(111) and ZnO films on Pt(111), b - TPD spectra of molecular oxygen from decomposition in UHV of 'as prepared' ZnO films. Heating rate β=3 Ks^{-1}
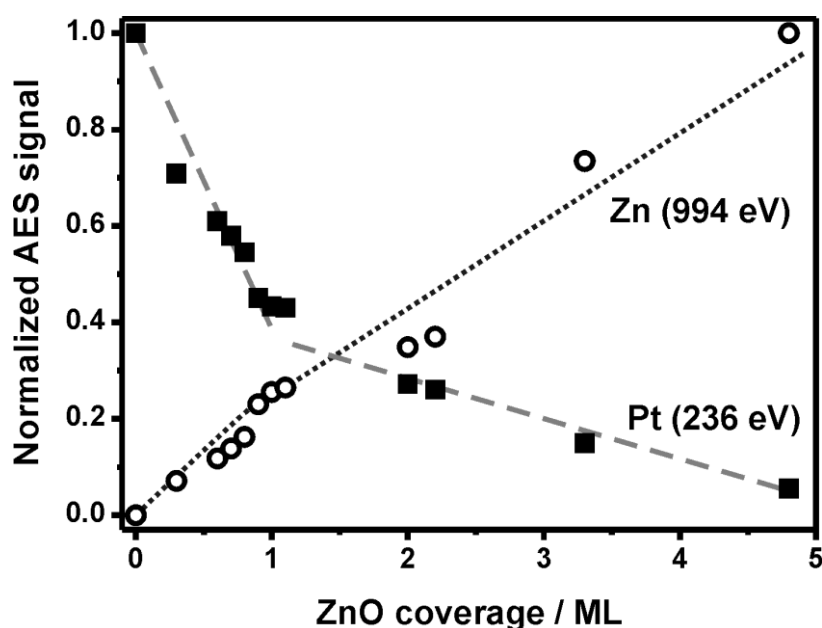
Figure 4.7 Auger signals of Pt and Zn as a function of the film thickness (in MLE). Characteristic breaking point at ~ 1ML reflects layer-by-layer growth mode of ZnO films on Pt(111).

To address the morphology of the ZnO films *additional structural characterization* of the similarly prepared oxide surfaces was performed in another UHV chamber equipped with LEED/AES and high pressure *scanning tunneling microscopy (HP-STM)* by *B.-H. Liu and M.E. McBriarty*, members of the 'Structure and reactivity' group, Department of Chemical Physics, Fritz-Haber-Institute of Max Planck Society.

At sub-monolayer coverages, Pt(111) terraces were randomly covered by two-dimensional islands (Fig. 4.8) [132]. The height measurements revealed that the islands are predominantly of ~ 2 Å in apparent height, although few islands of ~ 4 Å in height were also observed. These values correspond to one and two layers of graphite-like ZnO, respectively. Henceforth, the amount of Zn to form a dense monolayer film will be referred to as one monolayer equivalent (MLE).

Both mono- and bi-layer islands showed superstructure with a ~17 Å periodicity, which is consistent with the Pt(111)-(6×6) superstructure observed by LEED. The films thicker than 3 MLE showed no (6×6) superstructure in STM (also vanished in LEED), but triangular pits and islands which are very similar to those observed on ZnO(0001) single crystal surfaces in studies of Diebold's group [128].
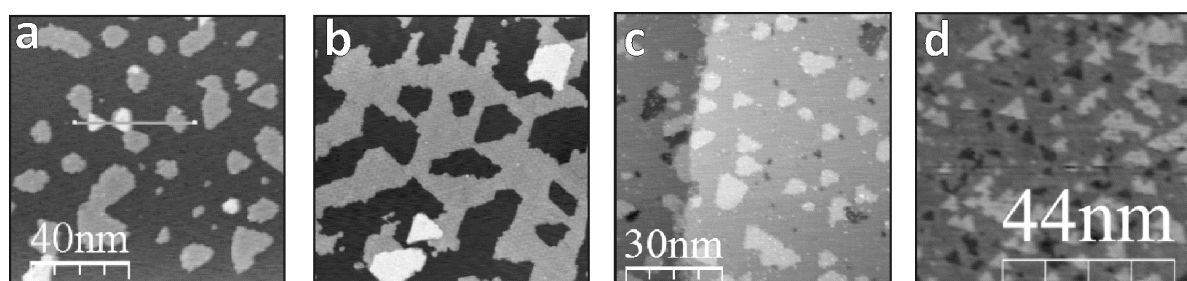
Figure 4.8 STM images of the "as prepared" ZnO films on Pt(111): 0.25 (a), 0.55 (b), 1.2 (c) and 4 MLE (d) [132]. The images are provided by *B.-H. Liu and M.E. McBriarty.*

Therefore, combined together the LEED, AES, STM and TPD characterization shows that the "as prepared" films first form ZnO(0001) monolayer islands which coalesce until the film covers the entire metal surface. The films then grow in a layer-by-layer mode. Upon increasing the thickness above 4 MLE, the film surface is essentially the same as of a ZnO(0001) single crystal, although the surface termination is not yet identified.

4.3 Results and discussion

4.3.1 Thickness dependence

The ZnO films, characterized by LEED, AES and CO TPD, were examined in the CO oxidation reaction at near atmospheric pressures at 450 K. The reactivity measurements were performed in excess of oxygen (CO/O_2 = 1/5) in order to prevent any possible oxide reduction and film dewetting, and also to compare with the previously studied FeO/Pt(111) films, which exhibited film dewetting under oxygen-lean conditions [14], and RuO_x/Ru(0001) films.

Fig.4.9a displays typical reaction kinetics observed for the ZnO films showing no deactivation in time. Fig.4.9b shows a CO_2 production rate as a function of the nominal film thickness measured *prior to* the reaction (overlapped reproduced data are not shown).

It is therefore clear, that the reaction exhibits a strong rate enhancement at sub-monolayer coverage. Interestingly, the 1 MLE film shows some activity, at least, it is higher than on pure Pt(111). As the thickness further increases, the rate gradually decreases such that the multilayer, "thick" ZnO films become almost inert under the conditions studied. The obtained trend is correct for ZnO films regardless the Pt(111) substrate temperature during the deposition of Zn (85 K or room temperature ~ 300 K).

AES characterization of the spent catalysts did not reveal considerable changes in the film stoichiometry, although some of the samples were lightly contaminated with carbon, in particular at the sub-monolayer coverages.

LEED patterns showed diffuse (1×1) spots of Pt(111) and ZnO(0001), whereas the (6×6) superstructure spots were vanished (see Fig. 4.10). Subsequent TPD measurements showed a considerably higher CO uptake (during the first run after reaction is about twice higher than before) as compared to that of measured prior to the reaction, thus indicating the film dewetting and concomitant Pt surface opening under the reaction conditions (see Fig.4.11).
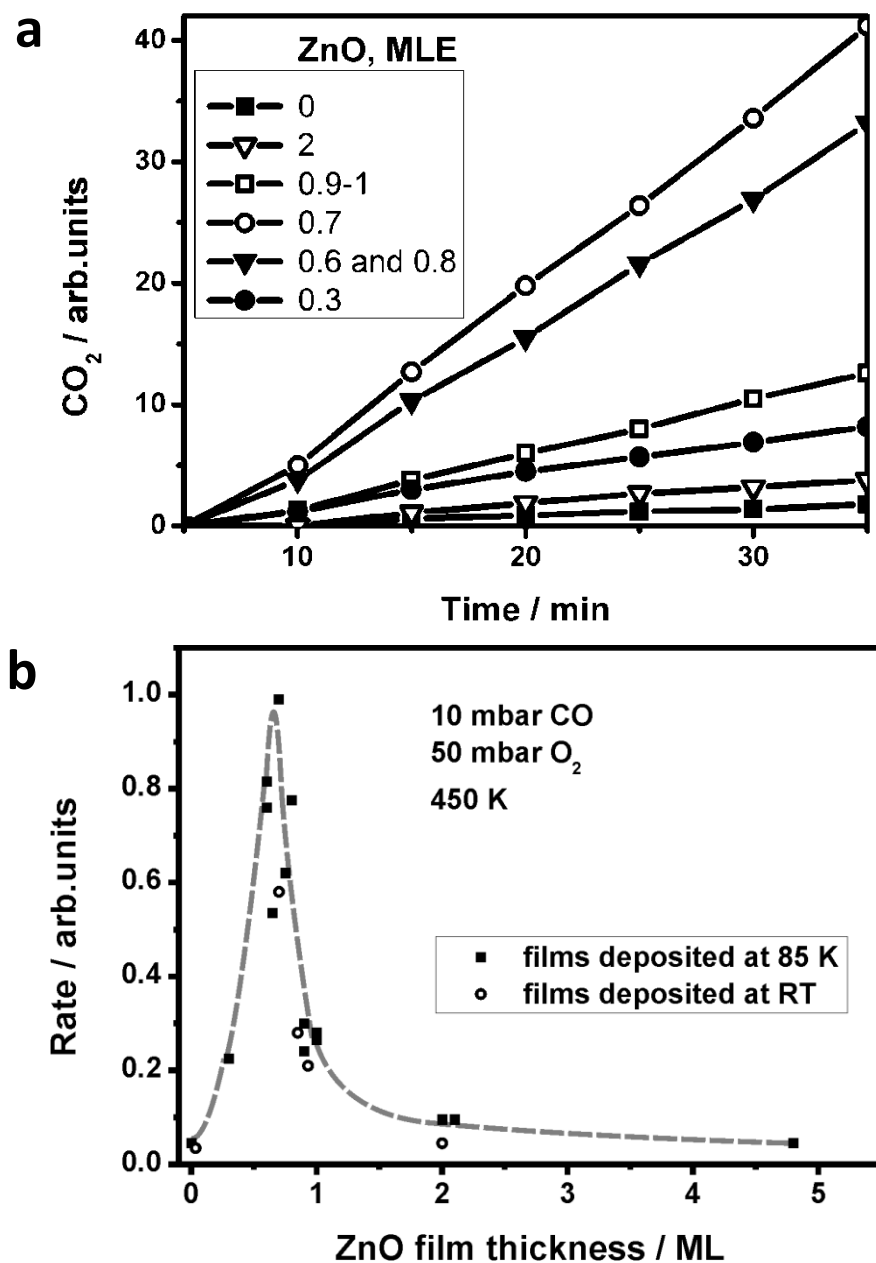
Figure 4.9 CO oxidation over ZnO/Pt(111): a - Kinetic curves for the pure Pt(111) and ZnO(0001) films. Reaction conditions: 10 mbar CO + 50 mbar O_2, He balance to 1 bar; 450 K, heating rate 1 Ks^{-1} (to reach 450 K). b - CO_2 production rate as a function of the nominal film thickness (in MLE).

Broadened and shifted to lower temperatures CO TPD profiles from postreacted films during sequential TPD runs after the first one are very similar to that reported for bimetallic surfaces of Zn/Pt(111) [130]. This could be ascribed to ZnO-Pt(111) alloying when heating the spent sample from 85 K to 600 K in UHV: upon burning some carbonaceous deposits formed under reaction conditions consume oxygen from the oxide film.
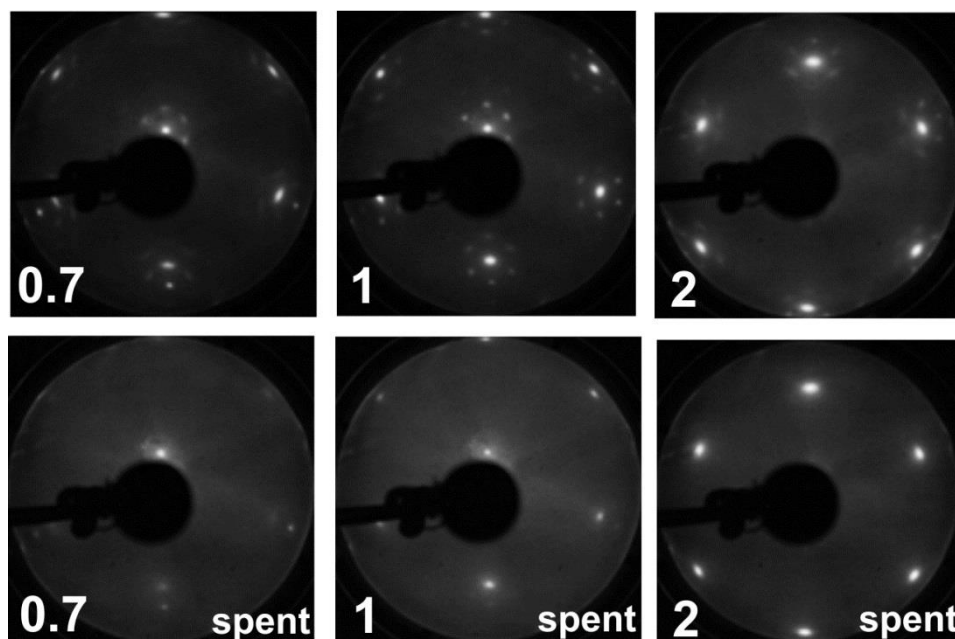
Figure 4.10 LEED patterns (60 eV) of the ZnO films on Pt(111) before (upper panel) and after (down panel) the reaction. The film thickness increases from left to right: 0.7, 1 and 2 MLE.
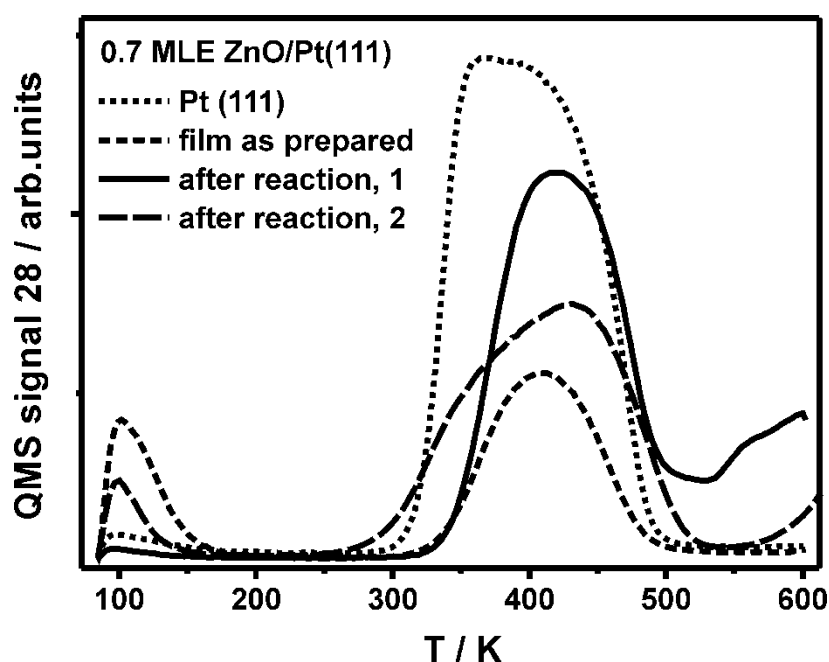
Figure 4.11 CO TPD for as prepared and post reacted surface of a ZnO film, θ=0.7. Heating rate β=3 Ks^{-1}

To examine whether the reaction is accompanied by Zn-Pt alloy formation, we studied the Zn-Pt alloy. For this, ~ 1 ML of Zn was deposited on clean Pt(111) surface with consequent annealing in UHV up to 600 K which resulted in the ordered (2×2) surface structure (see Fig.4.12). As prepared sample demonstrated well-documented CO TPD profile [130]. Explanation of such a well-pronounced shift of CO desorption peak from a freshly

71

prepared Zn-Pt(111) alloyed surface was given in [130]: the electronic perturbations induced by Zn on Pt reduce its CO-chemisorption ability by weakening the strength of the Pt(5d)–CO(2π*) bonding interactions.
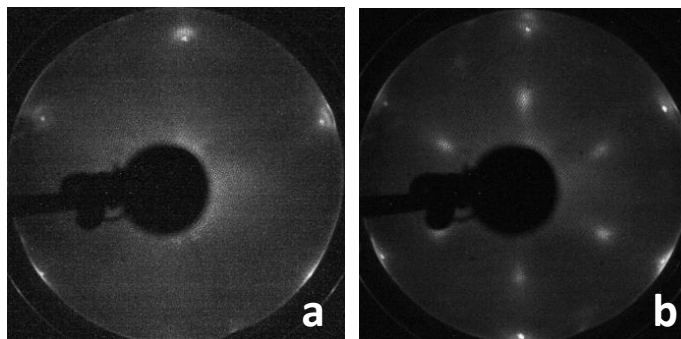
Figure 4.12 LEED patterns (60 eV) of an alloyed Zn-Pt(111) surface before (a) and after (b) annealing to 600 K

The reactivity of initially alloyed surface was comparable with that of some submonolayer ZnO films (see Fig.4.9a). And even post characterization by LEED did not show any ordered pattern, AES definitely revealed ZnO oxide formation (see Fig.4.13) due to high chemical potential of oxygen under reaction conditions. This conclusion is also supported by the first CO TPD after reaction, which is similar to that of preformed oxide films (see Fig.4.14, compare with Fig.4.11).
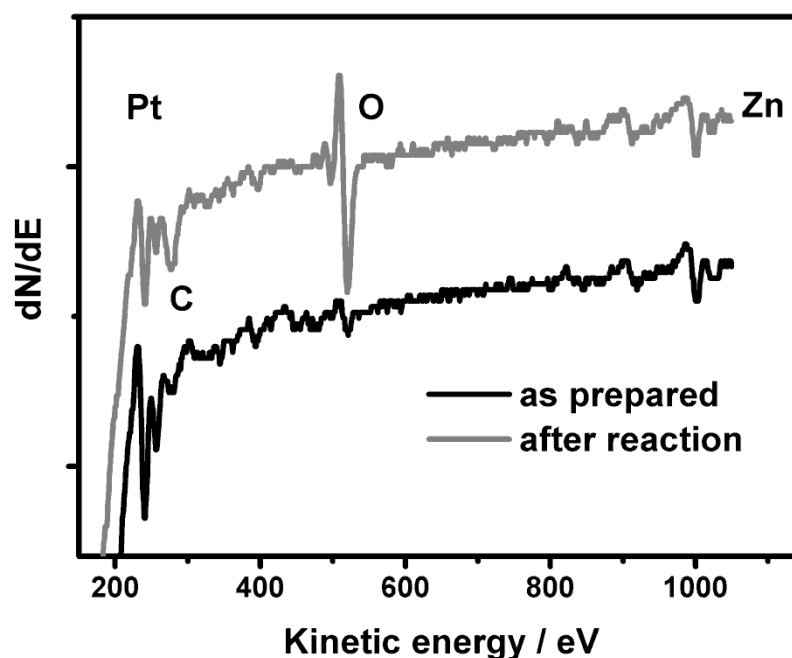
Figure 4.13 Auger spectra of an alloyed Zn-Pt(111) surface before and after reaction.
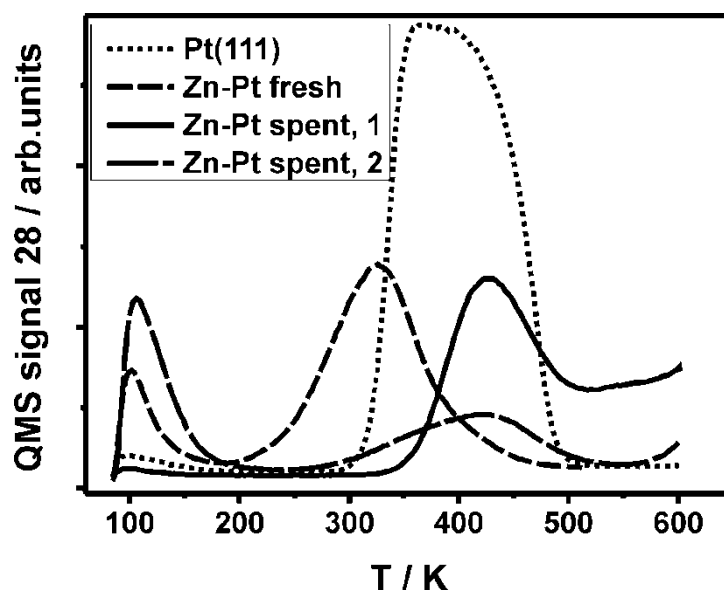
Figure 4.14 CO TPD for as prepared and post reacted surface of an alloy Zn-Pt(111). Heating rate β=3 Ks^{-1}

A temperature programmed reaction (TPR) was carried out (see Fig.4.15) over 1 MLE ZnO film with the nominal thickness ~ 1 ML to detect the point, when the reaction ignites: based on experiment an estimated value lies above 420 K. It is noteworthy that carbon contamination on the surface of the spent oxide film after TPR was *below* AES detection limit. This could be explained by constant increase of oxygen partial pressure during the reaction when CO gradually converts to CO_2, and, therefore, carbon deposits forming *in situ* are burnt.
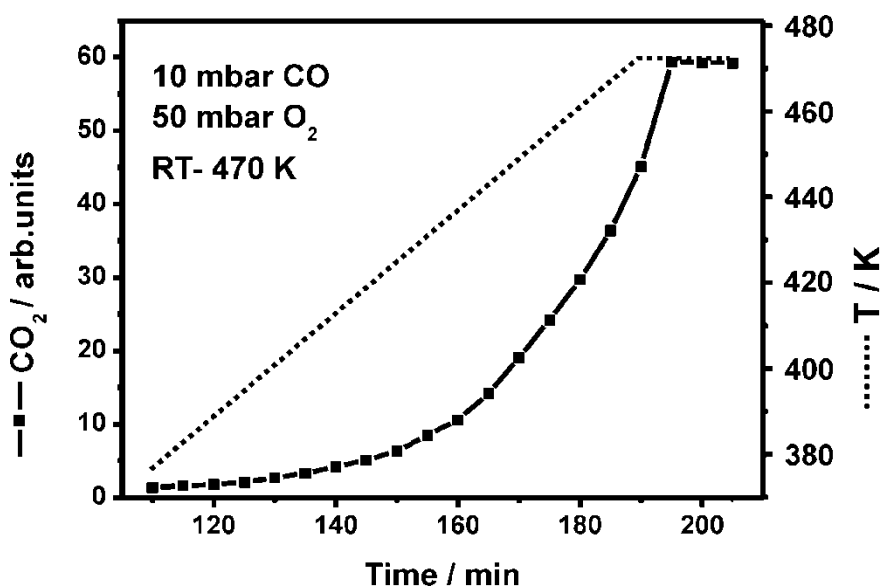
Figure 4.15 CO_2 production measured during TPR over 1 MLE ZnO film on Pt(111). Reaction conditions: 10 mbar CO + 50 mbar O_2, He balance to 1 bar; T=300-470 K, heating rate 0.02 Ks^{-1} (during the reaction). Here one-side polished Pt(111) crystal was used as a substrate.

Also the LEED pattern certified maintenance of the (6×6) superstructure (see Fig.4.16a and b) – at least in (0;0) in contrast to the case of a 'normal' catalytic run when this superstructure was vanished (see Fig.4.10). This can be a sign of the fact that thin ZnO films are able to restore their stoichiometry under oxidative conditions.
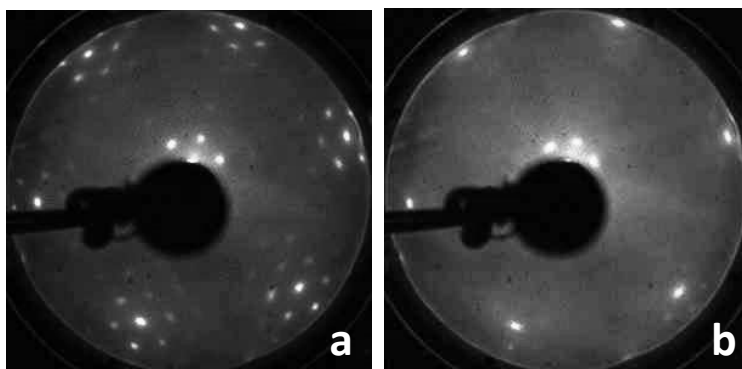

Figure 4.16 LEED patterns (60 eV) of 1 MLE ZnO film on Pt(111) before (a) and after (b) TPR.

4.3.2 Active phase formation and structural stability of ZnO films

In analogy with earlier works of our group on CO oxidation over ultrathin oxide films [14, 100] it was first proposed that the reactivity of ZnO films on Pt(111) possibly could be related to the new oxygen species formation under reaction conditions in excess of oxygen. To examine this, freshly prepared ZnO films (0.9, 1.1, 2.2, 5 MLE thick) were subjected to similar O_2 treatment: 20 mbar of pure O_2, 450 K, 10 min.

Thermal decomposition of the films evidenced only the presence of the lattice oxygen peak at ca. 1030-1100 K. Closed ZnO films did not possess any additional oxygen species. Partially covered films demonstrated a small extra-peak at lower temperatures, ca. 740 K. However, such a peak can be easily attributed to O_2 desorption from opened patches of the Pt(111) surface: this is well-documented in the work of Steininger with colleagues [133].

The morphology of the catalysts was studied by B.-H. Liu with STM *ex situ* [132]. For this, the well-defined films were exposed to the same reaction conditions (10 mbar CO, 50 mbar O_2, He balance, 450 K) in a high-pressure cell for 10 min. The sample was evacuated and transferred into analytical chamber via a gate valve and immediately scanned with STM at room temperature. The STM images of the "reacted" samples are displayed in Fig.4.17.

For the 0.25 MLE film, irregularly shaped islands of ~10 nm in lateral size are observed (Fig.17a). The film coverage is reduced to ~ 0.18 ML (which is most likely overestimated due to the well-known tip convolution effect for small objects). No monolayer islands, which dominated the surface of the "as prepared" film (see Fig. 4.8a), are observed anymore.

Instead, the particles are all about 4 Å in height, thus indicating the formation of two-layers thick (henceforth "bilayer") ZnO(0001) islands. Basically, similar behavior is observed for the 0.55 MLE film (Fig.4.17b): The surface coverage decreases to ~ 0.32 ML, and the Pt(111) support is covered with small ~ 4 Å-high islands and their aggregates. Finally, the 1.2 MLE film dewets as well, thus forming a 0.75 ML covered "bilayer" film (Fig. 4.17c).

For the all films inspected, only small amounts of ZnO are found in the third layer. The long range ordering via the Moire (6×6) superstructure seen on the "as prepared" films is hardly visible on the "reacted" films, in full agreement with the LEED data (Fig. 4.10).
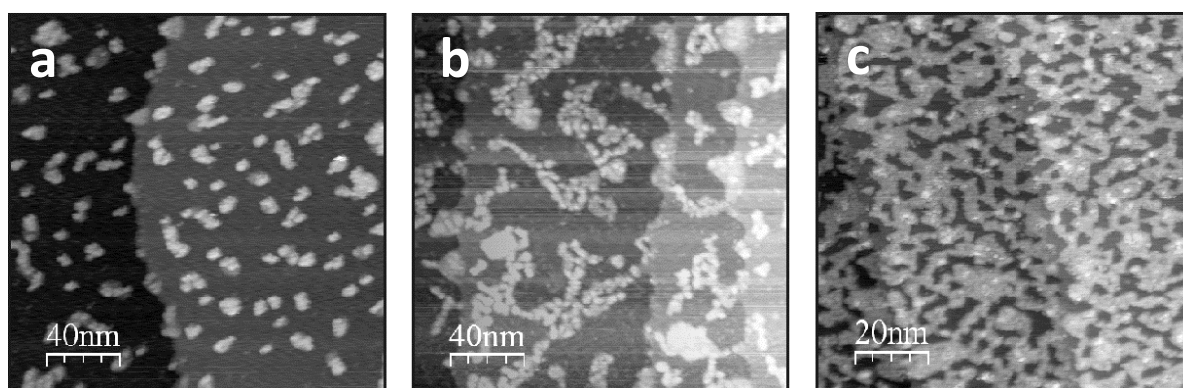
Figure 4.17 STM images of the "reacted" ZnO films at 0.25 MLE (a), 0.55 MLE (b) and 1.2 MLE (c) film thicknesses [132]. The images are provided by *B.-H. Liu and M.E. McBriarty.*

Observed structural change of 'postreacted' thin film surfaces correlates well with increased CO desorption from that samples as revealed by CO TPD. On Fig.4.18 (is presented with another focus than Fig.4.11) one can clearly see that ZnO dewets the Pt substrate under reaction conditions. The degree of dewetting is hard to quantify precisely because of the presence of carbonaceous deposits on the spent catalysts also contributes to CO signal by reaction with oxygen available in the system as it could be seen from the baseline rising up at T > 500 K.
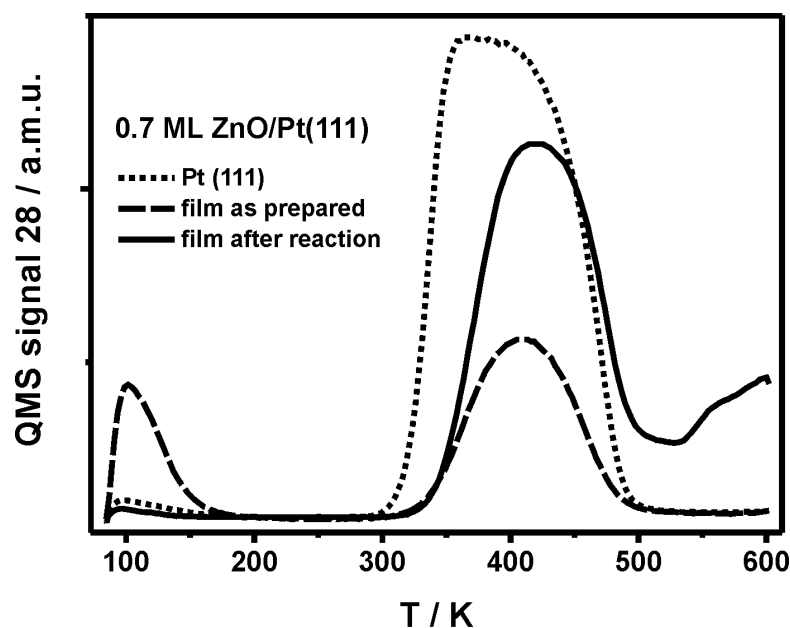
Figure 4.18 CO TPD spectra of the 0.7 ML film before and after the CO oxidation reaction: film dewetting. The spectrum of the clean Pt(111) is given as a reference. $\beta=3$ Ks^{-1}

Therefore, the STM results show that the CO oxidation reaction on ZnO/Pt is accompanied by substantial structural transformations such that monolayer islands (and a dense monolayer film) transform into the bilayer islands and their aggregates. Therefore, Pt surface opening observed by CO uptake measurements of the spent catalyst reflects, in fact, a higher stability of the *bilayer* structure at elevated pressures.

The exact mechanism and the driving force for the observed structural changes are hard to envision on the basis of the existing results. Note, however, that bilayer ZnO islands were also developed on Pd(111) at increasing oxygen pressures used for oxidation at 550 K [120]. Interestingly, bilayer islands were observed for $CeO_{2-x}(111)$ deposited onto Rh(111) [134] and Ru(0001) [135].

The rate enhancement on the metal surfaces partially covered by oxide is commonly rationalized in terms of the reaction occurring at the oxide/metal boundary. Indeed, the maximum in activity basically follows the perimeter length of the oxide/metal interface which goes to zero for a dense oxide film. The effect may result either from oxygen spillover from oxide to Pt or from the formation of highly active sites at the metal/oxide boundary. Since ZnO oxide is non-reducible oxide, the spillover mechanism seems to be not operative.

Previously, Hardacre et al. [136] found maximum in low temperature CO oxidation on $CeO_x/Pt(111)$ in the sub-monolayer regime. The coverage was measured by CO titration of

76

bare Pt(111). Reactivity was measured in a high-pressure cell used as a batch reactor filled with ~ 10 Torr of stoichiometric (2:1) CO + O_2 mixture at crystal temperature of 320 – 430 K. The authors found that the reaction rate increased between zero and 0.5 ML, after which it dropped almost to zero at 0.8-1.3 ML, but again increased steeply to a value which is greater than that observed over the clean Pt(111) surface.

It was suggested that for the coverages below 1 ML the reactivity is associated with the metal/oxide interface. The high reactivity of the fully encapsulated Pt(111) (as judged by CO TPD *before* the reaction) was rationalized in terms of a proposal made by Frost [137], according to which electron transfer from a metal phase to an oxide phase reduces the enthalpy for oxygen vacancy formation in the oxide. However, the authors argued themselves that there was no absolute evidence of total encapsulation of the Pt crystal. In particular, the sample morphology *after* the reaction was not defined in this work. The initially dense oxide film could dewet, ultimately forming CeO_x particles on Pt(111).

Nonetheless, the rate vs thickness plot observed for CeO_{2-x}(111)/Pt(111) system is very different from that shown in Fig.4.9b for ZnO(0001)/Pt(111). While "thick" ceria films (~ 10 MLE) were much more active than Pt(111), the reactivity of ZnO(0001)/Pt(111) dies away with increasing the film thickness. The difference may be related to the fact that ceria, well-known for the oxygen storage-release properties, readily provides weakly bound oxygen to react with CO, whereas ZnO as non-reducible oxide does not.

Recently Sun et al. [138] performed density functional theory studies of the 3d transition-metal oxide (TMO) nano-islands on Pt(111) in low-temperature CO oxidation in order to identify the active sites at the TMO/Pt boundaries. A Pt–cation ensemble was proposed, where coordinatively unsaturated TMO cations exposed at the edges of oxide nanoislands are highly active for O_2 adsorption and dissociation, and less-reactive Pt binds modestly with dissociated O responsible for the facile CO oxidation. But, in all these calculations the TMO islands were only one monolayer in thickness, which is not the case under technically relevant conditions as shown here for ZnO(0001) and previously for FeO(111) on Pt(111) [14]. Therefore, our results provide more adequate structural models for TMO/metal "inversed" catalysts.

The so called 'inverse' catalysts in the CO oxidation reaction, when reactants interact on the oxide-metal interface, are already well-known in the literature, e.g. for such cases like $VO_x/Pd(111)$, $VO_x/Rh(111)$, $CeO_x/Pt(111)$, $SnO_x/Pt(111)$ and $CeO_x/Cu(111)$ respectively [139-143]. However, the first four reported studies utilize low pressure reaction conditions. In the work with $CeO_x/Cu(111)$ [143] Yang et al. performed the reaction at elevated pressures (20 Torr CO, 10 Torr O_2, 475-575 K), but formation of copper oxide phases obscured establishing the active phase.

The idea of the active oxide/metal interface is a wide explanation and can include, at least, three potential pathways. These suggestions are roughly depicted on Fig.4.19 and marked respectively as 1, 2 and 3. The most reasonable one can involve CO adsorption on Pt sites and reaction with oxygen adsorbed on oxide film or coming from its lattice to produce CO_2 (1). Another scenario can be opposite to the first one: CO adsorbs on some defect sites of ZnO (e.g. Zn or O vacancies) and further interacts with atomic oxygen dissociated on Pt (2). Even if the electron transfer seems to be not the case for ZnO/Pt(111), as it was proven experimentally and theoretically for FeO/Pt(111), the third way can be true when Zn-Pt pair (not an alloy) as a local junction creates electronically modified area, and both reactants can easier adsorb at the oxide/metal boundary and combine with each other (3).
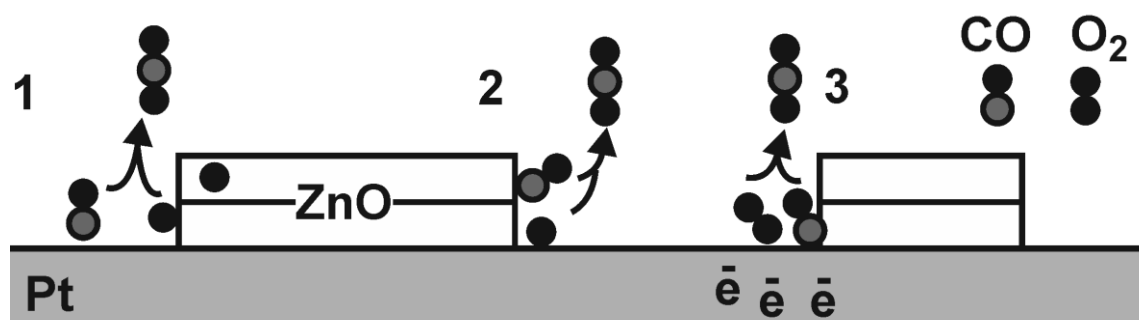

Figure 4.19 Schematic representation of possible pathways of the reaction mechanism of CO oxidation over ZnO/Pt(111) bilayer islands.

Thermal stability of ZnO films was studied by TPD. Experiments conducted with the films prepared on two different Pt(111) substrates (one- and two-side polished single crystals) have shown the same trend: the leading edge of the molecular oxygen peak for films thicker than 2 MLE is shifted to higher temperatures (see Fig.4.20). This could serve as

an evidence of substantial difference between thin and relatively thick films, being a sign of strained geometry: the stress, originated from the lattice mismatch between Pt(111) and ZnO(0001) and accumulated in thin films, releases upon thickness increase. A transition thickness of ca. 2 MLE differentiates ZnO ultrathin films with particular properties from already bulk-like thicker films. This issue needs further investigations.
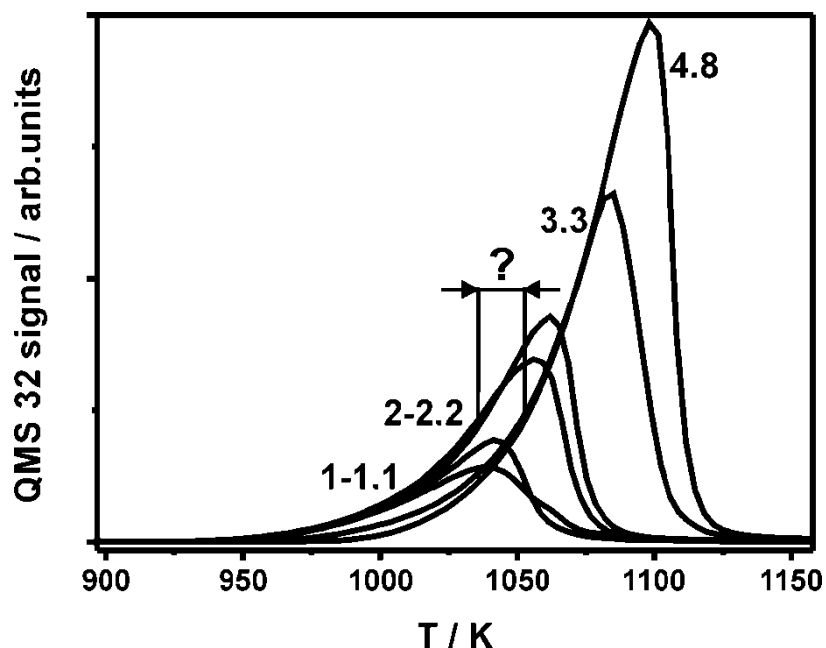

Figure 4.20 TPD spectra of molecular oxygen from decomposition in UHV of 'as prepared' ZnO films grown on two different Pt(111) crystals. Heating rate β=3 Ks^{-1}

Also in this respect a question of surface termination might be interesting, even observed for *ZnO single crystals*. Previously cited STM studies of Diebold's group certified the height difference between Zn- and O-terminated ZnO(0001) surface [128]: ~ 2.7 Å single step for (0001)-Zn against ~ 5.3 Å for double layer step of (000-1)-O phase.

Moreover, Lauritsen et al. in their combined study with high-resolution scanning probe microscopy (SPM), X-ray photoelectron spectroscopy (XPS), near edge X-ray absorption fine structure (NEXAFS) spectroscopy experiments, and density functional theory (DFT) calculations explain higher probability of existence of (000-1)-O surface by a higher bonding flexibility of the exposed 3-fold coordinated surface Zn atoms as compared to O atoms [144].

4.4 Summary

- Well-ordered ultrathin ZnO(0001) films on Pt(111) are shown to grow in a layer-by-layer mode. The films are examined in the CO oxidation reaction as a function of the film thickness. At low temperatures (~450 K) and near-atmospheric pressures, CO_2 production is much higher on the partially covered films than on the dense ZnO(0001) films and bare Pt(111).

- Under reaction conditions, both monolayer islands and a monolayer film transform into bilayer islands, which dominate the surface of the active catalysts. The results provide more adequate structural model than previously suggested for elucidating the reaction mechanism on the active oxide/metal boundary at technically relevant conditions. Stability of the ZnO bilayer structure at elevated pressures shows that the active phase differs from the pristine one stable and observed under UHV conditions. Therefore, the present work demonstrates, how the ZnO surface may respond dynamically to changes in the surrounding ambient atmosphere at elevated pressures.

Chapter 5

CO oxidation over manganese oxide films on Pt(111)

5.1 Catalytic activity of MnO$_x$-based materials and growth of MnO$_x$ films

Besides industrial applications of various bulk manganese oxides, e.g. related to *energy storage* [145-147], they as high area porous crystalline materials have an own niche in heterogeneous catalysis. Manganese oxide was reported to promote *CH$_4$ dry reforming by CO$_2$* to CO and H$_2$ (syngas) through mobility facilitation of bulk lattice oxygen [148]. Stabilized by alkaline additives MnO$_x$ were shown to be active in *oxidative coupling of methane* (OCM), where strongly bound (lattice) oxygen is responsible for selective methane coupling, while weakly bound oxygen - for conversion of CH$_4$ to CO$_2$ (exhaustive oxidation) [149, 150].

Manganese oxides are known to be active catalysts in ethylene [151] and alcohols [152] oxidation; NO [153], H$_2$O$_2$ [154] and O$_3$ [155] decomposition; selective catalytic oxidation of NH$_3$ [156], oxidative dehydrogenation ethylbenzene to styrene [157], selective catalytic reduction of NO with NH$_3$ [158], CO [159] and C$_2$H$_4$ [160] hydrogenation. The catalytic activity has been attributed to the capability of Mn to form several oxides and to store and provide oxygen selectively from its lattice. Because of its labile oxidation state, Mn is capable of playing the role of either a reducing agent that is oxidized (Mn^{2+} - ē → Mn^{3+} - ē → Mn^{4+}) or an oxidizing agent that is reduced (Mn^{4+} + ē → Mn^{3+} + ē → Mn^{2+}).

MnO$_x$-based catalysts are utilized for industrial *wastewater treatment* through catalytic wet air oxidation to degrade harmful organic pollutants [161]. Another environment related use of MnO$_x$ compounds refers to *oxidation of volatile organic compounds* (VOCs) [162]. In that work authors proposed that lattice oxygen was involved in the VOCs oxidation, suggesting that the reaction could proceed via the *Mars-van Krevelen mechanism*. Additionally, the conversion was found to be influenced by the type of VOCs and catalysts provided by the shape-selectivity of MnO$_x$ porous materials, *octahedral molecular sieves* (OMS) [163, 164]. Manganese oxides nanoparticles can biomimetically catalyze *water oxidation* in artificial photosynthesis to produce molecular oxygen O$_2$ [165].

Catalytic CO oxidation over various kinds of individual and mixed manganese oxide phases is in general overviewed by Royer and Duprez [166]. In detailed experimental studies of Kruse's group with MnO_x nanocrystals [167] the authors conclude that key requirement for catalytic activity is nanosize of MnO_x particles (as proven by transmission electron microscopy (TEM)) and, thus, high specific surface area of the catalysts. Based on CO oxidation in absence of O_2 it was proposed that due to excess of oxygen in surface region the Mars-van Krevelen type reaction mechanism is most likely in operative.

This is in agreement with the work of Baltanas et al. with highly dispersed overlayers of MnO_x [168]. They found that the reaction has the first order for CO and O_2. The amount of active oxygen on the surface is directly proportional to the catalytic activity, and is less than 10% of the total surface oxygen. The authors highlight that this active oxygen does not correspond to a labile moiety but is a part of the structural oxygen of the surface.

To differentiate several forms of oxygen bonds on the surface of oxide solids including manganese oxides, *oxygen isotope exchange* was utilized using O^{18}-labeled O_2, CO and CO_2 molecules, as it is reviewed by Novakova [169]. Recent studies of Fishman et al. [170] with MnO_x 'nanopowders' supported known regularities on the new level.

Catalytic properties of MnO_x-based materials mentioned above refer to studies where the catalysts were prepared by 'wet chemical' methods and tested either at atmospheric pressures or higher and over the wide temperature range (mostly elevated). Single crystalline MnO_x surfaces or metal-supported thin films have never been reported to be an object of studying any catalytic reaction. However, there is plenty of literature focused on growth and structure of MnO_x thin films of different thickness and stoichiometry.

Manganese oxide thin films were reported epitaxially to grow on a number of well-known substrates in surface science, namely on Ag [171], Pd [172], Pt [173] and Rh [174]. Upon multitechnique research (with LEED, X-ray photoemission spectroscopy (XPS), STM, X-ray photoelectron diffraction (XPD) and X-ray absorption spectroscopy (XAS)) on MnO(001)/Ag(001) it was found that MnO films few nm thick are strained and tetragonally distorted, while the thicker films evidently adopt bulk structure and bulk lattice constants [175-177]. However, MnO films can intermix with Ag(001), forming embedded layers [178].

A variety on MnO_x phases (in total nine) of different orientation and stoichiometry (e.g. MnO - (001), (100), (111), Mn_3O_4 - (001)) was revealed on Pd(100) as a function of the chemical potential of oxygen and thickness in works of Netzer's group [172, 179-180], where the data were collected from LEED, STM, XPS, XAS, high-resolution electron energy loss spectroscopy (HREELS) and atomic force microscopy (AFM) methods.

In studies of Widdra's group [173, 181] vibrational and electronic properties of manganese oxide films grown on Pt(111) were presented to be thickness dependent, as proved by HREELS technique: new excitations are observed below 4 ML, while films adopt the bulk-like structure comparable with that of single crystals already from the thickness ca. 4 ML. Additional LEED and STM characterization and TPD measurements demonstrated existence of different phases as a function of O_2 partial pressure and the substrate temperature during the film preparation. The film coverage was calibrated by CO TPD.

The hexagonal structure of MnO monolayer on Rh(100) was found and explained by Nakamura's group [174], based on LEED and STM studies. Such model system was proposed potentially to have a meaning for CO hydrogenation reaction. Recently, by Zhang et al. [182] MnO_x thin films were shown to grow on Rh(111) as an O-Mn-O like trilayer, above that coverage it continued to develop as Mn_3O_4 structure, as detected by combination of LEED, AES, XPS, HREELS and low energy ion scattering spectroscopy (LEIS) techniques.

It is worth to underline, that, in spite of availability of numerous studies regarding structural properties of MnO_x thin films, the information about small molecules adsorption in UHV on ordered individual MnO_x surfaces is still missing.

The idea about highly reactive surface oxygen species was already clearly introduced for the bulk and supported manganese oxides. Therefore, for me in the current work it was reasonable to perform catalytic studies of a model reaction, e.g. CO oxidation over ultrathin MnO_x films grown on a suitable substrate like Pt(111) in order to detect and prove the formation of new oxygen species under well-defined conditions, identify their nature and establish thickness-reactivity dependence if any. Moreover, the comparison of the reactivity of MnO_x/Pt(111) model catalyst at near-atmospheric pressures and low temperatures with that of FeO/Pt(111), RuO_x/Ru(0001) and ZnO/Pt(111) sounds interesting.

5.2 Structure of materials and thin film preparation

As a 3d-transition metal manganese with an electronic configuration [Ar] $4s^2$ $3d^5$ can form a large variety of oxides with the oxidation state between +2 and +7. Most commonly known of them are crystalline polymorphs of MnO, Mn_3O_4, Mn_2O_3 and MnO_2 stoichiometry, which basic data are compiled in Tabl. 5.1 [145, 183-185] (their literature nomenclature is often contradictory). Corresponding structures of most stable allotrope modifications are shown below in Fig.5.1. Here I overview materials consisting only of Mn and O ions, since detailed description of geometry of substituted forms, hydrates and minerals is beyond the scope of the present work. Temperature dependent magnetic properties of manganese oxides, which are intimately connected to materials geometry, are not overviewed as well. From my point of view such *extended structural information* about bulk manganese oxides as compared to corresponding sections in previous chapters is reasonable since MnO_x show much higher complexity in this respect than ruthenium and zinc oxides.
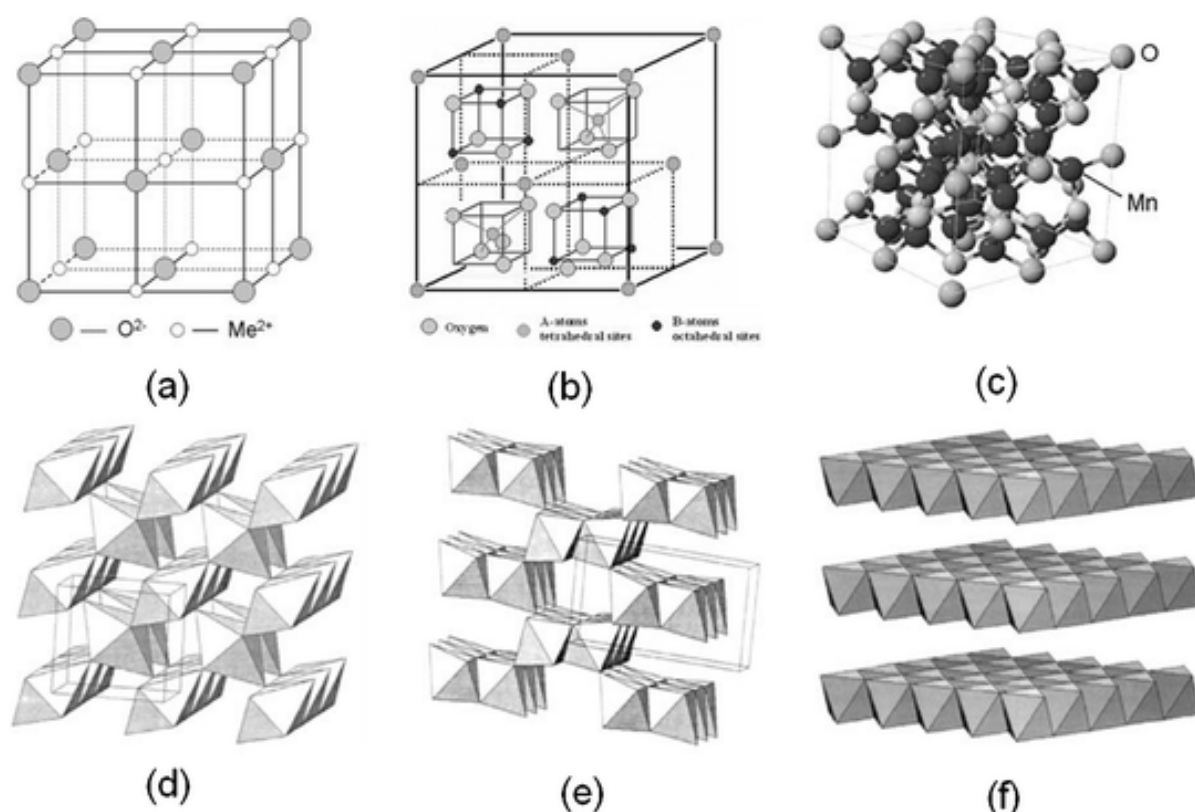
Figure 5.1 Schematic representation of bulk manganese oxides [145]. (a) Rock salt; (b) spinel (Mn_3O_4); (c) bixbyite (Mn_2O_3); (d) pyrolusite β-MnO_2 (rutile -type); (e) ramsdellite; (f) phyllomanganate

Table 5.1 Crystal structure of bulk manganese oxides

Formula	Trivial name	Symmetry	Structure type	Unit cell				Cleavage
				a	b	c	β	
MnO	manganosite	cubic	Rock salt (at room temperature) - face centered cubic (FCC) lattice with a 6 : 6 octahedral coordination.	4.44				100, 010, 001, 111
		rhombohedral (4.2 K)		4.43				
Mn_3O_4	α-, hausmannite	tetragonal distorted	Spinel - metal cations occupy 1/8 of the tetrahedral sites and 1/2 of the octahedral sites and there are 32 oxygen anions in the FCC unit cell.	5.76		9.47		001, 100, 110, 010
	β-	cubic (≥ 1170^{0}C)	spinel	8.55				
Mn_2O_3	α-, kurnakite	orthorhombic distorted		9.41	9.42	9.40		
	β-, bixbyite	cubic (≥ 302 K)	Body-centered cubic (BCC) unit cell with 16 formula units per unit cell. Fe ions	9.41				110, 111
	γ-		spinel					
MnO_2	α-, hollandite	monoclinic	Cross-linking of double or triple chains of the [MnO_6] octahedra, resulting in (2×2) opened tunnels within the lattice. Ba ions	10.03	2.88	9.73	91.03	
	α-, cryptomelane	monoclinic	-//-. K ions	9.96	2.87	9.71	90.95	
	β-, pyrolusite	tetragonal	Rutile structure with an infinite single chain of [MnO_6] octahedra running along the [001] direction and sharing opposite edges; each chain is corner-linked with four similar chains, forming (1×1) square cavities.	4.40		2.87		110, 100, 101
	R-, ramsdellite	orthorhombic	Closely related to rutile except that the single chains of edge-sharing octahedra are replaced by double chains, resulting in (1×2) channels.	9.27	2.87	4.53		
	γ-, nsutite	hexagonal	An irregular intergrowth of layers of pyrolusite and ramsdellite.	9.65		4.43		
	δ-, vernadite	preuso(tetragonal)	Layered structure, containing infinite two-dimensional sheets of edge-shared [MnO_6] octahedra. nH_2O	9.87		2.84		
	ε-, akhtenskite	hexagonal	Defective NiAs hexagonal close packing of anions, with Mn^{4+} statistically distributed over half the available octahedral interstices	2.84		4.6		
	λ-	cubic	Spinel with channels	8.04				
	η-		Different from γ -MnO_2 only in crystallite size and the concentration of microdomains of pyrolusite within the ramsdellite matrix					

There are not so many known experimental studies of the surface properties of manganese oxides single crystals due to charging problems. However, Langell et al. reported selective oxidation/reduction of *Mn(100) substrate* and epitaxial growth of Mn_2O_3 and Mn_3O_4 like surfaces under UHV conditions as supported by HREELS and XPS characterization [186]. The authors conclude that the ready formation and intermixture of these species imply that the redox properties of manganese oxide surfaces are important in their surface chemical reactivity and gas adsorption characteristics.

Later, unreconstructed and clean *Mn(001)-(1×1) surface* was successfully prepared by cleavage in N_2 ambience by Okazawa and Kido [187] and analyzed with reflection high energy electron diffraction (RHEED) and high-resolution medium energy ion scattering (MEIS) techniques. Long annealing in O_2 at too high temperatures and pressures led to the surface amorphization. Annealing at lower O_2 pressures generated oxygen vacancies at the surface.

Formation of *$Mn_3O_4(001)$ phase* on MnO(001) surface was shown in experimental-theoretical study by Bayer et al. [179] (methods are indicated in Sec.5.1). Authors computed low strain energy and proposed realistic models for the interface, even with 9% lattice mismatch between two phases on the interface.

Gorbenko et al. [188] grew thick ordered films of Mn_3O_4 (100 nm) on MgO(001) and SrTiO$_3$(001) single crystals and characterized them by X-ray diffraction (XRD), Raman spectrometry (RS) and high-resolution transmission electron microscopy (HRTEM). On MgO (001) only *domains of (001)[100]Mn$_3$O$_4$//(001)[100]MgO* symmetry were observed, while on SrTiO$_3$(001) different orientations were detected: *(001)[110]Mn$_3$O$_4$//(001)[100]SrTiO$_3$, (001)[110]Mn$_3$O$_4$//(001)[100]SrTiO$_3$ and (101)[010]Mn$_3$O$_4$//(001)[110]SrTiO$_3$.*

Natural pyrolusite and synthetic *MnO_2* material surfaces were both shown to crystallize in *[110]* direction, meanwhile exposing other planes as well according to HRTEM images of Yamada et al [189] and Zheng et al. [190] respectively.

Bulk-terminated polar MnO(111) phase first was calculated with DFT by Franchini et al. [191]. They reported unreconstructed O-terminated (1×1)-MnO(111) surface to be stable at high oxygen pressures. Previously MnO(111) thick films (200-3500 Å) were epitaxially grown on sapphire(001) and MgO(111) by a pulsed layer deposition (PLD) by Neubeck et al. [192]. Films orientation was proven by XRD, grazing incidence diffraction (GID), X-ray reflectometry and Rutherford Back Scattering (RBS) methods.

Under some preparation conditions an oxygen-terminated monolayer film *O-MnO(111)* was suggested to exist on Pt(111) substrate in a form of a *O-Mn-O trilayer* (see Fig.5.2 for clarity) with *MnO_2 stoichiometry* by Sachert (Widdra's group) [193]. Top layer of oxygen was found to be weakly bound as compared to MnO(19×1)-Pt(111).
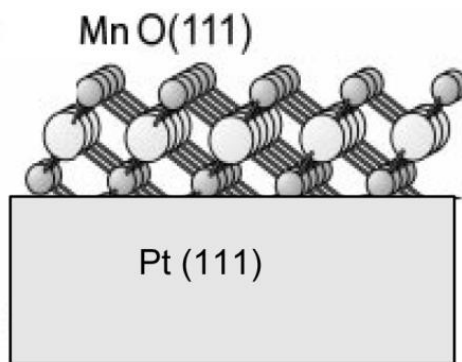
Figure 5.2 Structural model of an oxidized MnO monolayer film on Pt(111). Large and small balls refer to Mn and O atoms correspondingly [193].

In this work thin manganese oxide films of different structure and stoichiometry were prepared using conditions adapted from [173, 181, 193]. Manganese was evaporated at room temperature on a biased Pt(111) crystal by e-beam assisted (reactive) physical vapor deposition (PVD) in either UHV or O_2 ambient (~ $5 \cdot 10^{-8}$ mbar) from a metallic Mn rod (2 mm in diameter, 99.5%, Goodfellow). The deposition flux was controlled via a quartz microbalance (QMB).

'O-poor' MnO_x phases were obtained by postoxidation of Mn deposits at 700-1000 K for several minutes in 10^{-6} mbar O_2. Structures with higher oxygen content were produced by oxidation of Mn deposits in 10^{-4} mbar O_2 at 700 K for 5 min. 'O-rich' MnO_x phase was prepared by oxygen treatment of any 'O-poor' phase in 20 mbar O_2 at 450 K for 10 min in the HP cell.

Monolayer films deposited in UHV and annealed in O_2 below 850 K demonstrated a *(19×1) LEED pattern and Mn:O=1:1 stoichiometry in AES* (that corresponds to the peak ratio of 1.67) as shown on Figs.5.3a and 5.4. The (19×1) LEED pattern is a result of superposition of three 120°-rotational domains with (2.37×1) periodicity as proposed in [173]. Therefore, based on such characterization fingerprints, films were attributed to *MnO(100) monolayer* uniaxially reconstructed on Pt(111).

O_2-deposited films annealed in O_2 at T ≥ 850 K displayed a LEED pattern (see Fig.5.3b) not yet identidied due to its complexity. Elemental composition yielded Mn:O ratio ranging between 1.2 and 1.4 (see Fig.5.4, overlaps with MnO). A phase with these characteristics was assigned [193] to *Mn_3O_4*. It can convert to MnO(100) structure upon heating in UHV to 1190 K or obtained by MnO reoxidation in O_2 ambient at T>850 K.

O-rich phase formed from either MnO or Mn_3O_4 under mbar O_2 pressure at 450 K exhibited a diffused *(1×1) LEED* pattern with high background intensity. This could be explained by the *oxide surface amorphization*, while Pt spots at 1 ML film thickness are still visible (see Fig.5.3c). Or domains of an ordered structure are too small and have multiple orientation. Meantime, the chemical potential of oxygen was high enough to result in double increase of its amount and, therefore, in *MnO_2 stoichiometry* as judged by AES (see Fig.5.4). Direct deposited Mn oxidation in 10^{-4} mbar O_2 at 700 K led to a structure with a similar pattern as in HP cell, however, slight onset of a weak Moiré superstructure could be distinguished (see Fig.5.3d). If latter would be fully developed, it could be assigned to *O-Mn-O trilayer of O-MnO(111)* possessing a well-pronounced (1×1) Moiré pattern [49].
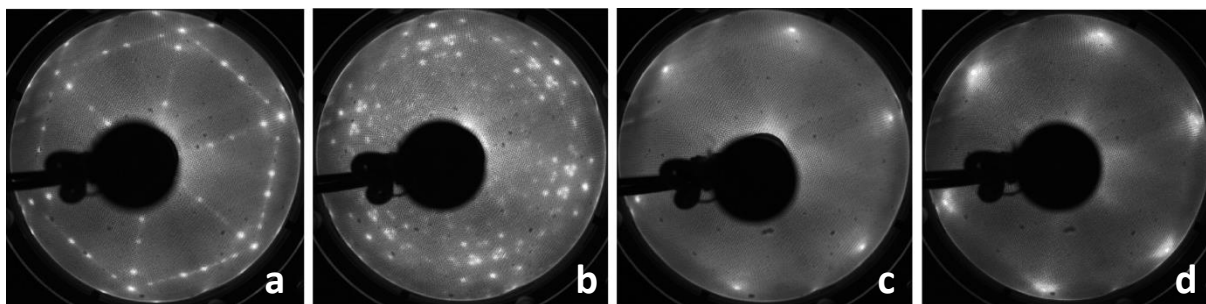
Figure 5.3 LEED patterns of 1 ML MnO_x films on Pt(111) at 70 eV: a - MnO, b - Mn_3O_4 and c(RT), d(700 K) - MnO_2.
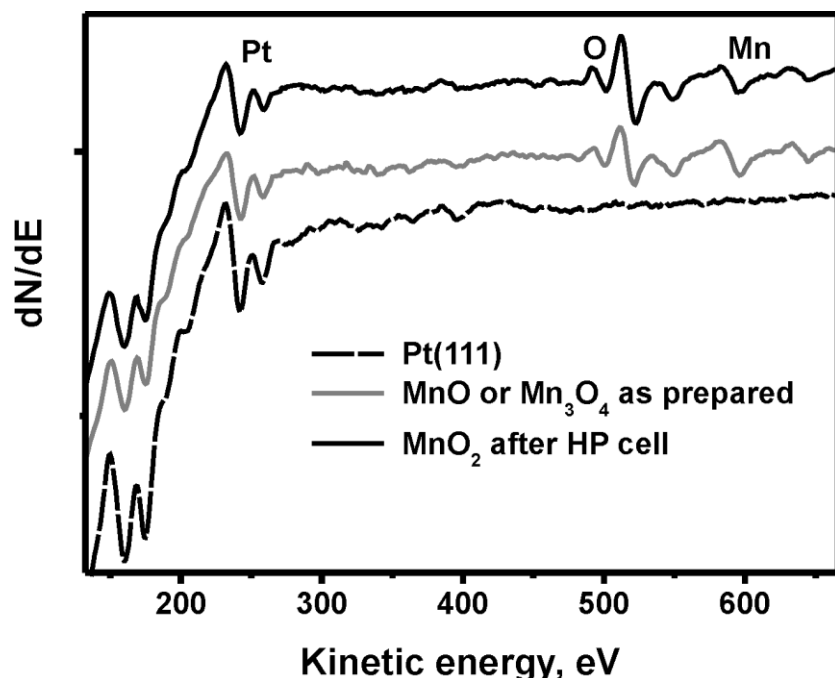
Figure 5.4 AES of 1 ML MnO$_x$/Pt(111) subsequently oxidized through MnO, Mn$_3$O$_4$ and MnO$_2$ steps.

The surface coverage was measured by CO titration of Pt sites using TPD of CO that desorbs from Pt(111) at 300 – 500 K.

5.3 Results and discussion

5.3.1 Active phase formation and special requirements for its existence.

Catalytic reactivity of bulk and supported MnO$_x$ materials in various chemical processes overviewed in Sec.5.1 as well as structural studies of O-MnO(111) film on Pt(111) [193] already documented existence of other forms of oxygen different from oxide lattice. Therefore, prior to start studying the reactivity, in a separate series of experiments the 'as prepared' 1 ML films were exposed to O$_2$ in HP cell and then thermally decomposed in UHV. A TPD profile depicted on Fig.5.5 clearly indicates three peaks of molecular oxygen desorption - 950, 1060 and 1230 K respectively. Peak positions allow to conclude that chemical composition is virtually similar to that of the O-Mn-O trilayer [193].
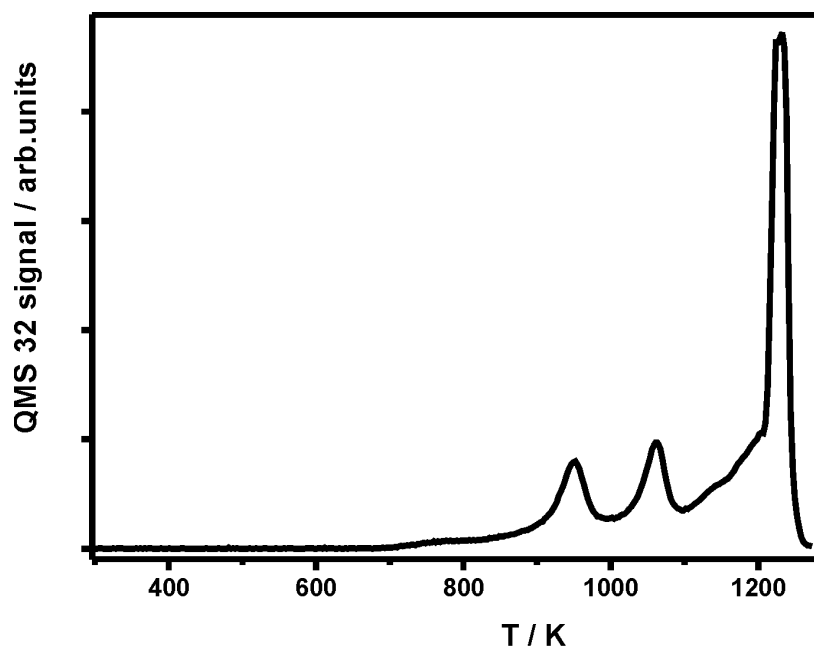
Figure 5.5 TPD profile of MnO$_x$/Pt(111) pretreated with O$_2$ (20 mbar, 450 K, 10 min), β=3 Ks^{-1}.

However, peaks integrated area ratio confirms the coexistence of MnO$_2$ and Mn$_3$O$_4$ rather than pure MnO$_2$ in contrast to [193] where the presence of Mn$_3$O$_4$ in the TPD spectrum is almost negligible. It means that during decomposition upon losing oxygen MnO$_2$ is followed by Mn$_3$O$_4$ and finally MnO.

Initially the reactivity measurements for CO oxidation were performed under the same conditions used for other oxide films in the present work (RuO$_x$/Ru(0001) and RuO$_x$/Pt(111), ZnO/Pt(111)) and earlier studies of our group (FeO/Pt(111)): namely in a mixture 10 mbar CO+50 mbar O$_2$, balanced by He up to 1 bar, at 450 K. On Fig.5.6 a kinetic curve of CO$_2$ production over a monolayer MnO$_x$ film is compared with that of a monolayer FeO film and bare Pt(111) surface. The reactivity of MnO$_x$/Pt(111) is lower than over the FeO film and just slightly above that of the Pt(111) substrate. After a short working period, CO oxidation slows down and stops.

Characterization of the postreacted oxide surface has shown that the film underwent severe dewetting as well as O-depletion accompanied by C deposits. This was concluded from a characteristic shape of the CO TPD profile (see Fig.5.7a) and a Pt(111)-c(4×2)CO LEED pattern

90

(see Fig.5.8a), both comparable with that of postreacted Pt(111) in a blank experiment. Subsequent heating to 600 K in the CO TPD run led to wetting of the most part of the Pt surface by MnO_x film with the development of the (19×1) LEED pattern (see Fig.5.8b). The film decomposition revealed no additional O_2-peaks besides the lattice one at ~ 1200 K (see Fig.5.7b).
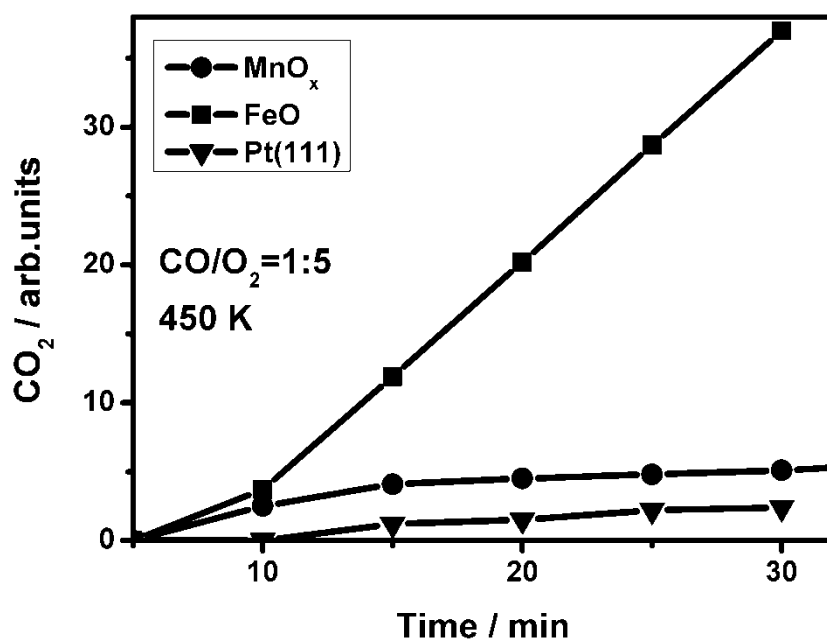
Figure 5.6 Kinetics of CO oxidation over 1 ML MnO_x film on Pt(111) at $CO:O_2$=1:5. Reaction conditions: 10mbar CO+50 mbar O_2, balanced by He to 1 bar; 450 K, heating rate 1 Ks^{-1} (to reach 450 K). Kinetic curves for 1 ML FeO film on Pt(111) and clean Pt(111) are given as a reference.
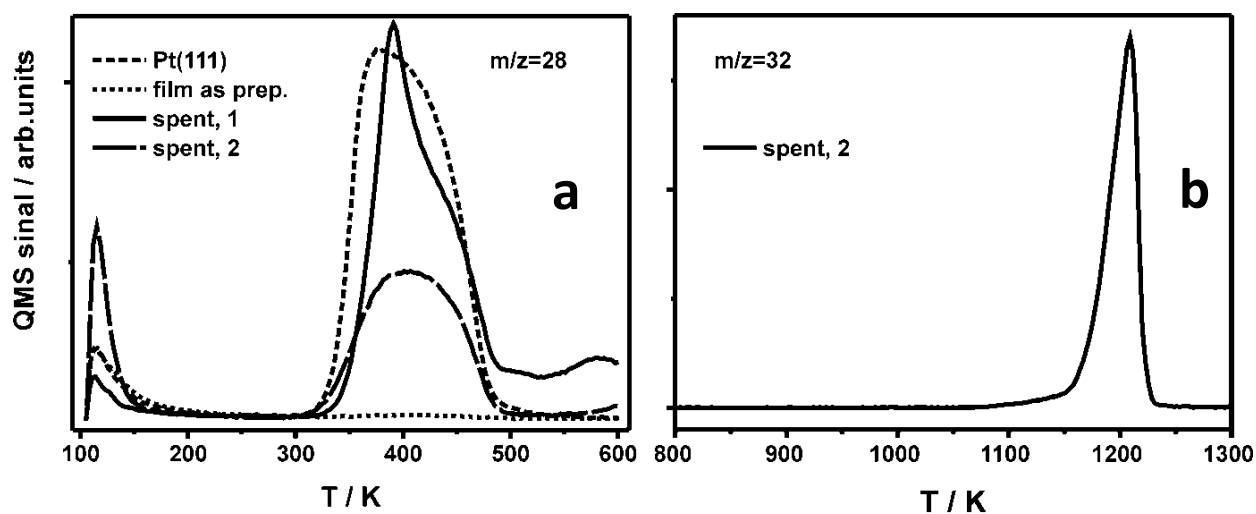
Figure 5.7 CO TPD (a) of 1 ML MnO_x/Pt(111) and its decomposition (b) after reaction with CO/O_2=1:5, β=3 Ks^{-1}.
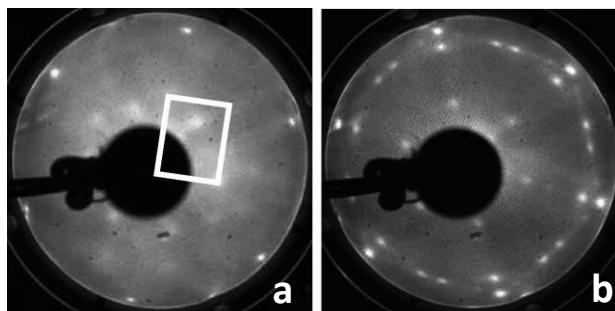
Figure 5.8 LEED patterns (70 eV) of a spent 1 ML MnO_x/Pt(111) after the reaction CO/O_2=1:5 (a) and CO TPD (b).

In attempts to prevent film dewetting, in the next experiments we increased CO/O_2 ratio from 1:5 to 1:10, keeping the total pressure of reactants to 60 mbar. Upon increase of $CO:O_2$ to 1:10 in the reaction gas mixture, the film catalyzes CO oxidation with a much higher and constant reaction rate (see Fig.5.9). CO titration experiments confirmed that the film does not dewet (see Fig.5.10a). Additionally, during thermal decomposition in UHV of postreacted oxide surface the profile of O_2 spectrum demonstrates O-states similar to that observed for the surface pretreated in pure oxygen (see Fig.5.10b). To compare, FeO/Pt(111) was also tested at CO/O_2=1:10 for the reference. Again, as in the case of CO/O_2=1:5 (see Fig.5.6), FeO/Pt(111) has shown the reaction rate higher than MnO_x/Pt(111), namely more than twice.
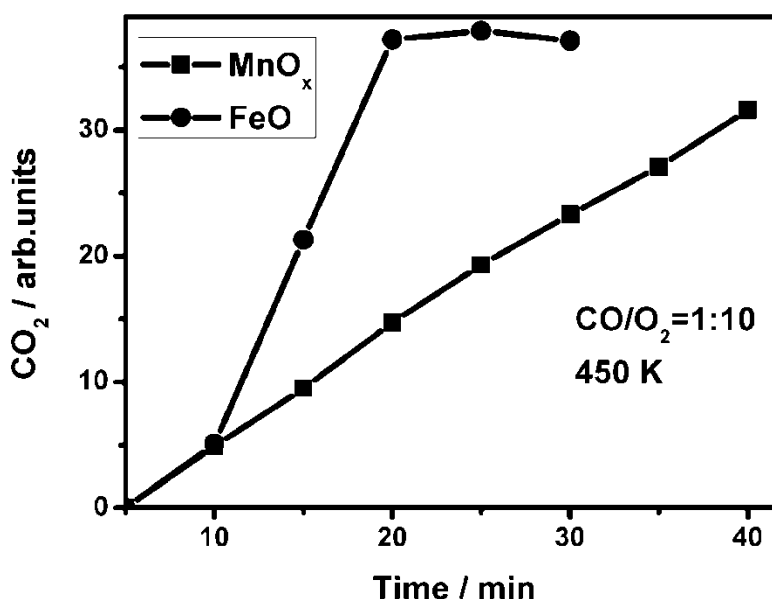
Figure 5.9 Kinetics of CO oxidation over 1 ML MnO_x film on Pt(111) at $CO:O_2$=1:10. Reaction conditions: 5.45 mbar CO+54.55 mbar O_2, balanced by He to 1 bar; 450 K, heating rate 1 Ks^{-1} (to reach 450 K). A kinetic curve for 1 ML FeO film on Pt(111) is given as a reference.

92
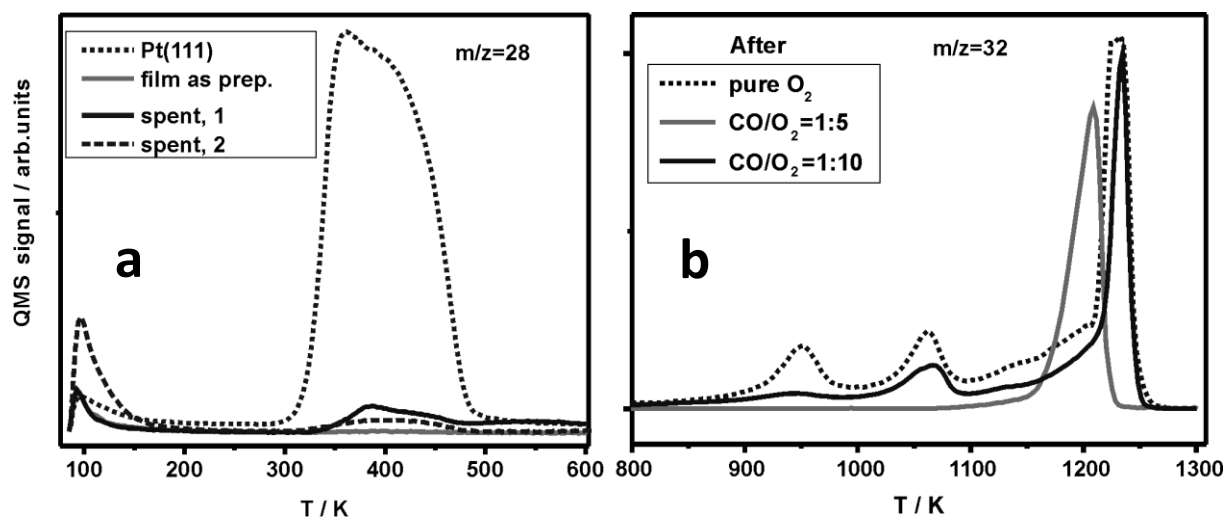
Figure 5.10 CO TPD (a) of 1 ML MnO$_x$ film on Pt(111) and its decomposition (b) after reaction with CO/O$_2$=1:10, β=3 Ks^{-1}.

5.3.2. Oxygen states differentiation

Additional structural characterization of the similarly prepared oxide surfaces (including multilayer films) was performed MAX-lab beamline I511 (Lund University, Sweden) [194]. Briefly, the preparation UHV chamber of the endstation was equipped with LEED, QMS, sputter gun and a load lock for sample transfer without breaking vacuum in the main chamber. The latter houses a hemispherical analyzer for *high pressure x-ray photoelectron spectroscopy (HP-XPS)* and high pressure (HP) cell with a separate load lock that allows catalytic reactivity measurements at near-ambient pressure conditions (up to 2 mbar). The synchrotron light after the monochromator enters the cell via a Si$_3$N$_4$ membrane window while the electrons escape to the analyzer through a 1mm aperture situated some millimeters in front of the sample. The crystal is heated in the preparation chamber by direct electron bombardment of the sample plate, while in the HP cell the heating is provided through electron bombardment of the high pressure cell wall. The sample temperature is measured both by a type K thermocouple and a pyrometer. The reaction was carried in a flow regime and monitored by QMS. Experimental guidance and operation was performed and assisted by *J. Weissenrieder and M. Soldemo*, members of Material Physics Division, KTH Royal Institute of Technology.

93

The evolution of O-species, present in O_2-treated samples, was monitored *in situ* and *ex situ* by XPS. Already at room temperature a shoulder on the high binding energy (BE) side of the lattice oxygen peak at 529.2 eV was detected. The intensity of the shoulder increased significantly at 450 K as shown in Fig.5.11. This indication of a newly formed O-species, active in the CO oxidation reaction, is fully consistent with the results described above. The 'as prepared' film was of Mn_3O_4 stoichiometry as concluded from XPS O 1s normalization by O(2×2)-Pt(111) and LEED pattern. After O_2 treatment in the HP cell the original LEED pattern was gone, which again certifying the amorphous state of the final O-enriched film. Oxygen content in the oxide film increased roughly 1.3 times after O_2-treatment in the HP cell. The binding energy of the main line in the O 1s spectrum goes from approximately 529.2 eV to 529.4 eV after oxidation.
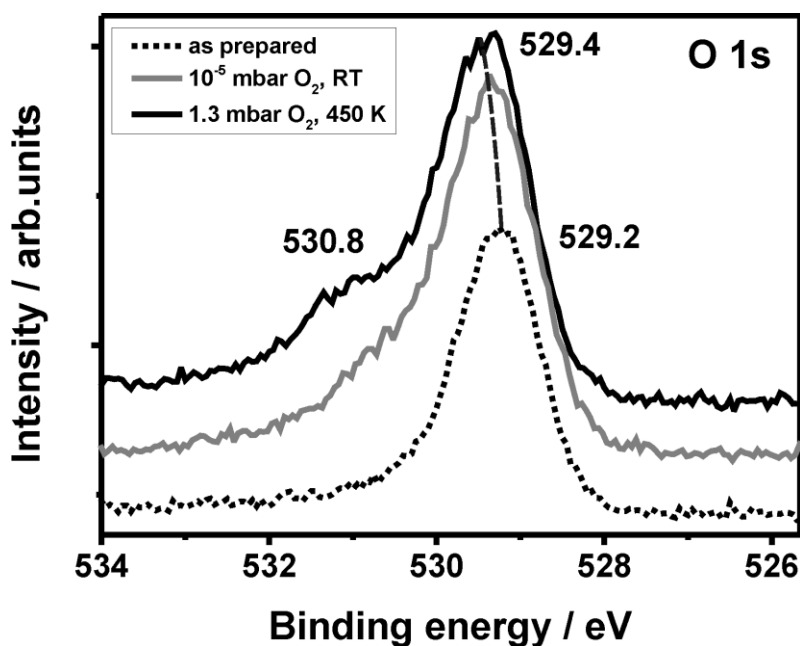
Figure 5.11 XPS spectra for O 1s (h*v*=750 eV) of a monolayer MnO_x film grown on Pt(111): as prepared, after 10^{-5} mbar O_2 in the HP cell at room temperature, after 1.3 mbar O_2 in the HP cell at 450 K. Film was prepared by 1 ML Mn deposition in $5 \cdot 10^{-8}$ mbar O_2 at room temperature followed by postoxidation in 10^{-6} mbar O_2 at 850 K.

The higher binding energy component is shifted approximately 1.4 eV. At the same time (not shown here) the Mn 2p strong line shifts to higher BE after oxidation from around 640.7 eV to 641.1 eV. A low binding energy shoulder at ~ 638.9 eV is almost, all indicative of a higher

oxidation state. The line profile of Mn 2p is rather complicated (as in several 3d elements) with multiplet splitting complicating detailed analysis.

Fig.5.12 shows the kinetics of CO oxidation at different temperatures over 1 ML MnO_x film on Pt(111) upon reaching a steady state regime (at 450 K) at a constant reactants ratio CO/O_2=1:10. After 500 K the film experienced two effects: it undergoes deactivation caused by carbon deposits what could be concluded from CO_2 concentration decrease in the end of each temperature step; the following rapid gain of the reactivity at 530 K could be caused by Pt(111) surface opening - a typical mass transfer limit is comparable from QMS trends [194].
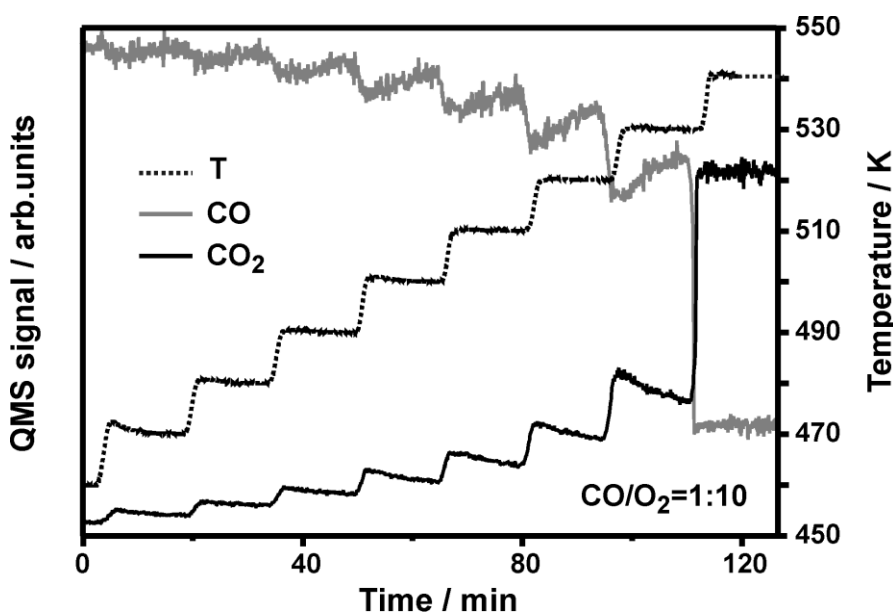
Figure 5.12 CO oxidation kinetics at different temperatures in flow mode over 1 ML MnO_x/Pt(111) upon reaching a steady state regime (450 K), CO/O_2=1:10, p(HP cell) ~1 mbar. Trends are shifted for clarity (~50% CO is converted).

Fig.5.13 displays the reaction kinetics at varying CO partial pressure at 450 K while keeping O_2 partial pressure constant. It can clearly be seen that CO_2 production proportionally follows the change of CO concentration up to CO/O_2 reaching 1:12; this suggests that the reaction is first order for CO. In parallel the amount of CO_2 in the gas phase over the oxide film surface at 450 K and CO/O_2=1:10 was sufficient to be detected by *in situ* HP-XPS (not shown). Such CO pressure dependence can be definitely attributed to the catalytic reaction over the surface of the MnO_x film. It is worth to notice that in the similar experiment with stepwise

increasing CO partial pressure at fixed O_2 pressure over clean Pt(111) no response like CO_2 production following CO concentration change was observed. A 2 ML thick MnO_x film appeared to be less active in CO_2 production. In the flow mode QMS signal 44 for 1 ML MnO_x/Pt(111), 2 ML MnO_x/Pt(111) and Pt(111) had the ratio 1:0.6:0.13 respectively.
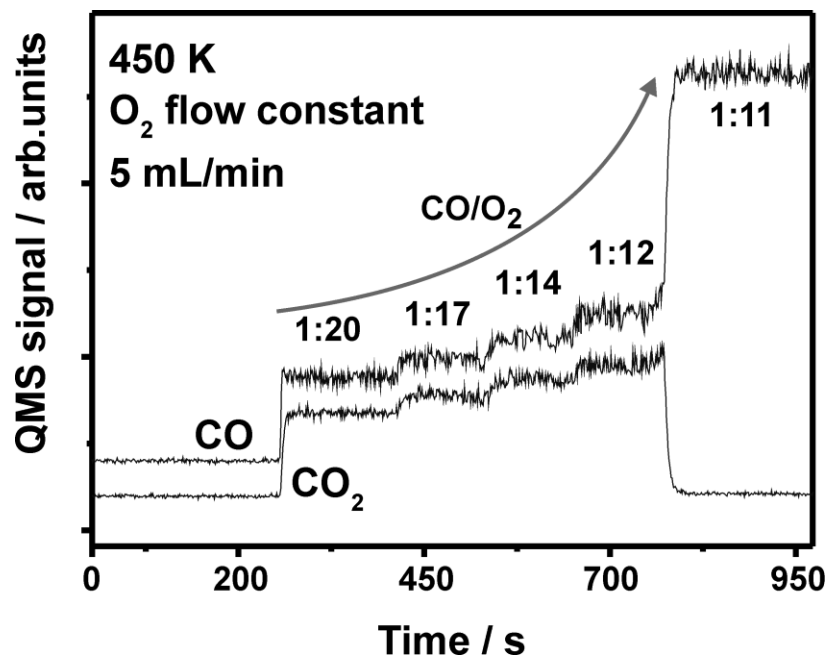
Figure 5.13 CO oxidation kinetics at different CO partial pressures in flow mode over 1 ML MnO_x film on Pt(111) at 450 K and constant O_2 partial pressure (O_2 flowrate through the HP cell is 5 mL/min).

However, when increasing the CO concentration in O_2 above 1:10 the monolayer film cannot convert CO anymore and 'dies'. This happen together with the disappearance of the high BE side shoulder in the O 1s spectrum under CO-rich reaction conditions (the shoulder cannot be restored by pure O_2 treatment and the film remains inactive in a new reaction runs, not shown here). This observation is in agreement with earlier experiments where the ratio of the reactants was found to be crucial requirement for the film stable performance (1:10 against 1:5, Figs. 5.9 and 5.6 respectively). CO adsorption could be detected on the dead surface (*in situ* HP-XPS, C 1s at around 286-287 eV). Therefore, the 'dead' MnO_x surface is considered to be a result of CO poisoning: manganese oxide gets reduced at the high CO partial pressure. Moreover, the spent surface has a different line profile in Mn 2p than the active (a clear doublet in the $2p_{3/2}$). The peaks are located at around 640.8 eV and 641.6 eV respectively (a

split of approximately 0.8 eV), what could certify a different structure or coordination to C. Such a feature is reproducible for a 2 ML MnO$_x$ film as well.

CO can be removed from the 'dead' 1 ML surface by oxygen treatment, but the catalyst will not regain its all native properties. There is some permanent change. In contrast the 2 ML system cannot be made "active" again even though the CO can be removed during regeneration.

5.4 Summary

- Ultrathin MnO$_x$ films epitaxially grown on Pt(111) were studied in the low temperature CO oxidation reaction at near-atmospheric pressures.
- Under O-rich conditions initially crystalline monolayer MnO$_x$ films were transformed into an amorphous MnO$_2$ structure, assigned to O-Mn-O trilayer.
- These films expose more weakly bound O-species as compared to those in MnO(19×1)-Pt(111) films.
- However, for stable catalytic performance MnO$_x$/Pt(111) requires more oxidative reaction conditions (CO/O$_2$=1:10), otherwise the film dewets.

Chapter 6

General trends in CO oxidation over thin oxide films and concluding remarks

6.1 General trends in CO oxidation over thin oxide films

Now, after all the films were introduced in previous sections, it is appropriate to compare on their reactivity in attempts to understand what rational background stays behind the reactivity of ultrathin oxide films on metal supports in low temperature CO oxidation at elevated pressures. For this, we first present thermal desorption spectra of all studied films after oxygen pretreatment on Fig.6.1. $RuO_x/Ru(0001)$, $FeO/Pt(111)$ and $MnO_x/Pt(111)$ placed together in the bottom portion of Fig.6.1 exhibit each well-pronounced evidence of weakly bound oxygen species different from lattice oxygen in pristine films as indicated by dotted lines for clarity: 420, 840 and 950 K correspondingly. $RuO_x/Pt(111)$ demonstrates a number of broadened features around the 'main' oxygen peak what could be interpreted as a mixture of phases other from $RuO_2(110)$. RuO_x thin films prepared on Pt(111) did not show rectangular (110) structure and demonstrated poor performance under reaction conditions in comparison with that of $RuO_2(110)/Ru(0001)$. For comparison a spectrum of 2 MLE thick ZnO/Pt(111) is given: this film is fully inactive under the same conditions.

Quantitatively the difference in catalytic performance can be described in terms of desorption energies of weakly bound oxygen (WBO)-species. Using for the rough approximation the Redhead formula (Eq.2.23), desorption energies were evaluated through the peak temperatures 420, 825, 840, 950 and 1040 K (ZnO has only lattice oxygen) as 109, 219, 223, 253 and 283 kJ·mol^{-1} for $RuO_x/Ru(0001)$, $RuO_x/Pt(111)$, $FeO/Pt(111)$, $MnO_x/Pt(111)$ and ZnO/Pt(111) respectively. Qualitatively the values of WBO desorption energy are in line with activation energies of CO oxidation: 58±4 and 113±5 kJ·mol^{-1} for $RuO_x/Ru(0001)$ [100] and FeO/Pt(111) [14] correspondingly, measured under identical reaction conditions. When the reactivity of the films is plotted against the corresponding desorption energies of WBO-species, the linear

dependence can be observed (see Fig.6.2). Therefore, the lower the desorption temperature of WBO, the more active is the film in the reaction and vice versa. The ratio of WBO to lattice oxygen is not that crucial as well as the origin of the film (deposited or native).
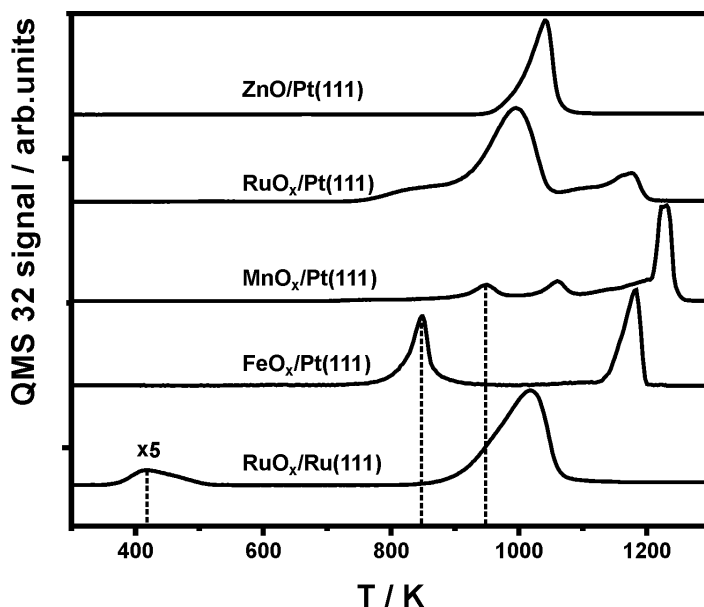

Figure 6.1 TPD spectra of molecular oxygen from decomposition in UHV of the films pretreated with O_2 in the high pressure cell (20 mbar O_2, 450 K, 10 min). Heating rate β=3 Ks^{-1}
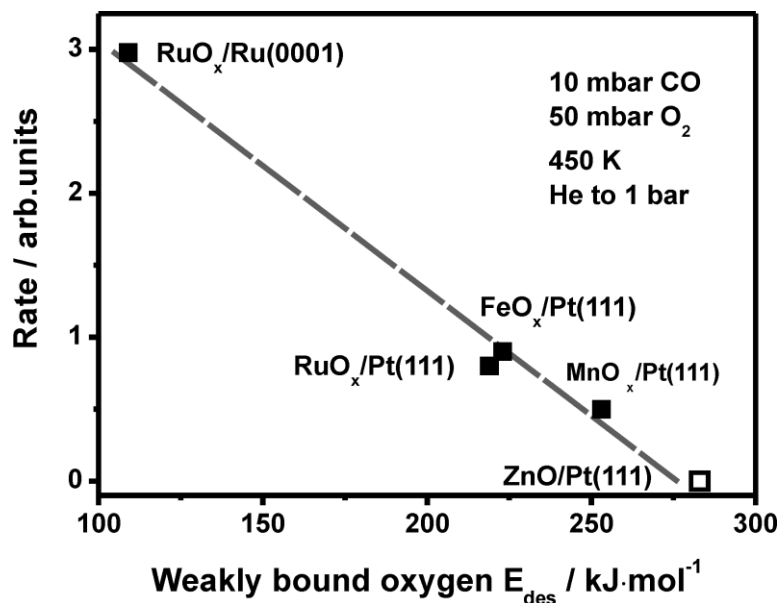

Figure 6.2 The rate of the CO oxidation reaction as a function of desorption energy of weakly bound oxygen for ultrathin films (grown on 2-side polished crystals, besides RuO_x/Pt(111)). The rate is given only for the first 5 minutes of the reaction (zero conversion conditions). Desorption energy is calculated by the Redhead formula. RuO_x and ZnO are 4.5 MLE and 2 ML thick (closed at this coverage), while FeO_x and MnO_x are monolayer films.

The case of ZnO/Pt(111) is different: it is a catalyst with a particular reaction mechanism. The film gets active in low temperature CO oxidation when it partially covers the substrate surface, i.e. in submonolayer regime: as it was shown in Ch.4, the reaction occurs on oxide-metal interface.

It is noteworthy to say that similar attempts to link thermodynamic and kinetic parameters were made regarding such a particular case of oxidative heterogeneous catalysis as the Deacon process (HCl oxidation) over rutile oxide surfaces. In the theoretical work with DFT calculations [195] the authors found volcano dependences of TOFs in oxidation of hydrogen halides as a function of the dissociative chemisorption energy of O_2 and the adsorption energy of OH on a variety of rutile (110) surfaces. Later, experimentally it was shown [196] that the same is correct for bulk oxides.

Therefore, on ultrathin films grown on metals two CO oxidation scenarios (reaction channels) are possible as schematically shown on Fig.6.3. Qualitatively it can be stated that flat closed films act as *oxygen exchangers* due to their capability to activate oxygen from the gas phase and therefore provide weakly bound oxygen (WBO) species under reaction conditions (*surface pathway*, Fig.6.3a). Quantitatively the films reactivity follows the desorption energy of top layer oxygen (Figs. 6.1 and 6.2). Films partially covering the metal substrate surface may accommodate the reactants on the oxide-metal interface and there facilitate their interaction (*interface pathway*, Fig.6.3b).
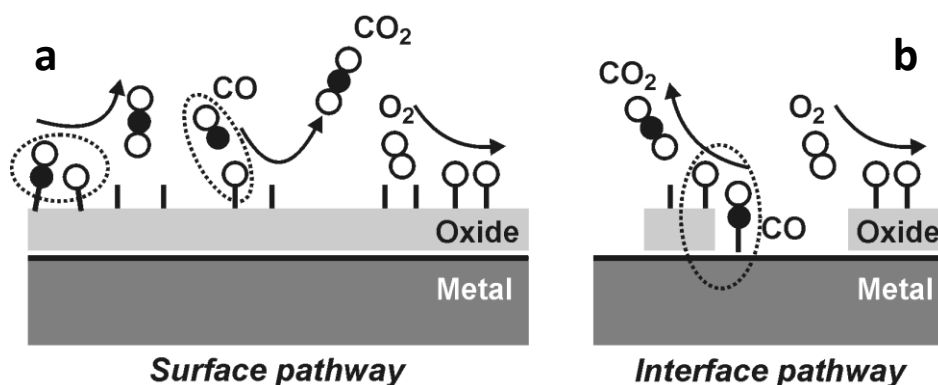
Figure 6.3 Scenarios of the CO oxidation reaction over ultrathin oxide films: a - surface pathway, CO_2 is formed on the film surface; b - interface pathway, the reaction happens on the metal-oxide interface.

6.2 Concluding remarks

Relying on the recent advances in the subject area, the present work comprises a broad experimental basis to formulate basic concepts for low temperature CO oxidation over ultrathin oxide films grown on metals. The performed research has established relationships between the films structure and their reactivity under technologically relevant conditions with a particular focus on thickness influence.

The key findings of the thesis can be summarized as follows.

- A characteristic attribute of the closed films (RuO_x/Ru(0001), MnO_x/Pt(111) and studied earlier FeO/Pt(111) by Y.-N. Sun [14]) as a one of the key observations in this thesis refers to their ability to undergo oxygen enrichment at high chemical potential of oxygen in the CO oxidation reaction under net oxidizing conditions. In that case the catalytic 'power' of a certain film is defined by the strength of chemical bond between the transition metal of the film and weakly bound oxygen species developed under reaction conditions.

- Submonolayer films only partially covering the substrate surface open up another reaction pathway at the oxide/metal boundary, which promotes the reactants activation and interaction. The catalyst activity is defined by availability of the interface border, i.e. its perimeter.

- Oxygen binding energy can serve as a good descriptor for the CO oxidation reaction on oxide films.

- Thickness/coverage dependence allows one to determine the predominant reaction route.

When dealing with a new class of materials scientists highlight its typical properties and categorize into subgroups with similar features. Scientific novelty of the present thesis is addressed as a systematic approach when studying the reactivity of ultrathin oxide films. Previously, the knowledge about thin films as model catalysts was quite segmental and diffuse to give an overall understanding of their catalytic activity. Having accumulated my own results in a separate cycle as a continuation of earlier works of our group, here I in a cooperation with

my colleagues suggest a universal way to 'handle' ultrathin oxide films in catalytic research and to analyze and interpret data.

The practical importance of the performed work could be fully comprehended when transferring its achievements to other more complicated chemical reactions over new kinds of ultrathin oxide films as a good ground in this field. 'Playing' with CO oxidation over mono-component films as a probe reaction should be logically replaced by catalytic processes of higher demand, over multi-component ultrathin oxide films to bridge the 'timeless' gap between industrial research and model studies in heterogeneous catalysis.

My personal contribution includes experimental work with all techniques overviewed in Ch.2 (LEED, AES, TPD and GC) as well as data analysis and interpretation (Chs.3-6). The key results and observations of the thesis were well-documented in several publications and presented to the corresponding scientific community on dedicated conferences as it is shown in App. A.

Bibliography

[1] Ertl, G., Knözinger, H., Schüth, F., & Weitkamp, J. (Ed.). (2008). *Handbook of Heterogeneous Catalysis.* Weinheim: Wiley-VCH Verlag GmbH.

[2] Somorjai, G. A., & Li, Y. (2010). *Introduction to Surface Chemistry and Catalysis.* 2nd ed. Hoboken, NJ: Wiley.

[3] Freund, H.-J., Meijer, G., Scheffler, M., Schlögl, R., & Wolf, M. (2011). CO Oxidation as a Prototypical Reaction for Heterogeneous Processes. *Angewandte Chemie International Edition, 50,* 10064–10094.

[4] Ertl, G., & Freund, H. -J. (1999). Catalysis and surface science. *Physics Today, 52(1),* 32-38.

[5] King, D. A., & Woodruff, D. P. (Ed.). (1982). *The Chemical Physics of Solid Surfaces and Heterogeneous Catalysts.* Volume 4. Amsterdam: Elsevier.

[6] Peden, C. H. F., & Goodman, D.W. (1991). In-situ FT-IRAS study of the CO oxidation reaction over Ru(001) I. Evidence for an Eley-Rideal mechanism at high pressures? *Surface Science, 253,* 44-58.

[7] Freund, H.-J. (2010). Model Studies in Heterogeneous Catalysis. *Chemistry - A European Journal, 16,* 9384–9397.

[8] Freund, H.-J., Kuhlenbeck, H., Libuda, J., Rupprechter, G., Bäumer, M., & Hamann, H. (2001). Bridging the pressure and materials gaps between catalysis and surface science: clean and modified oxide surfaces. *Topics in Catalysis, 15,* 201-209

[9] Stoltze, P., & Nørskov, J. K. (1985). Bridging the "pressure gap" between ultrahigh-vacuum surface physics and high-pressure catalysis. *Physical Review Letters, 55*(22), 2502-2505.

[10] Kuhrs, C., Swoboda, M., & Weiss, W. (2001). Single crystal flow reactor for studying reactivities on metal oxide model catalysts at atmospheric pressure to bridge the pressure gap to the adsorption properties determined under UHV conditions. *Topics in Catalysis, 15*(1), 13-18.

[11] Shaikhutdinov, S., & Freund H.-J. (2012). Ultrathin Oxide Films on Metal Supports: Structure-Reactivity Relations. *Annual Review of Physical Chemistry, 63,* 619-633.

[12] Freund, H. -J. (2007). Metal-supported ultrathin oxide film systems as designable catalysts and catalyst supports. *Surface Science, 601,* 1438–1442.

[13] Freund, H.-J., & Pacchioni G. (2008). Oxide ultra-thin films on metals: new materials for the design of supported metal catalysts. *Chemical Society Reviews, 37,* 2224–2242.

[14] Sun, Y.-N., Qin, Z.-H., Lewandowski, M., Carrasco, E., Sterrer, M., Shaikhutdinov, S., & Freund, H.-J. (2009). Monolayer iron oxide film on platinum promotes low temperature CO oxidation. *Journal of Catalysis, 266,* 359–368.

[15] Sun, Y.-N., Giordano, L., Goniakowski, J., Lewandowski, M., Qin, Z.-H., Noguera, C., Shaikhutdinov, S., ... Freund, H.-J. (2010). The Interplay between Structure and CO Oxidation

Catalysis on Metal-Supported Ultrathin Oxide Films. *Angewandte Chemie International Edition, 49,* 4418 –4421.

[16] Giordano, L., Lewandowski, M., Groot, I. M. N., Sun, Y.-N., Goniakowski, J., Noguera, C., Shaikhutdinov, S., ... Freund, H.-J. (2010). Oxygen-Induced Transformations of an FeO(111) Film on Pt(111): A Combined DFT and STM Study. *Journal of Physical Chemistry C, 114,* 21504– 21509.

[17] Lei, Y., Lewandowski, M., Sun, Y.-N., Fujimori, Y., Martynova, Y., Groot, I. M. N., Meyer, R., ... Freund, H.-J. (2011). CO+NO versus CO+O$_2$ Reaction on Monolayer FeO(111) Films on Pt(111). *ChemCatChem, 3,* 671–674.

[18] Vol'kenshtein, F.F. (1966). Experiment and the electronic theory of catalysis. *Russian Chemical Reviews, 35,* 537-546.

[19] Schwab, G.-M. (1979). Electronics of Supported Catalysts. *Advances in Catalysis, 27,* 1-22.

[20] Slinkin, A.A., & Fedorovskaya, E.A. (1971). Influence of Electronic Interactions with the Carrier and of State of Dispersion of the Metal on the Catalytic Activity of Supported Metal Catalysts. *Russian Chemical Reviews, 40,* 860-871.

[21] Lewandowski, M., Sun, Y.-N., Qin, Z.-H., Shaikhutdinov, S., & Freund H.-J. (2011). Promotional effect of metal encapsulation on reactivity of iron oxide supported Pt catalysts. *Applied Catalysis A: General, 391,* 407–410.

[22] Sun, Y.-N., Qin, Z.-H., Lewandowski, M., Kaya, S., Shaikhutdinov, S., & Freund H.-J. (2008). When an Encapsulating Oxide Layer Promotes Reaction on Noble Metals: Dewetting and In situ Formation of an ''Inverted'' FeO$_x$/Pt Catalyst. *Catalysis Letters, 126,* 31–35.

[23] Woodruff, D.P., & Delchar, T.A. (1994). *Modern techniques of surface science.* Cambridge: University Press.

[24] Clarke L. J., (1985). *Surface crystallography: an introduction to low energy electron diffraction.* Chichester: Wiley.

[25] Seah M. P., & Dench W. A. (1979). Quantitative electron spectroscopy of surfaces: a standard data base for electron inelastic mean free paths in solids. *Surface and Interface Analysis, 1(1),* 2-11.

[26] Oura, K., Lifshits, V. G., Saranin, A. A., Zotov, A.V., & Katayama M. (2003). *Surface science: an introduction.* Berlin: Springer.

[27] Christmann, K. (1991). *Introduction to surface physical chemistry (Topic in physical chemistry).* Darmstadt: Steinkopff-Verlag.

[28] Niemantsverdriet, J.W. (1993). *Spectroscopy in Catalysis: An introduction.* Weinheim: Verlag Chemie.

[29] Alford, T. L., Feldman, L. C., & Mayer, J. W. (2007). *Fundamentals of nanoscale film analysis.* New York: Springer.

[30] Zaremba, E., & Kohn, W. (1976). Van der Waals interaction between an atom and a solid surface. *Physical Review B, 13(6),* 2270-2285.

[31] Habenschaden, E., & Kuppers, J. (1984). Evaluation of flash desorption spectra. *Surface Science, 138,* L147-L150.

[32] King D. A. (1975). Thermal desorption from metal surfaces: A review. *Surface Science, 47,* 384-402.

[33] Redhead P. A. (1962). Thermal desorption of gases. *Vacuum, 12,* 203-211.

[34] Langmuir, I. (1916). The Evaporation, Condensation and Reflection of Molecules and the Mechanism of Adsorption. *Physical Review,* 8, 149-176.

[35] McNair, H., & Miller, J. (2009). *Basic gas chromatography*. 2nd ed. Hoboken, NJ: Wiley-Interscience.

[36] Grob , R. I., & Barry , E. F. (Ed.). (2004). *Modern Practice of Gas Chromatography*, 4th ed. Hoboken, NJ: Wiley.

[37] Settle, F. A. (Ed.). (1997). *Handbook of instrumental techniques for analytical chemistry*. Arlington, VA: Prentice Hall.

[38] Michalk, G., Moritz, W., Pfnür, H., & Menzel, D. A (1983). LEED determination of the structures of Ru(001) and of CO/Ru(001)-$\sqrt{3} \times \sqrt{3}$R30°. *Surface Science, 129,* 92-106.

[39] Madey, T. E., Engelhardt, H. A., & Menzel, D. (1975). Adsorption of oxygen and oxidation of CO on the ruthenium (001) surface. *Surface Science, 48,* 304-328.

[40] Feulner, P., & Menzel, D. (1985). The adsorption of hydrogen on ruthenium (001): adsorption states, dipole moments and kinetics of adsorption and desorption. *Surface Science, 154(2-3),* 465-488.

[41] Kostov, K. L., Rauscher, H., & Menzel, D. (1992). Adsorption of CO on oxygen-covered Ru(001) *Surface Science, 278,* 62-86.

[42] Riedmüller, B., Ciobîc, I.M., Papageorgopoulos, D.C., Frechard, F., Berenbak, B., Kleyn, A.W., Van Santen, R.A. (2001). CO adsorption on hydrogen saturated Ru(0001). *Journal of Chemical Physics, 115,* 5244-5251.

[43] Esch, F., Ladas, S., Kennou, S., Siokou, A., Imbihl, R. (1996). Identification of different surface species of NO adsorbed on Ru(0001) with NEXAFS. *Surface Science, 355,* L253-L258.

[44] Shi, H., Jacobi, K., & Ertl, G. (1993). Dissociative chemisorption of nitrogen on Ru(0001). *Journal of Chemical Physics, 99,* 9248-9254.

[45] Rodriguez, J. A., Kuhn, W. K., C. M. Truong, & Goodman D. W. (1992). A FT-IRAS study of ammonia adsorbed on Ru(0001). *Surface Science, 271,* 333-339.

[46] Hoffmann W., & Benndorf, C. (2000). Water adsorption structures on flat and stepped Ru(0001) surfaces. *Journal of Vacuum Science & Technology A, 18,* 1520-1525.

[47] Larsen, J. H., Holmblad, P. M., & Chorkendorff, I. (1999). Dissociative sticking of CH_4 on Ru(0001). *Journal of Chemical Physics, 110,* 2637-2642.

[48] Ransley, I. A., Ilharco, L.M., Bateman, J.E., Sakakini, B.H., Vickerman, J.C., Chesters, M.A. (1993). Adsorption and thermal decomposition of ethene and propene on Ru(0001), studied by RAIRS. *Surface Science, 298,* 187-194.

[49] Barros, R.B., Garcia, A.R., & Ilharco, L.M. (2001). The decomposition pathways of methanol on clean Ru(0001), studied by reflection-absorption infrared spectroscopy (RAIRS). *Journal of Physical Chemistry B, 105,* 11186-11193.

[50] Lee, H.-I., & White, J.M. (1980). Carbon monoxide oxidation over Ru(001). *Journal of Catalysis, 63,* 261-264.

[51] Shi, H., Jacobi, K., & Ertl, G. (1995). Interaction of hydrogen with nitrogen atoms chemisorbed on a Ru(0001) surface. *Journal of Chemical Physics, 102,* 1432-1439.

[52] Carabineiro, S.A.C., Matveev A.V., Gorodetskii V.V., & Nieuwenhuys B.E. (2004). Selective oxidation of ammonia over Ru(0001). *Surface Science, 555,* 83-93.

[53] Mullins, D.R., Radulovic, P.V., & Overbury S.H. (1999). Ordered cerium oxide thin films grown on Ru(0001) and Ni(111). *Surface Science, 429,* 186–198.

[54] Männig, A., Zhao, Z., Rosenthal, D., Christmann, K., Hoster, H., Rauscher, H., Behm, R.J. (2005). Structure and growth of ultrathin titanium oxide films on Ru(0001). *Surface Science, 576,* 29–44.

[55] Ketteler, G., & Ranke, W. (2003). Heteroepitaxial Growth and Nucleation of Iron Oxide Films on Ru(0001). *Journal of Physical Chemistry B, 107,* 4320-4333.

[56] Wu, Y., Garfunkel, E., & Madey, T. E. (1996). Growth of ultrathin crystalline Al_2O_3 films on Ru(0001) and Re(0001) surfaces. *Journal of Vacuum Science & Technology* A*, 14,* 2554-2563.

[57] Yang, B., Kaden, W.E., Yu, X., Boscoboinik, J.A., Martynova, Y., Lichtenstein, L., Heyde, M., (...), Freund, H.-J. (2012). Thin silica films on Ru(0001): monolayer, bilayer and three-dimensional networks of $[SiO_4]$ tetrahedra. *Physical Chemistry Chemical Physics, 14,* 11344-11351.

[58] Pan, Y., Shi, D.-X., & Gao, H.-J. (2007). Formation of graphene on Ru(0001) surface. *Chinese Physics,* 16, 3151-3153.

[59] Buatier De Mongeot, F., Scherer, M., Gleich, B., Kopatzki, E., Behm, R.J. (1998). CO adsorption and oxidation on bimetallic Pt/Ru(0001) surfaces – a combined STM and TPD/TPR study. *Surface Science,* 411, 249–262.

[60] Wang, J., Fan, C.Y., Jacobi, K., & Ertl, G. (2001). Adsorption and reaction of CO on RuO_2(110) surfaces. *Surface Science,* 481, 113-118.

[61] Kim Y. D., Seitsonen, A.P., Wendt, S., Wang, J., Fan, C., Jacobi, K., Over, H., & Ertl, G. (2001). Characterization of Various Oxygen Species on an Oxide Surface: RuO_2(110). *Journal of Physical Chemistry* B, 105, 3752-3758.

[62] Jacobi, K., Wang, Y., & Ertl, G. (2006). Interaction of hydrogen with RuO_2(110) surfaces: activity differences between various oxygen species. *Journal of Physical Chemistry B, 110,* 6115–6122.

[63] Wang, Y., Jacobi, K., & Ertl, G. (2003). Interaction of NO with the Stoichiometric RuO_2(110) Surface. *Journal of Physical Chemistry B, 107,* 13918-13924.

[64] Lobo, A., & Conrad, H. (2003). Interaction of H_2O with the RuO_2(110) surface studied by HREELS and TDS. *Surface Science, 523,* 279–286.

[65] Paulus, U. A., Wang, Y., Bonzel, H.P., Jacobi, K., & Ertl, G. (2005). Adsorption and Interaction of Ethylene on RuO_2(110) Surfaces. *Journal of Physical Chemistry B*, 109, 2139-2148.

[66] Erlekam, U., Paulus, U.A., Wang, Y., Bonzel, H.P., Jacobi, K., & Ertl, G. (2005). Adsorption of Methane and Ethane on RuO_2(110) Surfaces. *Zeitschrift für Physikalische Chemie, 219,* 891–903.

[67] Wang, J., Fan, C. Y., Jacobi, K., & Ertl, G. (2002). The Kinetics of CO Oxidation on RuO_2(110): Bridging the Pressure Gap. *Journal of Physical Chemistry B*, 106, 3422-3427.

[68] Wang, Y., Jacobi, K., Schöne, W.-D., & Ertl, G. (2005). Catalytic Oxidation of Ammonia on RuO_2(110) Surfaces: Mechanism and Selectivity. *Journal of Physical Chemistry B*, *109,* 7883-7893.

[69] Zweidinger, S. Crihan, D., Knapp, M., Hofmann, J.P., Seitsonen, A.P., Weststrate, C.J., Lundgren, E., (...), Over, H. (2008). Reaction Mechanism of the Oxidation of HCl over RuO_2(110). *Journal of Physical Chemistry* C, 112, 9966–9969.

[70] Over, H. (2012). Surface Chemistry of Ruthenium Dioxide in Heterogeneous Catalysis and Electrocatalysis: From Fundamental to Applied Research. *Chemical Reviews,* 112, 3356–3426.

[71] Peden, C.H.F., & Goodman, D.W. (1986). Kinetics of CO oxidation over Ru(0001). *Journal of Physical Chemistry,* 90, 1360-1365.

[72] Goodman, D.W, & Peden C.H.F, & Chen, M.S. (2007). CO oxidation on ruthenium: The nature of the active catalytic surface. *Surface Science,* 601, L124-L126.

[73] Over, H., Kim, Y.D., Seitsonen, A.P., Wendt, S., Lundgren, E., Schmid, M., Varga, P., (...), Ertl, G. (2000). Atomic-Scale Structure and Catalytic Reactivity of the RuO_2(110). *Surface Science, 287,* 1474-1476.

[74] Kim, Y.D., Over, H., Krabbes, G., & Ertl, G. (2001). Identification of RuO_2 as the active phase in CO oxidation on oxygen-rich ruthenium surfaces. *Topics in Catalysis, 14,* 95-100.

[75] Wendt, S., Knapp, M., & Over, H. (2004). The Role of Weakly Bound On-Top Oxygen in the Catalytic CO Oxidation Reaction over RuO_2(110). *Journal of American Chemical Society, 126,* 1537-1541.

[76] Narkhede, V., Aßmann, J., & Muhler, M. (2005). Structure-Activity Correlations for the Oxidation of CO over Polycrystalline RuO_2 Powder Derived from Steady-State and Transient Kinetic Experiments. *Zeitschrift für Physikalische Chemie*, *219,* 979-995.

[77] Aßmann, J., Löffler, E., Birkner, A., & Muhler, M. (2003). Ruthenium as oxidation catalyst: bridging the pressure and material gaps between ideal and real systems in heterogeneous catalysis by applying DRIFT spectroscopy and the TAP reactor. *Catalysis Today, 85,* 235–249.

[78] Blume, R., Hävecker, M., Zafeiratos, S., Teschner, D., Kleimenov, E., Knop-Gericke, A., Schlögl, R., (...), Kiskinova, M. (2006). Catalytically active states of Ru(0001) catalyst in CO oxidation reaction. *Journal of Catalysis, 239(2),* 354-361.

[79] Rosenthal, D., Girgsdies, F., Timpe, O., Blume, R., Weinberg, G., Teschner, D., & Schlögl, R. (2009). On the CO-oxidation over oxygenated Ruthenium. *Zeitschrift für Physikalische Chemie*, 223, 183-207.

[80] Hendriksen, B.L.M., & Frenken, J.W.M. (2002). CO Oxidation on Pt(110): Scanning Tunneling Microscopy Inside a High-Pressure Flow Reactor. *Physical Review Letters, 89,* 046101-1.

[81] Hendriksen, B.L.M., Bobaru, S.C., & Frenken, J.W.M. (2004). Oscillatory CO oxidation on Pd(100) studied with in situ scanning tunneling microscopy. *Surface Science*, 552, 229-242.

[82] Lundgren, E., Kresse, G., Klein, C., Borg, M., Andersen, J.N., De Santis, M., Gauthier, Y., (...), Varga, P. (2002). Two-Dimensional Oxide on Pd(111). *Physical Review Letters*, 88, 246103.

[83] Ackermann, M.D., Pedersen, T.M., Hendriksen, B.L.M., Robach, O., Bobaru, S.C., Popa, I., Quiros, C., (...), Frenken, J.W.M. (2005). Structure and Reactivity of Surface Oxides on Pt(110) during Catalytic CO Oxidation. *Physical Review Letters*, 95, 255505.

[84] Gustafson, J., Mikkelsen, A., Borg, M., Lundgren, E., Köhler, L., Kresse, G., Schmid, M., (...), Andersen, J.N. (2004). Self-Limited Growth of a Thin Oxide Layer on Rh(111). *Physical Review Letters*, 92, 126102.

[85] Gustafson, J., Westerström, R., Mikkelsen, A., Torrelles, X., Balmes, O., Bovet, N., Andersen, J.N., (...), Lundgren, E. (2008). Sensitivity of catalysis to surface structure: The example of CO oxidation on Rh under realistic conditions. *Physical Review B*, 78, 045423.

[86] Stampfl, C., & Scheffler, M. (1997). Study of CO oxidation over Ru(0001) at high gas pressures. *Surface Science, 377-379,* 808-812.

[87] Reuter, K., Stampfl, C., Ganduglia-Pirovano, M. V., & Scheffler, M. (2002). Atomistic description of oxide formation on metal surfaces: the example of ruthenium. *Chemical Physics Letters, 352,* 311–317.

[88] Reuter, K. (2007). Nanometer and Subnanometer Thin Oxide Films at Surfaces of Late Transition Metals. In U. Heiz, U. Landman (Ed.), *Nanocatalysis* (pp. 343-374). Berlin: Springer.

[89] Reuter, K. (2006). Insight into a Pressure and Materials Gap: CO Oxidation at "Ruthenium" Catalysts. *Oil & Gas Science and Technology, 61,* 471-477.

[90] Joo, S. H., Park, J.Y., Renzas, J.R., Butcher, D.R., Huang, W., & Somorjai, G.A. (2010). Size Effect of Ruthenium Nanoparticles in Catalytic Carbon Monoxide Oxidation. *Nano Letters, 10(7),* 2709-2713.

[91] Gao, F., Wang, Y., Cai, Y., & Goodman, D.W. (2009). CO oxidation over Ru(0001) at near-atmospheric pressures: From chemisorbed oxygen to RuO_2. *Surface Science, 603,* 1126-1134.

[92] Grant, J. T., & Haas, T. W. (1970). A study of Ru(0001) and Rh(111) surfaces using LEED and Auger electron spectroscopy. *Surface Science, 21,* 76-85.

[93] Musket, R. G., McLean, W., Colmenares, C.A., Makowiecki, D.M., & Siekhaus, W.J. (1982). Preparation of atomically clean surfaces of selected elements: a review. *Applied Surface Science, 10,* 143-207.

[94] Kostov, K.L., Gsell, M., Jakob, P., Moritz, T., Widdra, W., & Menzel, D. (1997). Observation of a novel high density 30(2 x 2) structure on Ru(001). *Surface Science Letters, 394,* L138-L144.

[95] Stampfl, C., Schwegmann, S., Over, H., Scheffler, M., & Ertl, G. (1996). Structure and Stability of a High-Coverage (1×1) Oxygen Phase on Ru(0001). *Physical Review Letters, 77,* 3371–3374.

[96] King, D. A., & Woodruff, D. P. (Ed.). (2001). *The Chemical Physics of Solid Surfaces and Heterogeneous Catalysts.* Volume 9. Amsterdam: Elsevier.

[97] Kim, Y.D., Seitsonen, A.P., & Over, H. (2000). The atomic geometry of oxygen-rich Ru(0001) surfaces: coexistence of (1×1)O and RuO_2(110) domains. *Surface Science, 465,* 1-8.

[98] Lin, W. F., Zei, M. S., Kim, Y. D., Over, H., & Ertl, G. (2000). Electrochemical versus Gas-Phase Oxidation of Ru Single-Crystal Surfaces. *Journal of Physical Chemistry B, 104,* 6040-6048.

[99] Wendt, S., Seitsonen, A.P., Kim, Y.D., Knapp, M., Idriss, H., & Over, H. (2002). Complex redox chemistry on the RuO_2(110) surface: experiment and theory. *Surface Science, 505,* 137–152.

[100] Martynova, Y., Yang, B., Yu, X., Boscoboinik, J.A., Shaikhutdinov, S., & Freund, H.-J. (2012). Low Temperature CO Oxidation on Ruthenium Oxide Thin Films at Near-Atmospheric Pressures. *Catalysis Letters, 142,* 657–663.

[101] Rössler, M., Günther, S., & Wintterlin, J. (2007). Scanning Tunneling Microscopy of the RuO_2(110) Surface at Ambient Oxygen Pressure. *Journal of Physical Chemistry C, 111,* 2242-2250.

[102] Herd, B., Knapp, M., & Over, H. (2012). Atomic Scale Insights into the Initial Oxidation of Ru(0001) Using Molecular Oxygen: A Scanning Tunneling Microscopy Study. *Journal of Physical Chemistry C, 116,* 24649–24660.

[103] Over, H., Balmes, O., & Lundgren, E. (2009). In situ structure–activity correlation experiments of the ruthenium catalyzed CO oxidation reaction. *Catalysis Today, 145,* 236-242.

[104] Over, H., Balmes, O., & Lundgren, E. (2009). Direct comparison of the reactivity of the non-oxidic phase of Ru(0001) and the RuO_2 phase in the CO oxidation reaction. *Surface Science, 603,* 298–303.

[105] Aßmann, J., Crihan, D., Knapp, M., Lundgren, E., Löffler, E., Muhler, M., Narkhede, V., (...), Varga, P. (2005). Understanding the Structural Deactivation of Ruthenium Catalysts on an

Atomic Scale under both Oxidizing and Reducing Conditions. *Angewandte Chemie International Edition, 44,* 917-920.

[106] Maeder, T., Muralt, P., & Sagalowicz, L. (1999). Growth of (111)-oriented PZT on RuO_2(100)/Pt(111) electrodes by in-situ sputtering. *Thin Solid Films, 345,* 300-306.

[107] Maillard, F., Lu, G.-Q., Wieckowski, A., & Stimming, U. (2005). Ru-Decorated Pt Surfaces as Model Fuel Cell Electrocatalysts for CO Electrooxidation. *Journal of Physical Chemistry B, 109,* 16230-16243.

[108] Vetrone, J., Foster, C.M., Bai, G.-R., Wang, A., Patel, J., & Wu, X. (1998). Growth, microstructure, and resistivity of RuO_2 thin films grown by metal-organic chemical vapor deposition. *Journal of Material Research, 13(8),* 2281-2290.

[109] Kostov, K.L., Jakob, P., & Menzel, D. (1997). A new high density CO/oxygen coadsorbate layer on Pt(111) and its role in CO oxidation. *Surface Science, 377-379,* 802-807.

[110] Hansen, J. B., & Højlund Nielsen, P. E. (2008). Methanol Synthesis. In G. Ertl, H.Knözinger, F. Schüth, & J. Weitkamp (Ed.). *Handbook of Heterogeneous Catalysis* (pp. 2920–2949). Weinheim: Wiley-VCH Verlag GmbH.

[111] Hinrichsen, K.-O., Kochloefl, K. & Muhler, M. (2008). Water Gas Shift and COS Removal. In G. Ertl, H.Knözinger, F. Schüth, & J. Weitkamp (Ed.). *Handbook of Heterogeneous Catalysis* (pp. 2905–2920). Weinheim: Wiley-VCH Verlag GmbH.

[112] Behrens, M., Studt, F., Kasatkin, I., Kühl, S., Hävecker, M., Abild-Pedersen, F., Zander, S., (...), Schlögl, R. (2012). The Active Site of Methanol Synthesis over $Cu/ZnO/Al_2O_3$ Industrial Catalysts. *Science, 336,* 893-897.

[113] Naumann D'Alnoncourt, R., Xia, X., Strunk, J., Löffler, E., Hinrichsen, O., & Muhler, M. (2006). The influence of strongly reducing conditions on strong metal-support interactions in Cu/ZnO catalysts used for methanol synthesis. *Physical Chemistry Chemical Physics, 8,* 1525-1538.

[114] Campbell, C. T., & Ludviksson, A. (1994). Model for the growth and reactivity of metal films on oxide surfaces: Cu on ZnO(0001)-0. *Journal of Vacuum Science & Technology A, 12(4),* 1825-1831.

[115] Campbell, C. T., & Ernst, K.-H. (1992). Forward and Reverse Water-Gas Shift Reactions on Model Copper Catalysts Kinetics and Elementary Steps Surface Science of Catalysis. In D.J. Dwyer, F.M. Hoffmann (Ed.), *Surface Science of Catalysis, ACS Symposium Series*, *482* (pp. 130–142). Washington, DC: American Chemical Society.

[116] Campbell, C.T., Daube, K.A., & White, J.M. (1987). Cu/ZnO(000-1) and ZnO_x/Cu(111): Model catalysts for methanol synthesis. *Surface Science, 182,* 458–476.

[117] Nakamura, I., Fujitani, T., Uchijima, T., & Nakamura, J. (1998). The synthesis of methanol and the reverse water-gas shift reaction over Zn-deposited Cu(100) and Cu(110) surfaces: comparison with Zn/Cu(111). *Surface Science, 400,* 387–400.

[118] Nakamura, I., Fujitani, T., Uchijima, T., & Nakamura, J. (1996). A model catalyst for methanol synthesis: Zn-deposited and Zn-free Cu surfaces. *Journal of Vacuum Science & Technology* A 14(3), 1464- 1468.

[119] Tusche, C., Meyerheim, H.L., & Kirschner, J. (2007). Observation of Depolarized ZnO(0001) Monolayers: Formation of Unreconstructed Planar Sheets. *Physical Review Letters, 99,* 026102.

[120] Weirum, G., Barcaro, G., Fortunelli, A., Weber, F., Schennach, R., Surnev, S., & Netzer, F.P. (2010). Growth and Surface Structure of Zinc Oxide Layers on a Pd(111) Surface. *Journal of Physical Chemistry* C, *114,* 15432-15439.

[121] Wöll, C. (2007). The chemistry and physics of zinc oxide surfaces. *Progress in Surface Science, 82,* 55–120.

[122] Wilmer, H., Kurtz, M., Klementiev, K.V., Tkachenko, O.P., Grünert, W., Hinrichsen, O., Birkner, A., (...), Muhler, M. (2003). Methanol synthesis over ZnO - a structure-sensitive reaction? *Physical Chemistry Chemical Physics, 5,* 4736–4742.

[123] Kobayashi, M., Golman, B., & Kanno, T. (1995). Diversity of the kinetics of carbon monoxide oxidation on differently prepared zinc oxides. *Journal of the Chemical Society, Faraday Transactions, 91(9),* 1391-1398.

[124] Esser, P., Feierabend, R. & Göpel, W. (1981). Comparative Study on the Reactivity of Polycrystalline and Single Crystal ZnO Surfaces: Catalytic Oxidation of CO. *Berichte der Bunsengesellschaft für physikalische Chemie, 85,* 447–455.

[125] Weiss, E. & Folman, M., (1986). Catalytic reactions on metal-supported semiconductors. Oxidation of CO over ZnO films on silver. *Journal of the Chemical Society, Faraday Transactions 1: Physical Chemistry in Condensed Phases,. 82(7),* 2025-2041.

[126] Chugh, A., Ramachanrdan, S., Tiwari, A. & Narayan, J. (2006). Epitaxial ZnO/Pt Layered Structures and ZnO-Pt Nanodot Composites on Sapphire(0001). *Journal of Electronic Material, 35,* 840-845.

[127] Morkoç, H. & Özgür, Ü. (2009). *Zinc Oxide: Fundamentals, Materials and Device Technology.* Weinheim: Wiley-VCH Verlag GmbH & Co.

[128] Dulub, O., Boatner, L. A., & Diebold, U. (2002). STM study of the geometric and electronic structure of ZnO(0001)-Zn, (000-1)-O, (10-10), and (11-20) surfaces. *Surface Science, 519,* 201–217.

[129] Diebold, U., Koplitz, L. V., & Dulub, O. (2004). Atomic-scale properties of low-index ZnO surfaces. *Applied Surface Science, 237,* 336–342.

[130] Rodriguez, J. A., & Kuhn, M. (1995). Chemical and electronic properties of Pt in bimetallic surfaces: Photoemission and CO-chemisorption studies for Zn/Pt(111). *Journal of Chemical Physics, 102*, 4279-4289.

[131] Duclère, J.-R., Mc Loughlin, C., Fryar, J., O'Haire, R., Guilloux-Viry, M., Meaney, A., Perrin, A., (...), Mosnier, J.-P. (2006). ZnO thin films grown on platinum (111) buffer layers by pulsed laser deposition. *Thin Solid Films, 500,* 78 – 83.

[132] Martynova, Y., Liu, B.-H., McBriarty, M.E., Groot, I.M.N., Bedzyk, M.J., Shaikhutdinov, S., & Freund, H.-J. (2013). CO oxidation over ZnO films on Pt(111) at near atmospheric pressures. *Journal of Catalysis*, *301*, 227-232.

[133] Steininger, H., Lehwald, S., & Ibach, H. (1982). Adsorption of oxygen on Pt(111). *Surface Science, 123,* 1- 17.

[134] Eck, S., Castellarin-Cudia, C., Surnev, S., Ramsey, M.G., & Netzer, F.P. (2002). Growth and thermal properties of ultrathin cerium oxide layers on Rh(111). *Surface Science, 520(3),* 173-185.

[135] Lu, J.-L., Gao, H.-J., Shaikhutdinov, S., & Freund, H.-J. (2006). Morphology and defect structure of the CeO_2(111) films grown on Ru(0001) as studied by scanning tunneling microscopy. *Surface Science, 600(22),* 5004-5010.

[136] Hardacre, C., Ormerod, R.M., & Lambert, R.M. (1994). Platinum-Promoted Catalysis by Ceria: A Study of Carbon Monoxide Oxidation over Pt(111)/CeO_2. *Journal of Physical Chemistry, 98(42),* 10901-10905.

[137] Frost, J.C. (1988). Junction effect interactions in methanol synthesis catalysts. *Nature, 334(6183),* 577-580.

[138] Sun, D., Gu, X.-K., Ouyang, R., Su, H.-Y., Fu, Q., Bao, X., & Li, W.-X. (2012). Theoretical Study of the Role of a Metal–Cation Ensemble at the Oxide–Metal Boundary on CO Oxidation. *Journal of Physical Chemistry C, 116(13),* 7491-7498.

[139] Leisenberger, F.P., Surnev, S., Koller, G., Ramsey, M.G., & Netzer, F.P. (2000). Probing the metal sites of a vanadium oxide–Pd(111) 'inverse catalyst': adsorption of CO. *Surface Science, 444,* 211-220.

[140] Schoiswohl, J., Eck, S., Ramsey, M.G., Andersen, J.N., Surnev, S., & Netzer, F.P. (2005). Vanadium oxide nanostructures on Rh(111): Promotion effect of CO adsorption and oxidation. *Surface Science, 580,* 122-136.

[141] Suchorski, Y., Wrobel, R., Becker, S., & Weiss, H. (2008). CO Oxidation on a CeO_x/Pt(111) Inverse Model Catalyst Surface: Catalytic Promotion and Tuning of Kinetic Phase Diagrams. *Journal of Physical Chemistry C, 112,* 20012-20017.

[142] Axnanda, S., Zhou, W.-P., & White, M.G. (2012). CO oxidation on nanostructured SnO_x/Pt(111) surfaces: unique properties of reduced SnO_x. *Physical Chemistry Chemical Physics, 14,* 10207-10214.

[143] Yang, F., Graciani, J., Evans, J., Liu, P., Hrbek, J., Sanz, J.F., & Rodriguez, J.A. (2011). CO Oxidation on Inverse CeO_x/Cu(111) Catalysts: High Catalytic Activity and Ceria-Promoted Dissociation of O_2. *Journal of American Chemical Society, 133,* 3444-3451.

[144] Lauritsen, J.V., Porsgaard, S., Rasmussen, M.K., Jensen, M.C.R., Bechstein, R., Meinander, K., Clausen, B.S., (...), Besenbacher, F. (2011). Stabilization Principles for Polar Surfaces of ZnO. *ACS Nano, 5(7),* 5987-5994.

[145] Wei, W., Cui, X., Chen, W., & Ivey, D. G. (2011). Manganese oxide-based materials as electrochemical supercapacitor electrodes. *Chemical Society Reviews, 40,* 1697–1721.

[146] Donne, S. W. (2011). Manganese Oxides For Energy Storage And Conversion. New York, NY: Taylor & Francis.

[147] Singhal, S. & Kendall, K. (2003). High Temperature and Solid Oxide Fuel Cells Fundamentals, Design and Applications. Amsterdam: Elsevier Science.

[148] Wang, N., Chu, W., Zhang, T., & Zhao, X.-S. (2011). Manganese promoting effects on the Co–Ce–Zr–O_x nano catalysts for methane dry reforming with carbon dioxide to hydrogen and carbon monoxide. *Chemical Engineering Journal, 170,* 457–463.

[149] Bezrukov, E. V., & Kurina, L. N. (2004). Interaction of Methane and Oxygen with the Surface of Manganese Oxide-Containing Catalysts. *Theoretical and Experimental Chemistry, 40,* 120-124.

[150] Li, S.-B. (2001). Oxidative Coupling of Methane over W-Mn/SiO_2 Catalyst. *Chinese Journal of Chemistry, 19,* 16–21.

[151] Dmuchovsky, B., Freerks, M.C., & Zienty, F.B. (1965). Metal oxide activities in the oxidation of ethylene. *Journal of Catalysis, 4,* 577–580.

[152] Sun, H.-Y., Hua, Q., Guo, F.-F., Wang, Z.-Y. & Huang, W.-X. (2012). Selective Aerobic Oxidation of Alcohols by Using Manganese Oxide Nanoparticles as an Efficient Heterogeneous Catalyst. *Advanced Synthesis and Catalysis, 354,* 569–573.

[153] Yamashita, T., & Vannice, A. (1996). NO Decomposition over Mn_2O_3 and Mn_3O_4. J*ournal of Catalysis, 163,* 158-168.

[154] Delgado Vigil, M. D., Paraguay Delgado, F., Collins Martnez, V., & Lopez Ortiz, A. (2008). Synthesis, characterization and kinetic evaluation of manganese oxide nanoparticles for the H_2O_2 catalytic decomposition. *International Journal of Chemical Reactor Engineering, 6(1),* A5.

[155] Dhandapani, B., & Oyama, S. T. (1997). Gas phase ozone decomposition catalysts. *Applied Catalysis B: Environmental, 11,* 129-166.

[156] Avilova, I. M., & Il'chenko, N. I. (1976). Oxidation of ammonia on a bismuth-manganese oxide catalyst. *Reaction Kinetics and Catalysis Letters, 5,* 55-60.

[157] Crăciun, R., & Dulămiţă, N. (1999). Ethylbenzene Oxidative Dehydrogenation on MnO_x/SiO_2 Catalysts. *Industrial & Engineering Chemistry Research, 38,* 1357-1363.

[158] Wang, C., Sun, L., Cao, Q., Hu, B., Huang, Z., & Tang, X. (2011). Surface structure sensitivity of manganese oxides for low-temperature selective catalytic reduction of NO with NH_3. *Applied Catalysis B: Environmental, 101,* 598–605.

[159] Te, M. & Foley, H. C. (1994). Intrinsic reactivities of manganese oxides for carbon monoxide hydrogenation catalysis. *Applied Catalysis A: General, 119,* 97-106.

[160] Khodakov, Yu. S., Zasypkin, V. V., Galan-Sanches, N. I. & Minachev, Kh. M. (1978). Catalytic activity of chromium, manganese, vanadium, tungsten, and molybdenum oxides in the hydrogenation of ethylene. *Bulletin of Academy of Sciences of USSR, Chemical series, 26,* 1550-1551.

[161] Kim K.-H., & Ihm, S.-K. (2011). Heterogeneous catalytic wet air oxidation of refractory organic pollutants in industrial wastewaters: A review. *Journal of Hazardous Materials, 186,* 16-34.

[162] Genuino, H.C., Dharmarathna, S., Njagi, E.C., Mei, M.C., & Suib, S.L. (2012). Gas-Phase Total Oxidation of Benzene, Toluene, Ethylbenzene, and Xylenes Using Shape-Selective Manganese Oxide and Copper Manganese Oxide Catalysts. *Journal of Physical Chemistry C, 116,* 12066–1207.

[163] Suib, S. L. (2008). Porous Manganese Oxide Octahedral Molecular Sieves and Octahedral Layered Materials. *Accounts of Chemical Research, 41,* 479-487.

[164] Luo, J., Zhang, Q., Garcia-Martinez, J., & Suib, S. L. (2008). Adsorptive and Acidic Properties, Reversible Lattice Oxygen Evolution, and Catalytic Mechanism of Cryptomelane-Type Manganese Oxides as Oxidation Catalysts. *Journal of American Chemical Society, 130,* 3198-3207.

[165] Najafpour, M.M., Rahimi, F., Aro, E.-M., Lee, C.-H., & Allakhverdiev, S.I. (2012). Nano-sized manganese oxides as biomimetic catalysts for water oxidation in artificial photosynthesis: a review. *Journal of Royal Society Interface, 9,* 2383-2395.

[166] Royer, S. & Duprez, D. (2011). Catalytic Oxidation of Carbon Monoxide over Transition Metal Oxides. *ChemCatChem, 3,* 24–6.

[167] Iablokov, V., Frey, K., Geszti, O. & Kruse, N. (2010). High Catalytic Activity in CO Oxidation over MnO$_x$ Nanocrystals. *Catalysis Letters, 134,* 210–216.

[168] Baltanas, M. A., Stiles, A. B. & Katzer, J. R. (1986). Development of supported manganese oxides for partial oxidation: CO oxidation and oxygen availability. *Applied Catalysis, 20,* 15- 29.

[169] Novakova, J. (1971). Isotopic exchange of oxygen 0-18 between the gaseous phase and oxide catalysts. *Catalysis Reviews, 4,* 77-113.

[170] Fishman, A. Y., Kurennykh, T. E., Vykhodets, E. V., & Vykhodets, V. B. (2012). Isotopic exchange of gaseous oxygen with mechanoactivated manganese oxides. *Defect and Diffusion Forum, 326-328,* 713-718.

[171] Müller, F., De Masi, R., Reinicke, D., Steiner, P., Hüfner, S., & Stöwe, K. (2002). Epitaxial growth of MnO/Ag(001) films. *Surface Science, 520(3),* 158-172.

[172] Li, F., Parteder, G., Allegretti, F., Franchini, C., Podloucky, R., Surnev, S., & Netzer, F.P. (2009). Two-dimensional manganese oxide nanolayers on Pd(100): The surface phase diagram. *Journal of Physics Condensed Matter, 21,* 134008.

[173] Hagendorf, Ch., Sachert, S., Bochmann, B., Kostov, K., & Widdra, W. (2008). Growth, atomic structure, and vibrational properties of MnO ultrathin films on Pt(111). *Physical Review B, 77,* 075496.

[174] Nishimura, H., Tashiro, T., Fujitani, T. & Nakamura, J. (2000). Surface structure of MnO/Rh(100) studied by scanning tunneling microscopy and low-energy electron diffraction. *Journal of Vacuum Science & Technology A, 18,* 1460-1463.

[175] Nagel, M., Biswas, I., Peisert, H., & Chassé, T. (2007). Interface properties and electronic structure of ultrathin manganese oxide films on Ag(001). *Surface Science, 601,* 4484-4487.

[176] Chassé, A., Langheinrich, C., Müller, F. & Hüfner, S. (2008). Growth and structure of thin MnO films on Ag(001) in dependence on film thickness. *Surface Science, 602,* 597-606.

[177] Chassé, A., Langheinrich, C., Nagel, M., & Chassé, T. (2011). Photoelectron diffraction studies of Ag(001), MnO(001) and epitaxial MnO films. *Surface Science*, 605, 272-281.

[178] Shantyr, R. (2004). PhD thesis: Scanning tunneling microscopy/scanning tunneling spectroscopy on growth, atomic and electronic structure of Co oxide and Mn oxide films on Ag(001), Halle (Saale): Martin-Luther-Universität Halle-Wittenberg.

[179] Bayer, V. & Podloucky, R. (2007). Formation of $Mn_3O_4(001)$ on MnO(001): Surface and interface structural stability. *Physical Review B,* 76, 165428.

[180] Allegretti, F., Franchini, C., Bayer, V., Leitner, M., Parteder, G., Xu, B., Fleming, A., (...), Netzer, F.P. (2007). Epitaxial stabilization of MnO(111) overlayers on a Pd(100) surface , *Physical Review B,* 75, 224120.

[181] Sachert, S., Polzin, S., Kostov, K. & Widdra, W. (2010). Thickness dependent vibrational and electronic properties of MnO(100) thin films grown on Pt(111). *Physical Review B,* 81, 195424.

[182] Zhang, L., Tang, Z., Wang, S., Ding, D., Chen, M., & Wan, H. (2012). Growth and vibrational properties of MnOx thin films on Rh(111). *Surface Science, 606,* 1507–1511.

[183] Madelung, O., Rössler, U., Schulz, M. (Ed.). (2000). Non-Tetrahedrally Bonded Binary Compounds II, Volume III/17G- Subvolume 41D 'Semiconductors', Group III Condensed Matter. The Landolt-Börnstein Database New York, NY: SpringerMaterials.

[184] Huang, P. M., Li, Y. &. Sumner, M. E (Ed.). (2011). Handbook of Soil Sciences: Properties and Processes. 2nd ed. Boca Raton, FL: CRC Press

[185] McKenzie, R. M. (1972). The Manganese Oxides in Soils - A Review. *Zeitschrift für Pflanzenernährung und Bodenkunde, 131,* 221–242.

[186] Langell, M. A., Hutchings, C. W., Carson, G. A., & Nassir, M. H. (1996). High resolution electron energy loss spectroscopy of MnO(100) and oxidized MnO(100). *Journal of Vacuum Science & Technology A, 14,* 1656-1661.

[187] Okazawa, T. & Kido, Y. (2004). Surface structure and lattice vibrations of MnO(001) analyzed by high-resolution medium energy ion scattering spectroscopy, *Surface Science, 556,* 101–108.

[188] Gorbenko, O.Yu., Graboy, I.E., Amelichev, V.A., Bosak, A.A., Kaul, A.R., Güttler, B., Svetchnikov, V.L., & Zandbergen, H.W. (2002). The structure and properties of Mn_3O_4 thin films grown by MOCVD, *Solid State Communications, 124,* 15–20.

[189] Yamada, N., Ohmasa, M., & Horiuchi, S. (1986). Textures in natural pyrolusite, β-MnO_2, examined by 1 MV HRTEM. *Acta Crystallographica B, 42,* 58-61.

[190] Zheng, D., Sun, S., Fan, W., Yu, H., Fan, C., Cao, G., Yin, Z., & Song, X. (2005). One-Step Preparation of Single-Crystalline β-MnO_2 Nanotubes. *Journal of Physical Chemistry B,* 109, 16439-16443.

[191] Franchini, C., Bayer, V., Podloucky, R., Parteder, G., Surnev, S., & Netzer, F.P. (2006). Density functional study of the polar MnO(111) surface. *Physical Review B, 73,* 155402.

[192] Neubeck, W., Ranno, L., Hunt, M.B., Vettier, C., & Givord, D. (1999). Epitaxial MnO thin films grown by pulsed laser deposition. *Applied Surface Science, 138-139,* 195-198.

[193] Sachert, S. (2008). PhD thesis: Bestimmung der vibratorischen, thermischen und strukturellen Eigenschaften von Manganoxiden auf Pt(111) mittels HREELS, TPD und LEED. Halle (Saale): Martin-Luther-Universität Halle-Wittenberg.

[194] Schnadt, J., Knudsen, J., Andersen, J.N., Siegbahn, H., Pietzsch, A., Hennies, F., Johansson, N., (...), Schaff, O. (2012). The new ambient-pressure X-ray photoelectron spectroscopy instrument at MAX-lab. *Journal of Synchrotron Radiation, 19(5),* 701-704.

[195] Toftelund, A., Man, I. C., Hansen, H. A., Abild-Pedersen, F., Bligaard, T., Rossmeisl, J. & Studt, F. (2012). Volcano Relations for Oxidation of Hydrogen Halides over Rutile Oxide Surfaces. *ChemCatChem, 4,* 1856–1861.

[196] Over, H., Schomäcker, R. (2013). *ACS Catalysis*, submitted.

List of abbreviations

AES Auger electron spectroscopy

AFM atomic force microscopy

DFT density functional theory

GC gas chromatography

GID grazing incidence diffraction

HP (cell) high pressure cell

HREELS high resolution electron energy loss spectroscopy

HRTEM high resolution transmission electron microscopy

HPXPS high pressure x-ray photoelectron spectroscopy

IMFP inelastic mean free path

LEED low energy electron diffraction

LEIS low energy ion scattering

MEIS medium energy ion scattering

ML/MLE monolayer/monolayer equivalent

NEXAFS near edge x-ray absorption fine structure

OCM oxidative coupling of methane

OMS octahedral molecular sieves

PLD pulsed layer deposition

PVD physical vapor deposition

QMB quartz microbalance

RBS Rutherford backscattering

SMSI strong metal-support interaction

SPM scanning probe microscopy

STM scanning tunneling microscopy

TCD thermal conductivity detector

TDS thermal desorption spectroscopy

TEM transmission electron microscopy

TMO transition metal oxide

TOF turnover frequency

TPD temperature-programmed desorption

TPR temperature-programmed reaction

UHV ultrahigh vacuum

VOCs volatile organic compounds

WGSR water gas shift reaction

XAS x-ray absorption spectroscopy

XRD x-ray diffraction

XPS x-ray photoelectron spectroscopy

List of figures and tables

119

121

123

Appendix A: List of publications and conferences attended

PUBLICATIONS

1. Y. Lei, M. Lewandowski, Y.-N. Sun, Y. Fujimori, Y. Martynova, I. M. N. Groot, R. Meyer, L. Giordano, G. Pacchioni, J. Goniakowski, C. Noguera, S. Shaikhutdinov, and H.-J. Freund, *CO + NO vs CO + O$_2$ reaction on monolayer FeO(111) films on Pt(111)*, *ChemCatChem* 3 (2011), p. 671-674.

2. Y. Martynova, B. Yang, X. Yu, J. A. Boscoboinik, S. Shaikhutdinov and H.-J. Freund, *Low Temperature CO Oxidation on Ruthenium Oxide Thin Films at Near-Atmospheric Pressures, Catal.Lett.* 142 (2012), p.657-663

3. B. Yang, W. E. Kaden, X. Yu, J. A. Boscoboinik, Y. Martynova, L. Lichtenstein, M. Heyde, M. Sterrer, R. Włodarczyk, M. Sierka, J. Sauer, S. Shaikhutdinov, H.-J. Freund, *Thin silica films on Ru(0001): Monolayer, bilayer and three-dimensional networks of [SiO$_4$] tetrahedral, Phys. Chem. Chem. Phys.* 14 (2012), p.11344-11351

4. Y. Martynova, B.H. Liu, M.E. McBriarty, I.M.N. Groot, M. Bedzyk, S. Shaikhutdinov, H.-J. Freund, *CO oxidation over ZnO films on Pt(111) at near-atmospheric pressures, J. Catal.* 301 (2013), p. 227-232.

5. Y. Martynova, M. Soldemo, J. Weissenrieder, S. Shaikhutdinov and H.-J. Freund, CO oxidation on Mn-oxide thin films, (2013), *in preparation*

6. Y. Martynova, S. Shaikhutdinov, H.-J. Freund, CO oxidation on metal supported ultrathin oxide films: what makes them active? (2013). *ChemCatChem,* submitted.

CONFERENCE APPEARANCES

1. European Conference on Surface Science (ECOSS-28), 28.8-2.9.2011, Wroclaw, Poland
Y. Martynova, S. Shaikhutdinov, H.-J. Freund
Ru(0001) vs RuO$_x$ thin films in low temperature CO oxidation (oral presentation)

2. European Conference on Surface Science (ECOSS-29), 3.9-7.9.2012, Edinburgh, Scotland, UK

Y. Martynova, B.H. Liu, M.E. McBriarty, I.M.N. Groot, S. Shaikhutdinov, H.-J. Freund

CO oxidation over ultrathin ZnO films on Pt(111) (poster)

3.   46. Jahrestreffen Deutscher Katalytiker, 13-15.3.2013, Weimar, Germany

Y. Martynova, S. Shaikhutdinov, H.-J. Freund

CO oxidation over metal supported ultrathin oxide films (poster)

Appendix B: Curriculum Vitae

Yulia Martynova

geboren am 23.10.1986

in Krasnokamensk, Russland

Schulausbildung

1993 -1998   Schule-Gymnasium № 9, Krasnokamensk, Russland

1998 - 2001   Lyzeum № 7, Tomsk, Russland

2001 - 2003   Lyzeum an der Polytechnischen Universität Tomsk, Russland

Studium

2003-2007   Polytechnische Universität Tomsk, Russland

2007   als Bachelor der Technik und Technologie abgeschlossen

2007-2008   Polytechnische Universität Tomsk

2008   als Diplom-Ingenieur in Chemischen Technologie

des Öls und des Gases abgeschlossen

Berufliche Tätigkeit

07/2008 – 10/2009   Laborantin bei NIOST, Labor der Katalysatoren und

katalytischer Systeme, Tomsk, Russland

Forschungsthema: Preparation and testing of new titanosilicate

catalysts for direct propylene epoxidation with oxygen

Promotion

02/2010   Doktorandin an der Technischen Universität Berlin und

Forschungstätigkeit unter der Leitung von

Herrn Prof. Hans-Joachim Freund am Fritz-Haber-Institut

der Max-Planck-Gesellschaft, Abteilung Chemische Physik,

Berlin, Deutschland

Titel der Dissertation: CO oxidation on metal supported

ultrathin oxide films

Erklärung an Eides statt

Ich versichere an Eides statt, dass ich die vorliegende Arbeit selbständig verfasst und nur die angegebenen Hilfsmittel und Quellen benutzt habe.

Berlin, 28. März 2013